CZECH TECHNICAL UNIVERSITY IN PRAGUE

Faculty of Civil Engineering
Experimental Centre

<u>Dimploma thesis</u>

Experimental assessment of mechanical behaviour of 3D printed modular metamaterials

Matěj Porubský   2023/2024

ČESKÉ VYSOKÉ UČENÍ TECHNICKÉ V PRAZE
Fakulta stavební
Thákurova 7, 166 29 Praha 6

ZADÁNÍ DIPLOMOVÉ PRÁCE

I. OSOBNÍ A STUDIJNÍ ÚDAJE

Příjmení: Porubský   Jméno: Matěj   Osobní číslo: 484564

Zadávající katedra: K210

Studijní program: Stavební inženýrství

Stud. obor/ spec.: Konstrukce pozemních staveb

II. ÚDAJE K DIPLOMOVÉ PRÁCI

Název diplomové práce: Experimentální ověření mechanické odezvy tištěných modulárních metamateriálů

Název diplomové práce anglicky: Experimental assessment of mechanical behaviour of 3D printed modular metamaterials

Pokyny pro vypracování:

Diplomová práce se zabývá návrhem experimentu a experimentálním ověřením vstupních parametrů pro výpočetní materiálový model mechanických modulárních metamateriálů s hexagonálním uspořádáním vnitřní geometrie. Experimentální vzorky jsou v rámci diplomové práce zhotoveny z plastu, a to aditivní metodou 3D tisku. Z důvodu této, velmi specifické, volby výrobní technologie se práce rovněž zabývá vlivem anizotropie lokálních charakteristik vzniklé z důvodu (ne)stejnoměrného ukládání (extruzi) jednotlivých vrstev při tisku.

Seznam doporučené literatury:

Inelastic Analysis of Structures, Milan Jirásek, Zdeněk P. Bažant, 2001

Jméno vedoucího diplomové práce: doc. Ing. Jan Novák, Ph.D.

Datum zadání diplomové práce: 27. 9. 2023   Termín odevzdání DP v IS KOS: 8. 1. 2024
Údaj uveďte v souladu s datem v časovém plánu příslušného ak. roku

_____   _____
Podpis vedoucího práce   Podpis vedoucího katedry

III. PŘEVZETÍ ZADÁNÍ

Beru na vědomí, že jsem povinen vypracovat diplomovou práci samostatně, bez cizí pomoci, s výjimkou poskytnutých konzultací. Seznam použité literatury, jiných pramenů a jmen konzultantů je nutné uvést v diplomové práci a při citování postupovat v souladu s metodickou příručkou ČVUT „Jak psát vysokoškolské závěrečné práce" a metodickým pokynem ČVUT „O dodržování etických principů při přípravě vysokoškolských závěrečných prací".

27. 9. 2023
_____   _____
Datum převzetí zadání   Podpis studenta(ky)

Declaration of Honour

I declare that I have prepared this diploma thesis independently, on my own, under the supervision of Doc. Ing. Jan Novák, Ph.D. and Ing. Michael Somr, Ph.D. I further declare, the thesis was prepared with the help of publicly available resources that are all referenced accordingly.

In Prague ....

Bc. Matěj Porubský

Acknowledgements

Abstract

This thesis is dedicated to the experimental study of the mechanical properties of hexagonal cells and their implementation in modular structures with "meta" characteristics. The experimental observation is based on digital image analysis, which allows detailed measurements and tracking of the behaviour of individual cells as well as their larger scale aggregates. The experimental data obtained is intended to validate a newly developed theoretical mathematical model.

Some experimental executions have been designed as a proof of concept, with an emphasis on developing an efficient method for future, more complex, tests. Optimisation and acceleration of existing procedures were the key objectives, particularly about the theoretical computational model to be fed by quickly and precisely acquired parameters. The processes of modulating the stiffness of the hexagonal cells were carefully studied to optimise and customise their properties for specific engineering applications.

The work also includes measurements to assess the influence of the filling pattern of the 3D printed specimens on their overall performance, which further contributed to a better understanding of the behaviour of these structures. Integrating 3D printing aspects into the experimental framework thus represents yet another dimension of innovation, enabling the efficient development and testing of new material structures with potential for broad engineering applications with additive manufacturing technology at heart.

Key words

Abstrakt

Tato práce se věnuje experimentálnímu studiu mechanických vlastností hexagonálních buněk a jejich agregaci do větších modulárních struktur za účelem dosažení meta-materiálového chování. Experimentální měření je založeno na analýze digitálního obrazu, která poskytuje detailní informaci o mechanickém chování jak jednotlivých buněk tak celých agregátů. Získaná experimentální data mají v budoucnu sloužit k ověření nově vyvinutého teoretického výpočetního modelu.

Některé provedené experimenty byly navrženy jako proof of concept s důrazem na vytvoření efektivní testovací metody pro budoucí ještě detailnější výzkum. Optimalizace a zrychlení stávajících postupů byly klíčovými cíli, zejména s ohledem na teoretický výpočetní model, který vyžaduje rychlý přístup k přesným vstupním parametrům. Procesy modulace tuhosti a orientace vnitřních konzol v hexagonálních buňkách byly pečlivě zkoumány za účelem optimalizace vlastností těchto buněk pro specifické inženýrské aplikace.

Součástí práce byla také měření odhadující vliv vzoru výplně 3D tištěných vzorků na jejich celkovou odezvu, což přispělo k celkovému porozumění chování těchto struktur. Integrace aspektů vzoru 3D tisku do experimentálního rámce představuje další dimenzi inovace, umožňující efektivní vývoj a testování nových materiálových struktur s potenciálem pro inženýrské aplikace využívající aditivní technologie výroby.

Klíčová slova

metamateriály, modulární konstrukce, aditivní výroba, digitální korelace obrazu

Table of content

List of Figures

List of Tables

1   Introduction

In the evolving world of engineering and Materials Science, we face new challenges in the field of structural materials and structures. Metamaterials represent a revolutionary approach to achieve unique mechanical properties that cannot be achieved with traditional materials [1]. It is in the context of this thesis, that we focus on hexagonal cells and their potential to create innovative modular structures with tailored properties.

We believe that understanding the mechanical properties of hexagonal cells and their interaction in modular structures can lead to new ways of designing materials and/or to optimise their performance and use. This work aims not only to study, but more importantly to open the door for innovations in Materials engineering, where the interplay of hexagonal cells in modular structures design will become a useful ingredient.

Incorporating digital image analysis and experimental techniques into our research allows us not only to model the behaviour of hexagonal cells theoretically, but also to validate these models on real experimental data, thus creating efficient workflows for both experimentation and theoretical analysis.

The aim of this work is therefore to contribute to a deeper understanding of hexagonal cell-based structures and to push the boundaries of what is possible in the field of metamaterials a bit forward.

1.1   Metamaterials

1.1.1   Mechanical metamaterials

Metamaterials are structures that are designed to exhibit unique physical properties and behaviour that are not typically found in nature [2–14]. Metamaterials are a continuously evolving field of research and significant developments and discoveries have been made in recent years, see a review paper by Fan et al. [15] for more information. There are multiple types of the metamaterials based on the modified properties, for example electromagnetic [5, 16], thermal [6, 7], optical [8–10], mechanical [11, 12], acoustic [13, 14]. Mechanical metamaterials are typically created with a periodic internal structure that, through its arrangement and geometric behaviour, achieves target (customised) properties [17]. Customised mechanical properties of metamaterials can be achieved based on their topological structure rather than chemical composition which results in behaviour that is different from virgin material from which it is made [18].

1.1.2   Modular cell structures of metamaterials

Metamaterial structures can be divided into individual units forming a modular system. Through the arrangement and the specific types of individual components, it is possible to design the desired characteristics of the overall structure, achieving metamaterial properties by combining the ordinary properties of individual units [11]. Modular structures are versatile and can

be easily assembled and potentially disassembled, offering additional benefits such as reusability. Modular structures are composed of individual prefabricated modules or components. By their arrangement and the type of the individual components can be used to design the desired characteristics of the overall structure. This approach offers advantages such as speed of construction, possible automation, economic efficiency and transformative potential [15, 19]. The construction can be then easily automated using robotic arms or other assembly methods [20].

Another option is discretely assembled mechanical modular metamaterials, which are created by spatially stacking a finite set of predefined parts, forming individual cells and subsequently the entire structure. The assembly of the individual parts allows control of properties such as stiffness, elasticity, chirality, auxeticity, etc. [11, 21]. The desired properties are achieved through the design of the individual parts, which governs the global behaviour through local mechanisms [22]. The discrete assembly approach eliminates scale limitations and allows for reliable, low-cost part production especially with a combination of quickly developing additive manufacturing methods [12, 20]. The integration of mechanical features and specific functions into metamaterials leads to the development of multifunctional structures [23]. One approach is the use of modular multistable metamaterials with reprogrammable mechanical properties, which are assembled by unit cells with tunable snap-through mechanisms [24, 25]. Another approach involves N-fold symmetry motion structures that provide tunable mechanical properties through controllable macroscopic topological reconfiguration [25, 26]. These advancements in modular structures and metamaterials have opened up new possibilities for engineering applications and the design of multifunctional structures.

1.2 Additive manufacturing

1.2.1 Additive manufacturing technology

Additive manufacturing, also known as 3D printing, is a process that involves adding material layer by layer to create a three-dimensional object. This fabrication technique differs from traditional methods, such as moulding, forming, machining, and joining [27–29], and is used in various industries due to its ability to produce complex shapes and geometric features, making it suitable for small to mid series production. Additive manufacturing utilises a range of materials, including metals, polymers, glass, ceramics, and composites [30]. This technology offers precise design control and the ability to create customised parts [31]. Additive manufacturing uses different processes, such as material jetting, powder fusion, directed energy deposition, laser-assisted systems, nozzle-based material extrusion, binder jetting, inkjet printing, sheet lamination or 3D bioprinting [32–35]. Each printing technology has its own advantages and limitations. The choice of technology depends on the specific application and the printable materials used. The most common and widely used technologies of 3D printing [36] are briefly described hereinafter.

1.2.1.1 Stereolithography

Stereolithography (SLA) is a printing method that uses photopolymerization (i.e., resin curing) to create required objects. The printing material is in liquid form and is selectively hardened by

emitting UV light in the form of a single laser beam or overall digital projection (DLP). A similar method is Masked Stereolithography (MSLA) / LCD printing. This technology uses an LCD display to mask the projected UV light into a specific 2D shape for the current layer [35–37].

1.2.1.2   Selective Laser Sintering

Selective Laser Sintering (SLS) technology uses a powder of specific material as printing material. Powder is spread across the whole printing area in the form of individual layers. Powder is dusted everywhere in every layer, therefore this is the only technology that doesn't need supporting structures, because surrounding non-sintered material already serves this purpose. Material is then solidified by fusing the tiny grains of powdered material together by a laser beam. Materials used could be polymers, metals or ceramics [35–37].

1.2.1.3   Fused Filament Fabrication

Fused Filament Fabrication (FFF) is one of the simplest, versatile and widely spread technologies of additive manufacturing. This method can be also found as Fused Deposition Modeling (FDM), which is a patented trademark and these methods are nearly identical. This is extrusion based technology which is usually based on deposing melted filament material. The material is melted in the extrusion head and extruded through the nozzle. Various types of thermoplastic polymers are commonly used as filament materials. Material is applied in layers on top of each other to create 3D objects. This is achieved by the movement of the printing head or the printing bed [35–38].

3D printers can be further categorised based on construction design and the achieved method of movement of the extrusion head of the printer. The categories are [38]:

- *Cartesian Printer*
  The printhead usually moves along the X and Z axes, while the bed moves along the Y axis. These printers work in the Cartesian coordinate system. This type of printer is the simplest and also the most widely used [37].
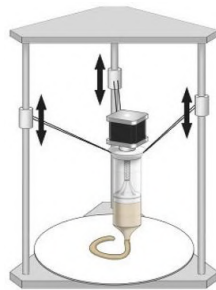
Figure 1: Schematic representation of the Cartesian printer [39]

- *CoreXY Printer*
  The CoreXY printer technology is similar to a Cartesian printer, except that the X and Y axis movements are in some sense linked together [40].

- *Delta printers*

  The head moves in all directions, i.e. X, Y, Z axis, while the bed is stationary. Printing is based on the movement of the head using three arms suspended from a fixed frame above the printing surface. The production is based on the Cartesian coordinate system [37].
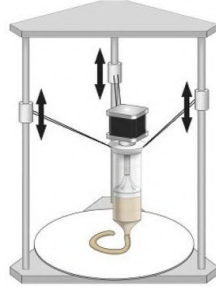
Figure 2: Schematic representation of the Delta printer [39]

- *Polar printers*

  Printing is done by moving the head along a single horizontal and vertical axis and a rotary bed. It operates in a polar coordinate system whose points are determined by distance and angle from a defined central point.It is currently the least common type of the printer [37].
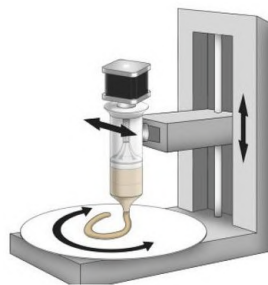
Figure 3: Schematic representation of the Polar printer [39]

- *Scara / Printer with robotic arm*

  The entire printing head is mounted at the end of the robotic arm, which can then move in given directions. The arm of Scara (Selective Compliance Assembly Robotic Arm) 3D printers is usually limited only to planar direction. The vertical direction is controlled separately. However, this type, like the Polar 3D printers, is relatively new and not widely used [41]. Another method is mounting the print head on a multi-axis robotic arm that moves in all directions over a stationary print surface. Production using the robotic arm, unlike conventional three-axis (X, Y, Z) printers, can be many times larger and it is possible to print from almost any angle. No supports are needed during model fabrication, and it is possible to print very complex geometric shapes [42], or to print at large scales from unconventional materials such as specifically designed concrete mixtures[43].

a)   *b)*
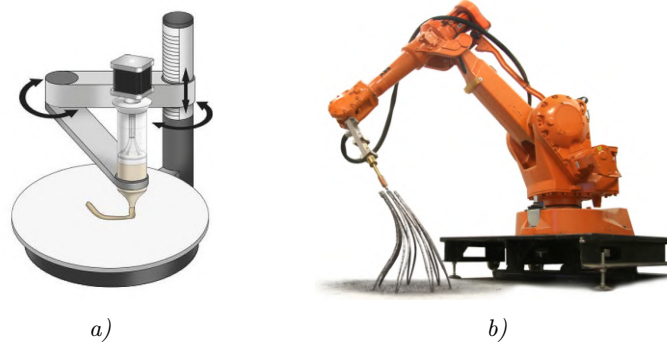
Figure 4: Schematic representation of the Scara printer a) [39], Multi-axis robotic arm with printing head b) [44]

1.2.2   3D Printing procedure

To print an object, a 3D model must be created first. For this purpose, CAD (computer-aided design) [45] modelling program is usually used, and a triangulated model in STL (Standard Tessellation Language or originally STereoLithography) file format is consequently exported. To translate the triangulated model into the language (set of commands) of a 3D printer, a slicer program must be employed. The slicer program is designed for dividing the model in the horizontal direction into individual layers and setting all the parameters for the 3D printing. The slicing program usually works with the models in standardised STL format. There are countless such programs, each with its own advantages and limitations. The output of this program is a G-code file [37, 46]. G-code files containing all the instructions for the 3D printer are written in the form of M-code and G-code commands. G-code is generally a programming language used for controlling CNC machines (which are, unlike additive 3D printers, an example of subtractive manufacturing). G-codes commands are commonly used as functions that specify motion and other specifications [47].

2   Objectives

The research focuses on the construction of cell-based modular metamaterial structures. The modular approach provides economic advantages, speeds up production processes, reusability, and eliminates size constraints [15, 19]. The structure is expected to achieve the meta-properties through the specific arrangement of the cell types and their orientations through the snapping mechanism and modulation of stiffnesses in respective directions.

This thesis proposes methods for obtaining weighted parameters through experimental work to validate continuously evolving mathematical simulations and provide desired input values. The primary objective of the work is to determine the material properties and overall behaviour of the 3D printed samples. The thesis also addresses the issues and characteristics associated with additive manufacturing, which is the chosen fabrication technology for testing samples.

A critical aspect of the experimental measurements involves computer vision and image analy-

sis. A multi-camera measurement system has been developed for the evaluation of metamaterial cells behaviour. This system aims to extend the scope of conventional two-dimensional DIC. The system works with the used loading machine and monitors various parameters through different cameras.

To make the experimental testing procedure and subsequent data processing faster, more robust and automated custom tracking program was developed within this work. The programme was created especially to facilitate the processing of large numbers of performed tests. The primary objective of the program is to provide fast data transfer and dynamically adapt to the requirements of intended mathematical simulations.

This work further focuses on the design and characterisation of metamaterial structures using a modular cell-based approach. The importance of metamaterials in various industries is increasing. A review of relevant literature covers studies on metamaterials, additive manufacturing, and computer vision applications. The terms and scope of this text cover modular structures, additive manufacturing processes, material properties, and state-of-the-art computer vision-based measurement techniques.

The current situation in the field of Materials Engineering emphasises the vast potential of metamaterials and the pressing need to develop efficient manufacturing and rigorous testing methods. While there are advantages to consider, such as economic viability and adaptability, it is important to acknowledge the potential problems associated with the design complexity and the manufacturing process. One recognised gap is the need for an integrated approach to comprehensively characterise metamaterials mechanical behaviour.

The research aims to advance the understanding and practical application of metamaterials through the formulation of rational design methodologies, efficient manufacturing processes, and careful characterization techniques. The core of the research problem is the development of a highly flexible, adaptable and efficient measurement system for the characterization of metamaterial cells and validation of theoretical simulations through rigorous experiments. Additionally, the research focuses on fine-tuning the 3D printing process and improving computer vision-based measurement methods. The experimental process is expected to provide valuable insights for design optimization and practical applications.

The methodology covers various aspects, such as additive manufacturing techniques, computer vision methods, materials testing procedures, and complex data analysis processes. The combination of these elements is designed to effectively achieve the proposed objectives.

he testing will focus on individual cells and their structures/aggregates. The aim is to achieve modularity by ensuring that the structure can be subsequently decomposed. However, several aspects of the 3D printing manufacturing technology are dependent on the parameters set during the manufacturing process. These aspects can potentially alter the properties of the samples. The hypotheses and goals are as follows:

- The type of infill has the same properties regardless of its relative orientation to the axes of the wall samples.

6

- In the case of using multiple independent infills that are not directly interconnected, they will exhibit reduced specimen stiffness due to discontinuities.

- The pre-snapped cell will exhibit higher stiffness.

- The cells will be equivalent in stiffness after snapping to those without the snapping mechanism.

- A macrostructure composed of adhered individual cells will exhibit comparable properties to a structure made as a whole, or what is the effect of bonding.

- Determine whether the bonding is repeatable and therefore whether the macrostructures can be reconfigured. Find out the coefficient of friction for 3D printed samples.

- The developed programme will satisfy all the required aspects.

- The developed multi-camera system will provide useful results..

3   Hexagonal cells as modules

3.1   Description

As mentioned above, the tests were performed to experimentally verify the mathematical simulation. The requirements were to experimentally verify the individual cells and the subsequently created macrostructure, which consisted of individual modules (cells). For this reason, two types of cell sizes were produced. The large samples were used to determine the properties of the individual cells, and (due to a limited size of the print bed) the macrostructure consisted of smaller individual cells. However, small cells were not tested individually. These modules will be combined to form a coherent structure that can be easily decomposed and recombined.

To create a macrostructure from modular cells of the same shape, it was necessary to select a shape with tessellation properties. Tessellation generally refers to the capacity of covering a plane or space by regularly arranged shapes to create a uniform structure without gaps or overlaps. By regular repetition of the identical shape, it becomes possible to form a continuous and infinite pattern, leading to an efficient discretization/tiling of the plane/space. This geometric characteristic has a wide spectrum of applications in various fields, from architecture and art to naturally looking patterns in computer graphics. Tessellation can be achieved by various shapes, such as squares or triangles. However, regular tessellation cannot be created with convex polygons that have seven or more sides . Therefore, a hexagon, which is the polygon with the highest number of sides that can achieve tessellation, is perfectly suited for our purposes. Hexagonal tessellation can be found in nature, for example, in the arrangement of honeycombs or in the crystal structure of several minerals. Filling the plane with hexagons is one of the basic forms of tessellation and can also be found under the term Hexagonal tiling [48].

a) Type A   *b) Type B*   *c) Type C*   *d) Type D*   *e) Type E*
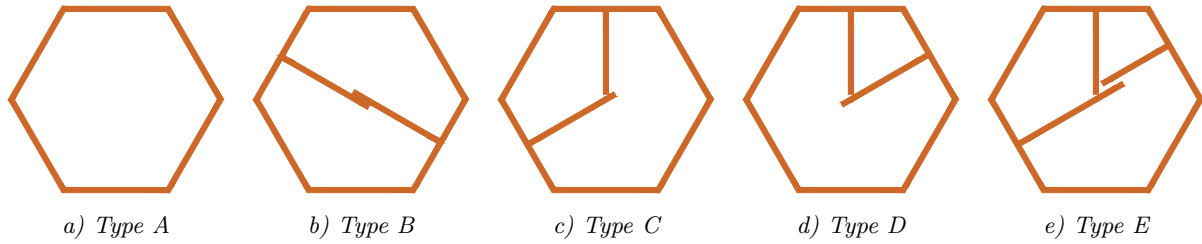
Figure 5: Designed hexagonal cells

The stiffness and overall behaviour of individual cells can be modified through adjustments of dimensions and orientation of the internal cantilevers, resulting in the clock-like appearance of the cells. The combinations of the number of cantilevers, their dimensions and orientations are countless. This design results in a multistable form of these cells through the snapping mechanism. This thesis focuses on two specific cell types – the empty cell (A) and the cell with internal cantilevers (B). Other cells with different inner cantilever orientations are not tested in this paper.

The B type cell features three stages, altering its mechanical properties in response to applied load and consequent deformation. These stages are characterised by several stiffness levels of the cell and different deformation properties, which vary depending on the relative position of the cantilevers.The first stage is defined by a general increase in stiffness as the cantilevers slide against each other. In the second stage, the cantilevers pass over each other, lose contact and the cell behaves similarly to cell type A (without the cantilevers). This stage is characterised by an abrupt reduction in stiffness and highlights the dynamic response of the cell to changes in its internal structure. The third and final stage exhibits a unique behaviour where, under significant deformation, the cantilevers come into contact with the cell walls and wedge themselves into the corners of the cell. This results in an extraordinary increase in stiffness as the cantilevers experience bracing forces combined with bending moment. Due to safety reasons and limitations of the testing equipment, the third stage was not experimentally tested and investigated.

Cell type B also has an additional arrangement where the internal cantilevers are snapped in the default configuration. This means that they are prestressed due to the imposed initial deformation. Type B sample has six different configurations and another six in mirror position. If we also consider configurations with initial prestressing, we get 24 different configurations.

The internal cantilevers can be modulated to achieve desired mechanical properties in cellular structures. The ability to transition between its stages provides a versatile approach to developing adaptive materials with tunable stiffness, making them suitable for various applications in mechanical engineering and beyond. The aim is then to arrange and combine these cells in a way that the overall structure exhibits the desired properties. To achieve modularity and potential reusability, these cells were manufactured individually and then adhered together. The structure as a whole was also created and tested for comparison purposes.
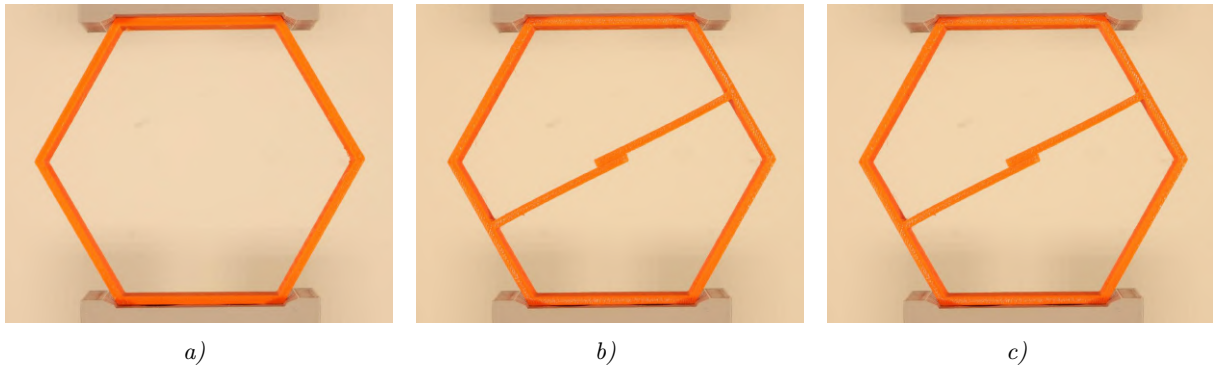
Figure 6: Hexagonal cells: Type A a), Type B initial stage b), Type B prestressed initial stage with snapped cantilevers c)
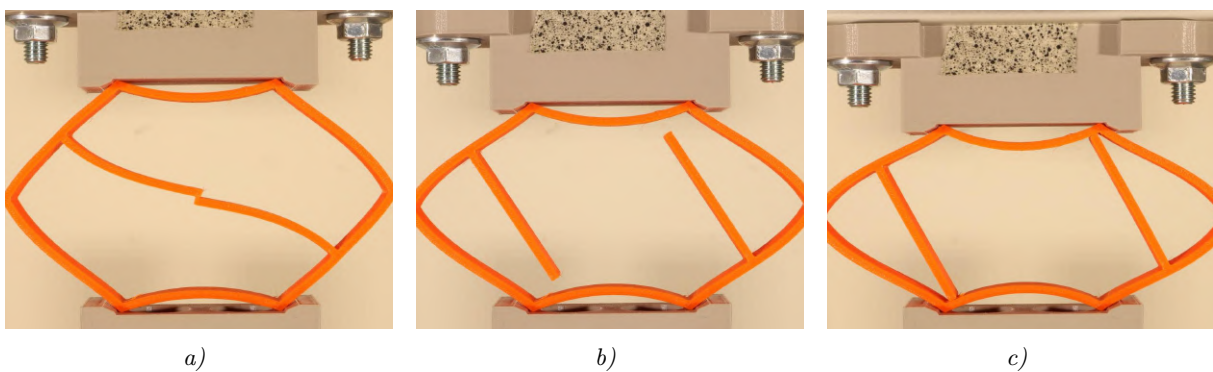
Figure 7: Hexagonal cells type B initial state: First stage before snapp a), Second stage after snapp b), Third stage of contact of the cantilevers with the perimeter walls c)

3.2 Dimensions

As previously stated, two sizes of hexagonal cells were manufactured. The large hexagon has a side centerline length of 50 mm and the small hexagon has a side centerline length of 20 mm. The size of the small cells was determined by the resolution of the 3D printing fabrication method described in the following section. Additionally, a gap was added between the internal cantilevers according to the sample size, as illustrated in Figures of cell dimensions. This is to prevent the overlapping parts from fusing together due to technological manufacturing reasons. All dimensions of the hexagonal cells A and B (Fig) are bases from these proportions:

- Side centerline length = X
- Wall thickness = X · 0.05
- Wall height = X · 0.3
- Cantilevers overlaps X · 0.2
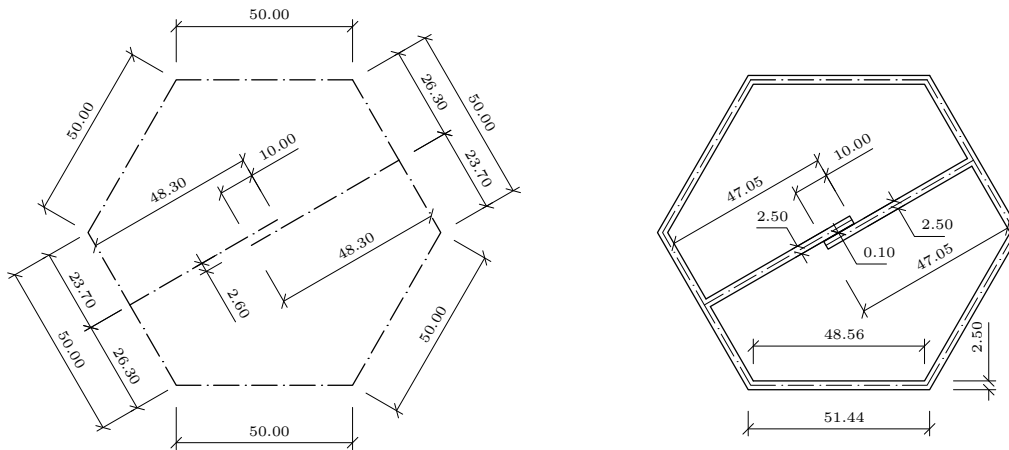
Figure 8: Large hexagon cells dimensions
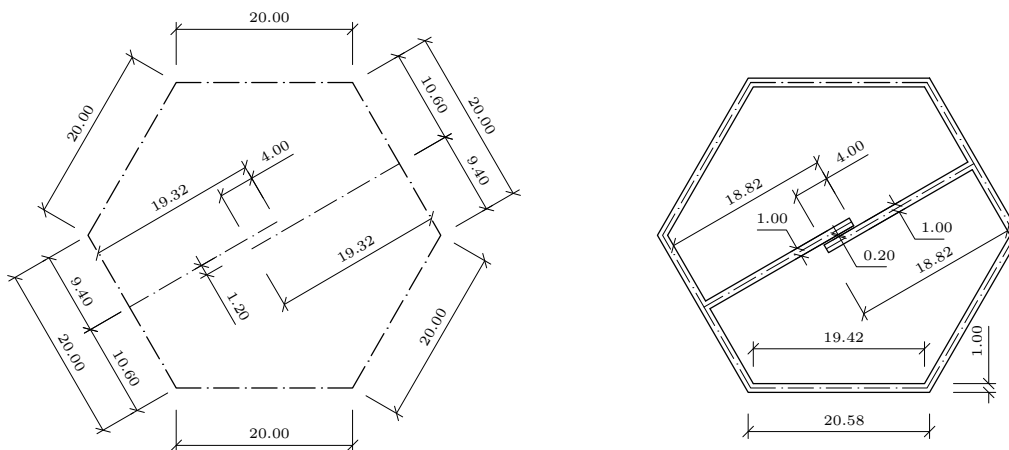
Figure 9: Small hexagon cells dimensions

3.3 Used printer and printing parameters

In this work, samples were manufactured using a Prusa i3 MK3 3D printer. The printer was employed to fabricate the designed cellular structure, other samples and supporting components. Material of the experimental specimens was set to orange *Prusament* PETG (Polyethylene Terephthalate Glycol Copolymer) by Prusa Polymers a.s. [49]. This material was preferred for its mechanical properties, durability, low cost and suitability for prototyping. PETG was also extensively used in producing parts of the experimental set-up components.

The objective was to create small samples as compact as possible. This is because all sample dimensions were scaled proportionally and the goal was to print both individual cells and the entire structure in one go or as a single piece, respectively. Therefore, it was necessary to scale the cells so that the resulting overall structure fit the limited printable area of the printer. To satisfy the demanding design requirements and further increase the versatility of the 3D printing process, modifications were made to the Prusa printer. This included swapping the

conventional print head with an E3D Revo Hemera XS [50] extruder. The significance of this adaptation is the ability to use E3D Revo nozzles [51] with various (finer) diameters, specifically 0.25 mm nozzle diameter. However, finer nozzles required modifying the default printer settings, namely the extrusion rate.The toothed pins responsible for advancing the filament into the nozzle would occasionally skip, resulting in a clicking noise. This problem was caused by over-extrusion, primarily due to the small diameter of the nozzle. The issue was tackled by reducing the material extrusion rate and therefore reducing the overall printing speed. The new extruder was necessary to satisfy the need for reduced wall thickness in the cellular structures, as each wall had to consist of a minimum of two adjacent layers to ensure sufficient strength during manipulation and stability of the printed sample during the manufacturing process. Calibration and testing of the modified 3D printer was essential to ensure the accuracy and precision required for the intricate details of the cellular structures. This modification not just extended the printer's capabilities (the extruder is also suitable for printing flexible and other non-standard filament materials), but also enabled more precise control over the manufacturing process, ultimately leading to successful creation of the small experimental samples.

In conclusion, the Prusa 3D printer, in combination with PETG material and a strategically replaced print head, proved to be a vital tool for producing cellular structures for this thesis. The adaptations enabled a more efficient approach to sample production, highlighting the importance of customising 3D printing technologies to meet specific needs given by the thesis' goals. The final setting of printing parameters is summarised in Tab 1.

Figure 10: E3D Revo Hemera XS print head [50]

Printing parameters:

Printer	Prusa MK3	Prusa MK3 + E3D Hemera head
Printer firmware version	3.10.1	
Slicer - version	Prusa Slicer - 2.5.2	
Material	Prusament Orange PETG	
Nozzle diameter (extrusion width) [mm]	0.4	0.25
Layer height [mm]	0.2	0.1
Extrusion flow [%]	100	90
Printing speed: outer / inner perimeter / infill [mm/s]	25 / 45 / 80	17 / 25.5 / 38.25
Temperature: nozzle / bed (first ; other layers) [°C]	240 / 85 ; 250 / 90	230 / 85 ; 240 / 90
Number of perimeters	1	4
Infill pattern / infill density [%]	Rectilinear / 100	None
Seam position	Aligned	Random
Infill overlap (of extrusion width) [%]	10	20

Table 1: Summary of set printing parameters

3.4   Sample preparation and description

3.4.1   Hexagonal cells

Samples needed to cool down to room temperature before removing them from the printing plate after finishing printing owing to the fact that PETG is a thermoplastic material that can be permanently deformed during manipulation at higher temperatures. The suitability of the samples from the viewpoint of geometry distortion was then evaluated and undeformed ones selected for testing. The specimens were then carefully cleaned to remove string residues known as stringing or oozing [52]. Finally, the samples were lightly sprayed with white colour to enhance contrast for DIC supported measurements linked to speckle patterns created in black.

a)   *b)*
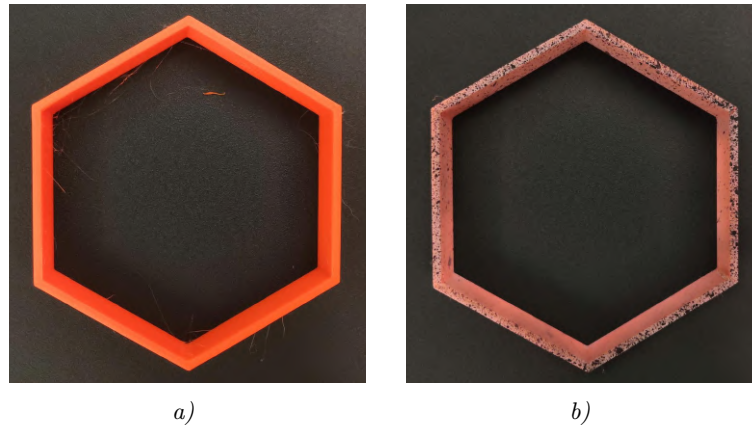
Figure 11: Printed hexagon cell sample a), prepared hexagon cell sample for testing b)

The macrostructure was created in two variations. The first was that individual cells were produced separately and then assembled together. The thickness of neighbouring cells' walls is reduced by half, meaning that when the cells are joined together, they retain their original uniform wall thickness. The second variant was a monolithic single print of identical cell layout to compare the properties of the structure.

a)   *b)*
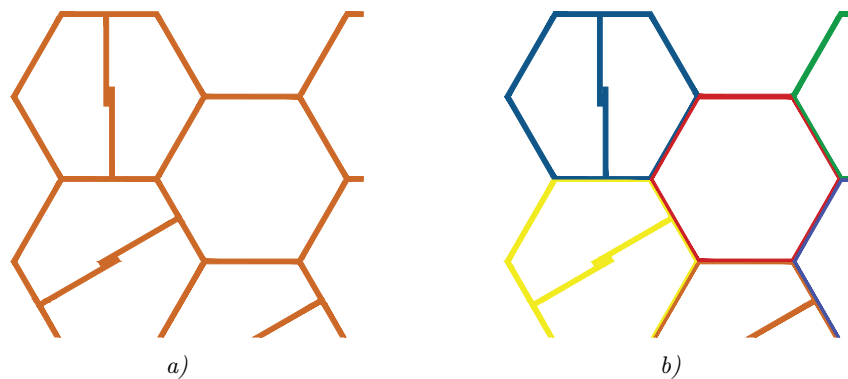
Figure 12: Render of 3D modelled hexagon cells of macrostructure: whole structure a), individual cells b)

a)   *b)*   *c)*   *d)*
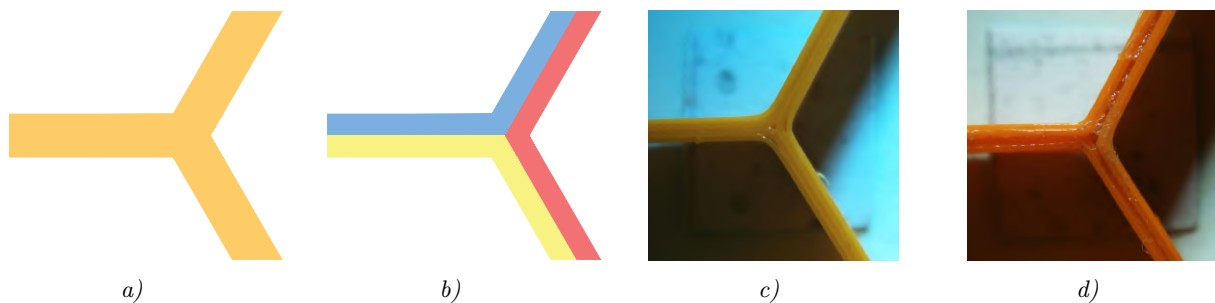
Figure 13: Render of 3D modelled joints of monolithic a) and individual cells b); manufactured joints of monolithic c) and assembled d) macrostructure.

Printing with a nozzle diameter of 0.15 mm was also considered, but because of problems in the case of an attempt to print the macro structure as a whole, which with its dimensions occupies

almost the entire printing area, this nozzle diameter was abandoned. The problem was mainly in the attachment of the first layer at the edges to the printing bed. For this reason, printing was carried out with a 0.25 mm nozzle. The cell dimensions are based on the minimum thickness of the individual cell walls. The walls of the samples had to be made of at least two layers side by side. This is due to the 3D printing technology, the chosen nozzle diameter of 0.25 mm, and to ensure the quality and stability of the sample.

Samples produced using a modified printer were fitted with a 5 mm width brim (a printed border that extends from the edges of the printed part giving it a greater surface area to adhere to the print bed) with 0.01 mm offset from the sample. This offset provided sufficient contact with the sample walls but also allowed for easy removal. The brim was necessary to stabilise the printed sample on the printing bed due to the thin walls and small contact area of the sample. Moreover, it reduced a wall warping that occurred during printing due to temperature effects.

a)   b)

Figure 14: Deformation of vertical wall of the 3D printed sample by 0.25 mm nozzle a), Individual small hexagon cells with added supporting brim highlighted by green color b)

To assemble the individually printed cells into the macrostructure, various types of adhesives were used, including double-sided tape. Finally, the cells were joined together using *Patex Chemopren Univerzal* adhesive, which is used to make flexible joints. This adhesive is highly flexible and elastic [53]. Adhesive can be easily removed by petrol. *Severochema Technical petrol* [54] chemically removes any remaining adhesive, and does not affect mechanical properties of PETG [55], which was proved by fully submerging one cell in petrol for 7 days. The glued small hexagonal cells were held in place by binder clips for 24 hours, and the glue was cured for 48 hours. Labels with a stochastic speckle pattern for the DIC tracking of corners were attached by a small drop of thick cyanoacrylate instant adhesive.

Figure 15: Individual hexagonal cell submerged in technical petrol
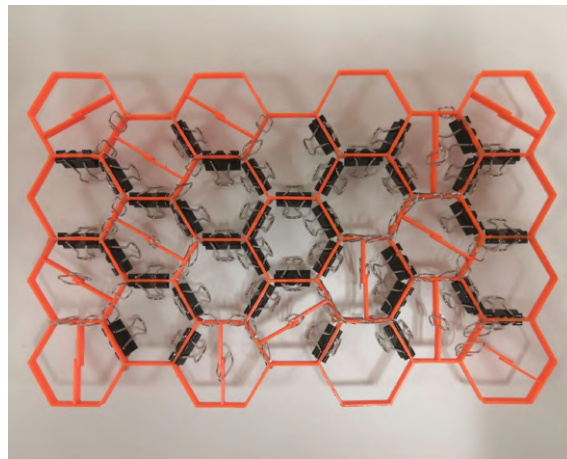
Figure 16: Adhered macrostructure held by binder clips
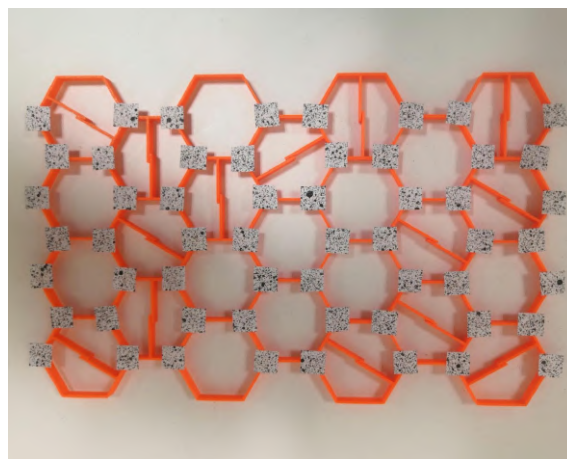
Figure 17: Prepared macrostructure for DIC testing with attached tracking labels

3.4.2   Individual cell walls

During the manufacturing process of the individual wall specimens, randomly occurring surface deformation in the form of waves was observed. These wall specimens were produced for the purpose of subsequent friction coefficient measurements. The searched coefficient is related to the contact surface area between the overlapping parts of the internal cantilevers of the hexagonal B cells. Surface deformations and certain inaccuracies are visible with the naked eye. These

deformations could be caused by printer inaccuracies as well as by environmental influences such as vibration, thermal expansion, cooling, etc. For this reason, wall surfaces printed in three configurations were measured in order to determine which surface corresponds to the first hexagon's cantilever configuration S1, which is the same as the hexagon cantilever printing. The second configuration S2 was attributed to walls with a corresponding gap of 0.1 mm along the entire length, and the third configuration S3 is a standalone wall. This was done in order to find out which manufacturing method corresponds to the first original configuration, from which the coefficient of friction between the surfaces of the hexagon cantilevers will be determined.
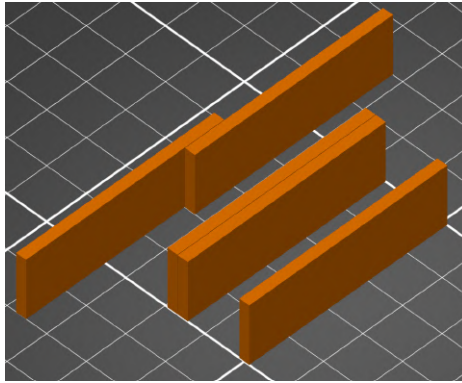
*Figure 18: Types of configuration of printed samples: **A** (top left), **B** (middle), **C** (bottom right)*

With the correct viewing angle, exposure and sharp lighting conditions, it can be seen how the surface differs among the samples, see Figure XY. The single wall of sample S3 is further divided into its two opposite surfaces S3-1 and S3-2. The cause of the surface difference for type S3 is not entirely clear. It may likely be due to the different surrounding air temperature of the regions of respective surfaces. As a perimeter layer was set up, it is possible that it could not resist the effects of temperature changes. Another hypothetical reason could be the vibration resonance of the sample or entire printer/printing bed caused by the movement of the printer stepper motors. These deformations could theoretically be prevented by placing the 3D printer in a thermoregulating chamber. Another theory is that this is caused by the inner infill being printed first and the outer perimeter layer being printed afterwards. When the material is extruded, the resulting layer may be slightly wider than its theoretical width. When the secondary layer is produced, the extra material takes over an extra space and spreads out to the other side from the first layer into the open space. This occurs where the diagonal layer meets the outer perimeter [56].

a) A   *b) B*

c) C1   *d) C2*
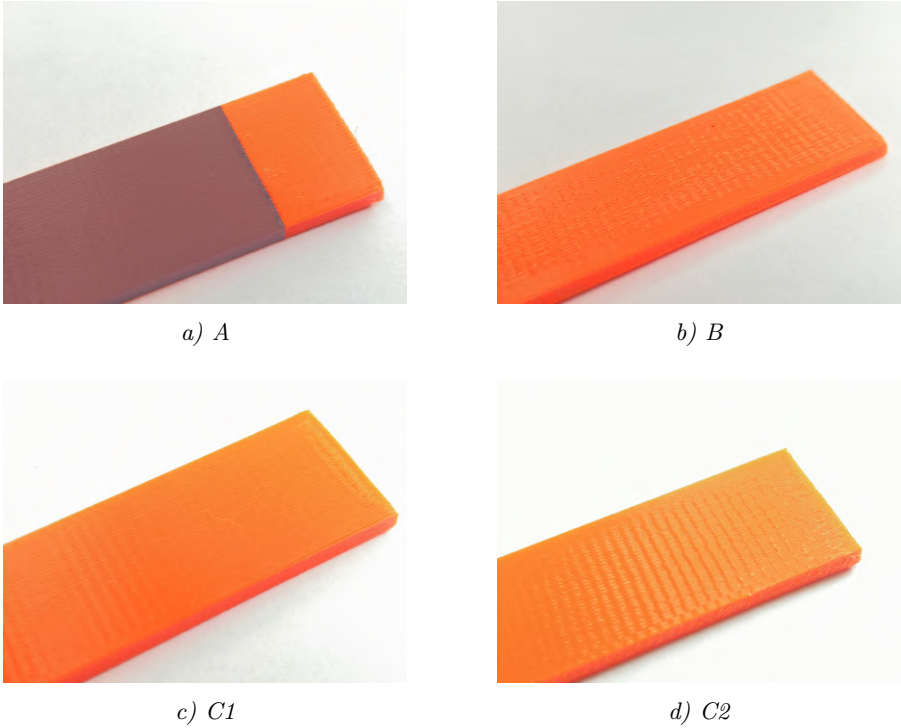
Figure 19: Types of surfaces of wall samples

Figure 20: Stand-alone internal infill pattern
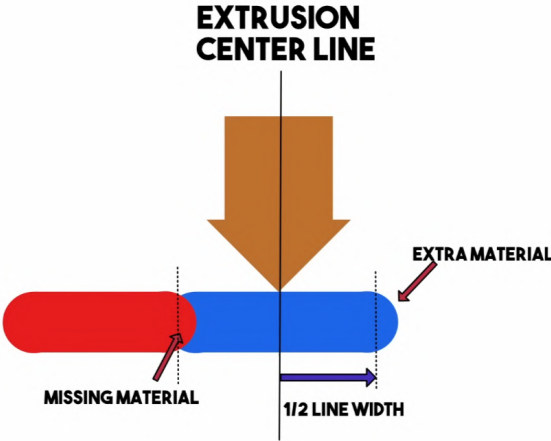
Figure 21: Inaccuracies of extruded material [56]

Despite the fact that the gap between the walls related to type S1 and S2 were identical, the walls of type S2 stuck together. Since the S2 walls are close together along their entire length,

17

there is a greater probability of their spurious bonding to each other. Their separation had to be done by forceful tearing. Similar connections can be observed on sample A, which are highlighted in the figure below. This could be caused by general inaccuracies of the printer and by stringing of the material that happens during the printing head changes its configuration.

a)   b)
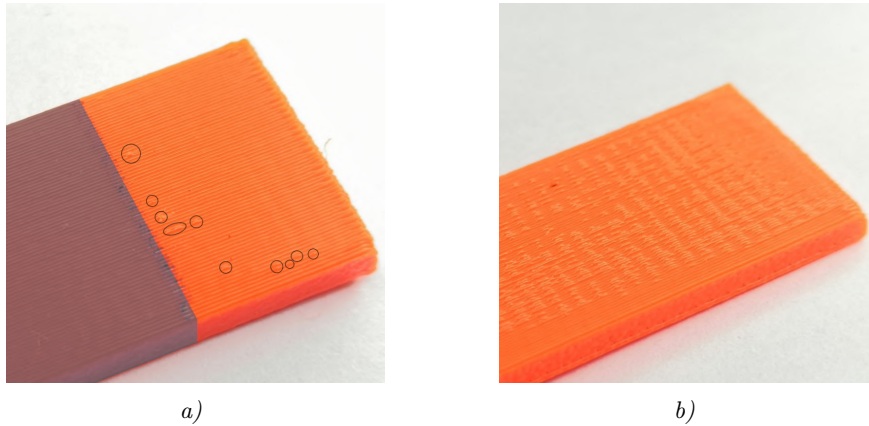
Figure 22: Appearance of out of plane protrusions between samples on surface A a) and B b)

Figure 23: Stringing on printed sample

The observed surface ripple/wrinkling was difficult to replicate due to changing conditions throughout the year. It is likely caused by the infill moving outside the sample perimeter, although the position of the sample on the printing plate may also play a role. Notably, this phenomenon has not been observed at the contact area between the hexagonal sample cantilevers. This ripple effect has been partially reduced by calibrating the 3D printer. However, these ripples only appeared on thin samples. This can be seen in Fig RE, where the sample has a variable thickness. The ripples on these samples appeared only on the thin part, which corresponds to the thickness of the wall samples. This could mean that this effect is influenced by rapid changes in the position of the printing head. The ripple effect observed in the printed samples can be eliminated by changing the pattern of the infill to a parallel pattern. These samples are identified as S4. Another way to eliminate this effect is by reducing the infill overlap values in Slicer, as shown in Tab X. To completely eliminate this effect in combination with the rectilinear infill pattern, the overlap had to be set to -10%. However, reducing the overlap leads to potential

gaps in the sample and weakening the bonds among individual layers. Conversely, increasing this parameter artificially causes the ripple effect. The order of the ticking layers and the width of the extruded material may be the main reasons for this effect to happen, along with printing inaccuracies that can accumulate at certain points. During the initial tests of using the parallel pattern, delamination of the inner layers was observed. For this reason, this pattern was not used.

<div align="center">a)   b)</div>
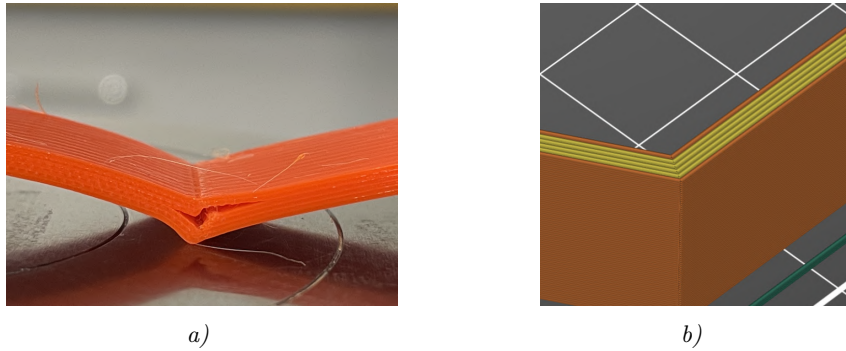
Figure 24: Parallel infill and delamination of layers
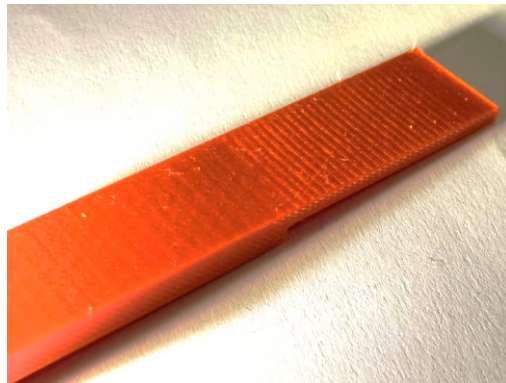
Figure 25: Ripple effect on CP sample with variable thickness

The coefficient of friction of the samples can be significantly affected by the ripple effect, including the number and size of protrusions. If we consider that the contact area of two parallel perfectly smooth surfaces is 100%, then this surface with significant protrusions may have a contact area of less than 100% because of the creation of structural bridges. Contact area may even be more than 100% if the arrangement of the protrusions is such that there are protrusions and anchored in opposite valleys, forming a "zipper" mechanism. This theory can be applied for the B type surface but especially for the S3-2 surface.

<div align="center">a) 100 %   b) < 100 %   c) > 100 %</div>
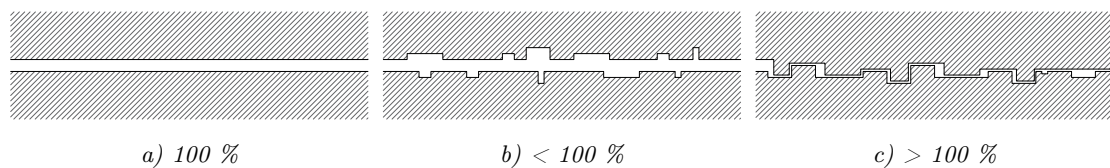
Figure 26: Scheme of possible contact area

The protrusions also occurred in a sort of periodic pattern that corresponded with the wave effect on surface type S3-2 and the infill pattern. After printing only the infill pattern and following further investigation it was clear that this periodic occurrence corresponds to the shape of the infill pattern. In conclusion, it is important to note that all the above issues are related to the specific printer, set parameters and configurations that have been used.
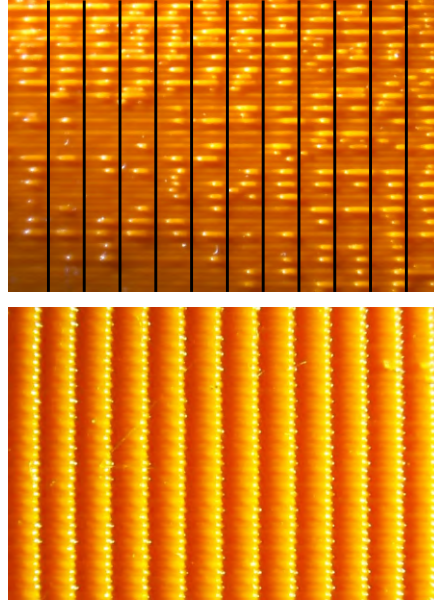
Figure 27: Marked periodic appearance of spots on S2 (top), Printed internal infill pattern (bottom)

In conclusion, it is important to note that all the above issues are related to the specific printer, set parameters and configurations that have been used.

4   Image analysis

4.1   Digital image correlation

Digital image correlation (DIC) is a non-contact optical experimental method that allows measurements and analyses of the motion, and deformation of monitored objects [57]. DIC provides full-field displacement, deformation, and strain measurements, allowing visualisation of measured data across the entire domain under investigation such that it provides us with both, local and average data. It offers several advantages over traditional tools such as strain gauges and extensometers [58, 59]. This is particularly useful for inhomogeneous materials like composites and others, where strain can vary significantly over the investigated surface [28]. The contactless aspect of this technique eliminates the need for physical attachment of specific accessories to the material sample and eliminates the potential side effects due to the attachment inaccuracies. Additionally, this method is easy to set up and provides reliable results compared to conventional equipment [60, 61]. It is also suitable for difficult-to-attach surfaces and reduces the risk of damaging the tool [62]. DIC can be used to accurately measure changes in 2D and

3D space. 3D DIC utilises stereo digital images to measure the displacement, deformation, and strain in space. This method is widely applicable in characterising material behaviour, quantifying material parameters, and validating numerical simulations [63].

DIC involves matching the grey-scale values of pixels on taken images of an object's surface. This process includes correlating grey values to compute shape and surface displacements of selected regions [64–66]. Several types of stochastic patterns are used. The pattern can take the form of random spots sprayed on the surface [67], laser spots [68], fractal surface patterns [69], and simulated random patterns [70]. These patterns are used to match features between reference and deformed state images in order to measure displacements [64–70]. It finds applications in mechanical testing from macro to nano scale. It can be used under both static and dynamic loading conditions [71]. The accuracy of the analysis results is closely linked to the quality and precision of the digital measuring optical equipment and applied pattern.

Standard two-dimensional DIC measurements are carried out following the setup presented in following figure. To ensure accurate results, it is essential to position the camera perpendicular to the surface of the investigated sample. Usually a stable white light source should be used to illuminate the sample [72].

To compute the displacements of the determined points $P[x_0, y_0]$, the reference subset of pixels centred on point P is selected. This reference subset serves as a reference point for tracking its position in the target image. For accurate tracking, it is crucial to establish a criterion for assessing the similarity or dissimilarity between the reference and target subsets. The process involves relocating the reference subset within the search area on the target image. Correlation coefficients are then calculated at each location. The correlation coefficient is computed by iteratively transforming the subset to closely match the grayscale values of the reference subset. The matching procedure is completed by determining the peak position of the correlation coefficient distribution through the chosen optimization algorithm. Once the correlation coefficient's extreme has been identified, the position of the deformed subset can be determined. The difference between the positions of the reference and target subsets provides the in-plane displacement vector. This process is repeated for all monitored pixels, resulting in the complete displacement field [73]. To evaluate the degree of similarity between the reference and transformed subsets, it is necessary to establish predetermined correlation criteria in advance [74–77].
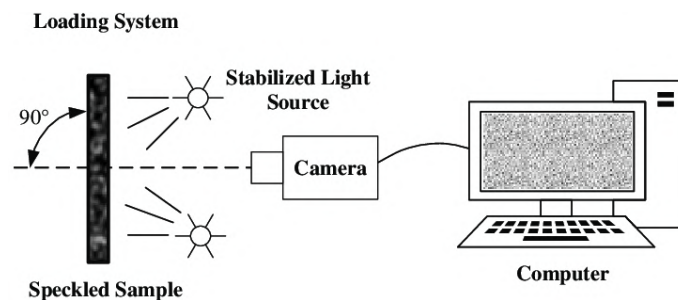
Figure 28: Searching of reference subset values in target image
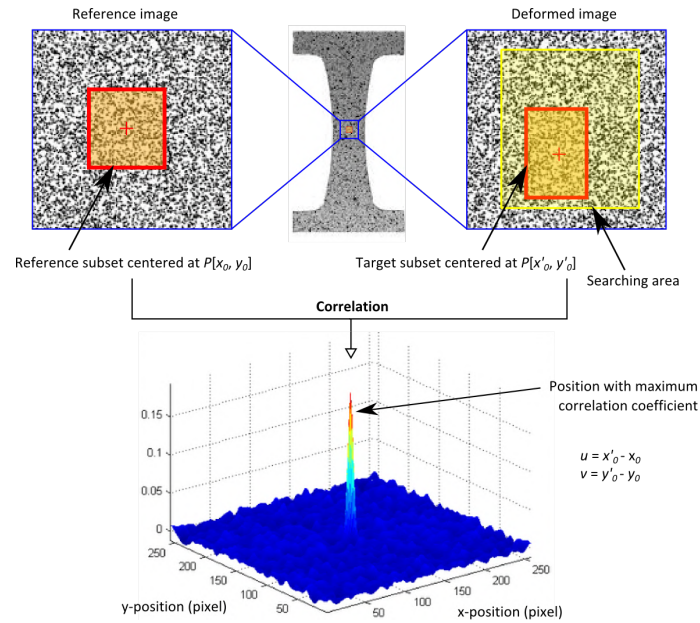
Figure 29: Standard 2D DIC experimental setup

The DIC measurements were evaluated using Ncorr, Ncorr_post, and the Ncorr_post_CSTool tool. These software applications are open source programs based on the MATLAB programming environment. Ncorr is designed for 2D digital image correlation and uses algorithms written in the C++/MEX programming language. MEX stands for "MATLAB executable" and it is a type of computer file that provides connection between MATLAB and functions written in C, C++ or Fortran programming language. MATLAB, provided by The MathWorks, is a programming and computing platform that enables data analysis, matrix operations, simulation, and algorithm generation. MATLAB also offers a range of pre-built tools that are used by Ncorr programmes [78, 79].

4.2   Tracking program

This section outlines the structure and procedures of the tracking program developed in the context of this thesis. This program was primarily developed to acquire desired parameters more efficiently and to overcome certain limitations of the Ncorr DIC program. Currently, the program is primarily dedicated to terminal commands. However, some functions and elements are handled through a graphical user interface (GUI) as well. The program benefited extensively from the use of QR-code, which were used for various kinds of applications to speed up and simplify certain types of repetitive tasks.
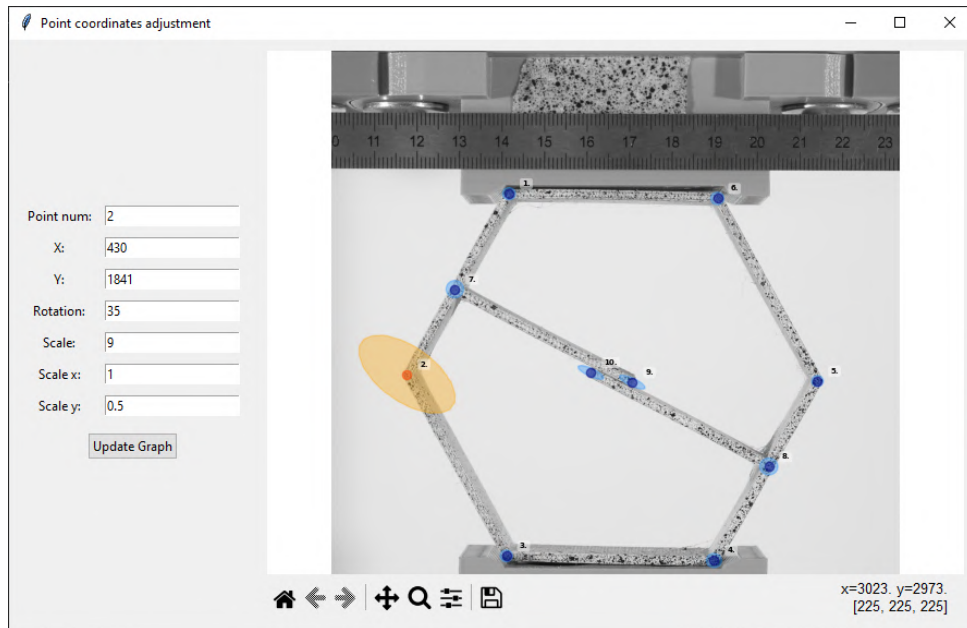
Figure 30: Screenshot from the program GUI of the point adjustment window

4.2.1   Tracking programme architecture

Point tracking program was implemented using the Python programming language. Python is a versatile, high-level, object-oriented, and dynamic programming language that offers a wide range of modules, packages, libraries, and add-ons, making it one of the most multifunctional programming languages of these days [80]. The program was based primarily on the OpenCV and Numpy libraries, with additional use of PyZbar for QR code reading in images and PyGMSH for triangulation of region partitioning. OpenCV and Numpy are open source libraries based on the C and C++ programming language [81, 82]. OpenCV is used for the work with the images while Numpy is used for matrix manipulation and other types of operations. PyGMSH is based on Gmsh which is a powerful open source 3D finite element mesh generator [83]. The GUI is built on the Tkinter library combined with the Matplotlib plotting library. The data export is handled by means of the Pandas library.

4.2.2   QR-Codes in experiments

QR-Code (Quick Response Code) is a standardised 2D matrix-type barcode. It is composed of black and white squares arranged in a regular pattern and offers robust error correction capabilities. QR-Codes can store various types of structured data. The data capacity of the QR code is primarily determined by the selected size style, ranging from 1 to 40. The code structure includes three 'Finder patterns' for localising QR-Codes. These patterns are linked by "Timing patterns" that are designed to rectify potential distortions within the code. For larger codes, an "Alignment pattern" is introduced to enhance distortion correction. To ensure reliable reading, the code should be surrounded by a designated "Quiet zone", which is an empty space that aids in distinguishing the code from its surroundings [84, 85].
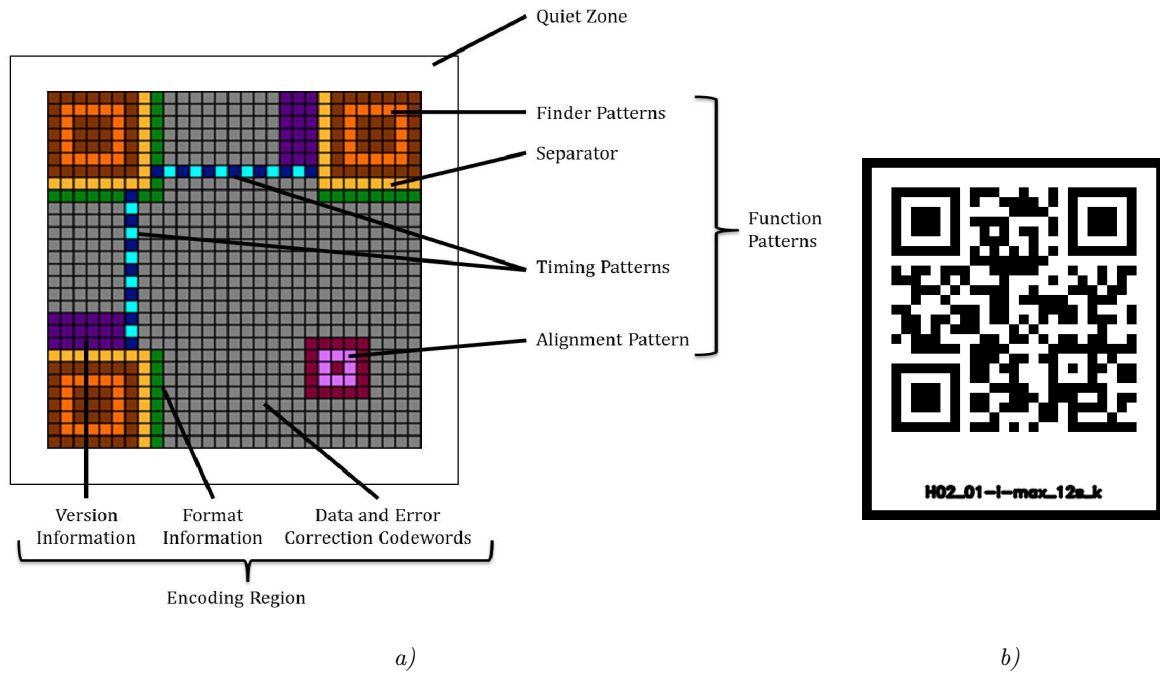
Figure 31: Structure of QR-Code [70] *a), Example of used QR-Code containing the experiment identification and text of containing data b)*

The implemented codes had various purposes within the experimental setup. They were used to display relevant information about the current experiment, such as its classification, name, and type. This feature allowed for a simplified and rapid organisation of the acquired images. The relevant folders corresponding to each experiment were automatically generated, and the images within them were systematically sorted. A further important application was the dynamic tracking of the QR code attached to the sample under observation. The QR-code movement was tracked, providing valuable information about the sample's movement. Additionally, the QR-codes served as markers, serving as reference objects to determine the pixel to millimetre ratio. One application involved the use of QR codes as universal reference points for calculating various calibration parameters. These parameters included the quantification of angular differences between the machine with the specimen, loading bar of machine, and the used camera. QR codes have been found to be versatile in facilitating and automating certain tasks. They have proven to be a suitable universal tool in the detection of certain calibration procedures.
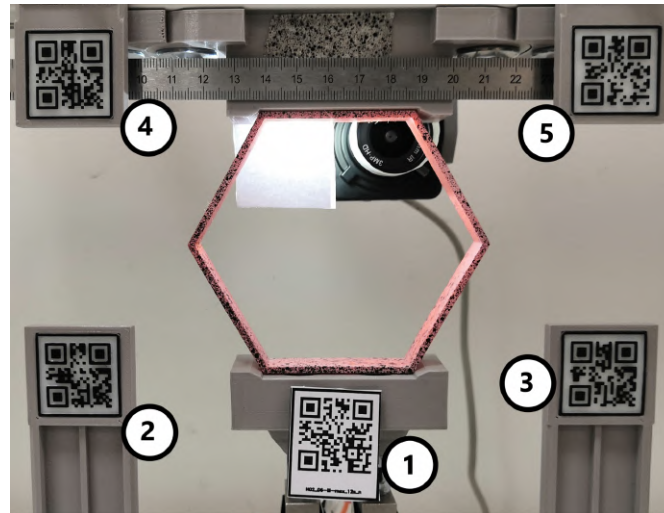
Figure 32: QR-Codes used in experiments: 1 - experiment identification, 2 - First calibration point of machine base, 3 - Second calibration point of machine base, 4 - First calibration point of the loading bar, 5 - Second calibration point of the loading bar

4.2.3 Programme Structure and Monitoring Mechanisms

The program is divided into individual stages consisting of specific tasks and tracking mechanisms:

1. Initialization and definition of calculation parameters

   a) Defining the regions of interest (ROI) of the non-deforming ares

   b) Defining the regions of interest (ROI) of the deforming areas

   c) Defining the searching points of interest (POI) on the deforming ROI

   d) Setting the calculating specifications

   e) Automatic or manual definition of required parameters

2. Tracking mechanisms

   a) Searching of non-deformed areas

   b) Searching of deformed ROI

   c) Searching of subdivided areas of deformed ROI

   d) Searching of tracked POI

3. Post-processing and corrections of data

4. Saving the calculating data

5. Visualisation of calculated data

6. Data export

The non-deforming ROI is serving the purpose of fast and simple tracking of some moving

monitored parts of the experiments. For example, the position of the loading crossbar or support components. For this purpose, the template matching function, that tracks subdivided rectangular areas of this ROI to capture and reduce potential slight rotation is used.

The deforming ROI is defined by positive and negative polygonal regions that are then subdivided into individual triangles. By dividing this ROI into almost regularly large triangular areas, it can be then ensured that each sub-area has a similar number of keypoints from the SIFT function and the whole ROI is evenly covered. These points are referred to as keypoints. The matched keypoints are sorted based on their similarity, and only those that exceed the set limit are taken. Then, a maximum number of points per triangle area are selected. The deformed shape of the ROI is then determined by calculating new position triangle vertices of these sub-areas. SIFT operates by detecting distinctive key points in the given images based on predetermined parameters. These points are then matched between the individual images. These triangular sub-areas can be furthermore divided into smaller triangular elements that are used for visualisation purposes of displacements of the whole sample.

a)   b)
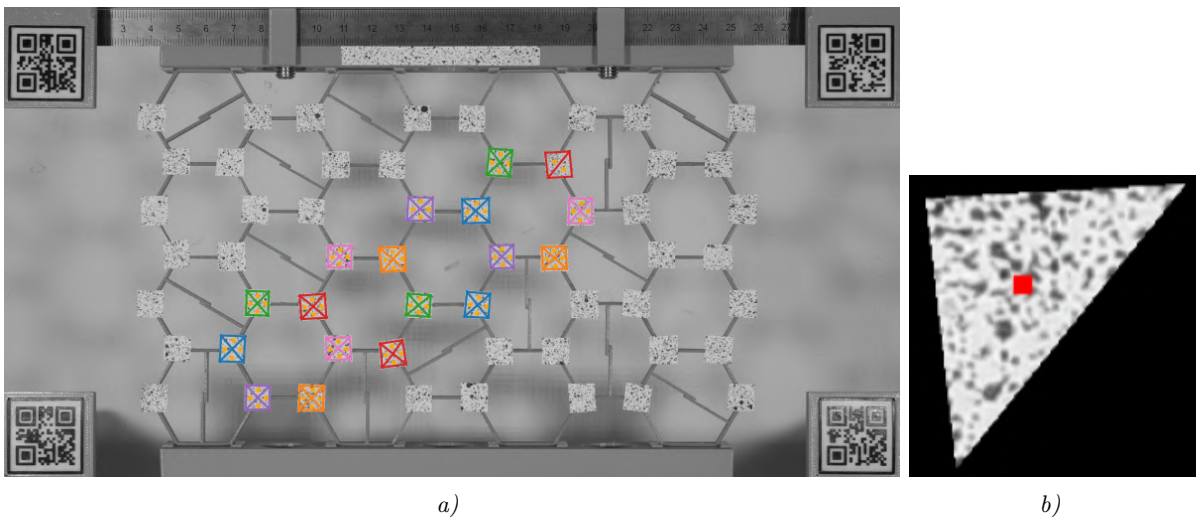
Figure 33: Marked triangulated ROI of first reference image a), one selected masked triangle element of ROI b)

a)   *b)*
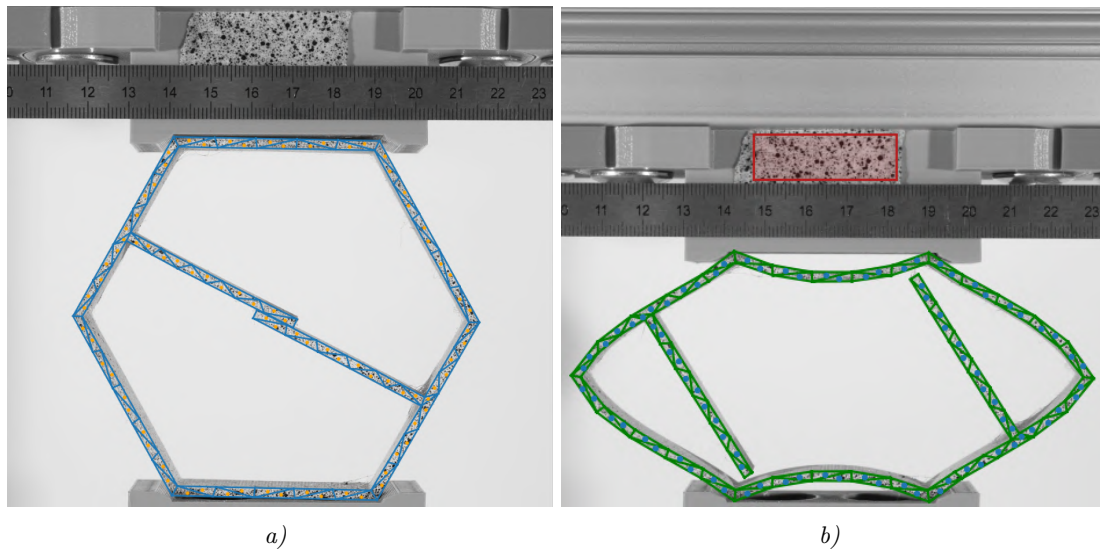
Figure 34: Triangulated deforming ROI: reference image a), last image b)

The POI are defined by the center and surrounding elliptic area. This area is defined to associate the corresponding surrounding keypoints from the SIFT function on the first reference image, which will then be used to find the new location of the tracked centre. Additionally, the rotation of the provided centres is determined based on the keypoints. The space between the marked points can be in the case of large hexagon samples filled with 15 evenly spaced points. These points were created to provide sufficient quantities of comparison points to validate the theoretical simulation.

a)   *b)*
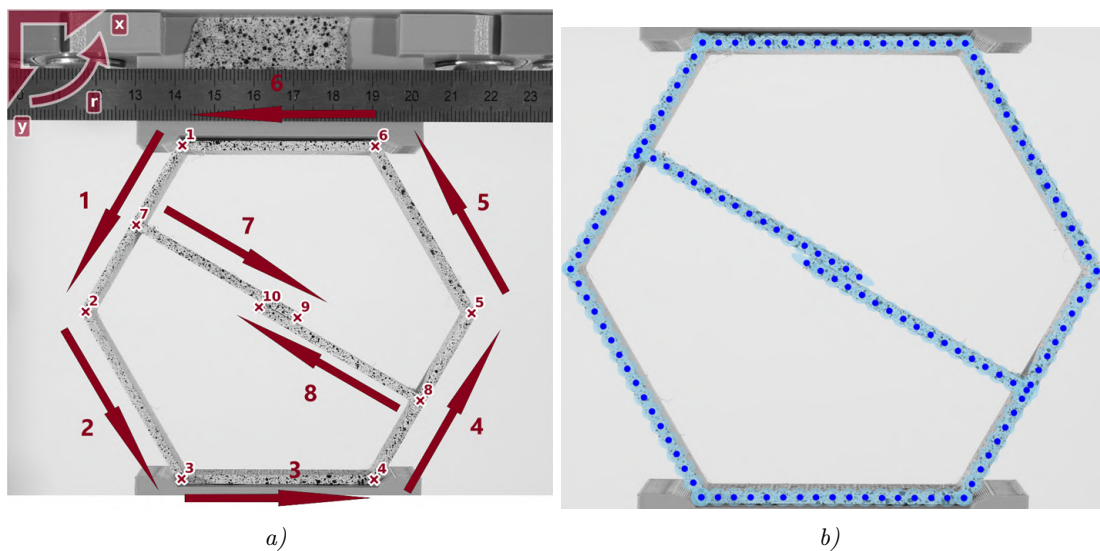
Figure 35: Directions of division of space between marked points a), Resulting marked points b) (dark blue) with corresponding elliptic area (light blue)

TThe settings of the calculating specifications are the conditions and parameters of diving the both types of ROI, selected folders and corresponding images, selection of methods of tracking and their corresponding parameters. Certain parameters can be defined automatically, but user intervention is necessary in case of any issues. This includes for example determining the scale

and points for the machine angle.

The acquired coordinates of the positions of the found points are transformed using a rotational transformation matrix. This fixes the vertical alignment based on the relative angle of the machine to the vertical axis of the tracking camera. The data is converted to real-world units using the pixel-to-millimetre scale. Additionally, the displacement data of the loading bar during the loading sequence has been corrected, due to the potential inaccuracy in the machine's displacement values. During the initial stages, a bug in the machine's software caused a deviation between the theoretical machine displacements and their actual values.

All calculated data are compiled into a single ZIP file, which includes the utilised images, a complete information log detailing the performed calculations, saved data in the H5 file format, and an associated CSV file documenting the experimentally measured forces and displacements. The H5 format is the fifth version of the open source Hierarchical Data Format file format. It can be found as HDF5. HDF5 utilises a file-directory-like system to organise various types of structured data, including metadata. The main advantage is the support of large, complex and heterogeneous data. Additionally, it supports various types of compression [86]. H5 is an independent platform, allowing for seamless use across various operating systems and hardware platforms. The data is exported to a CSV file for validating theoretical models and other related purposes. All the data plots have been done by the versatile Matplotlib library.
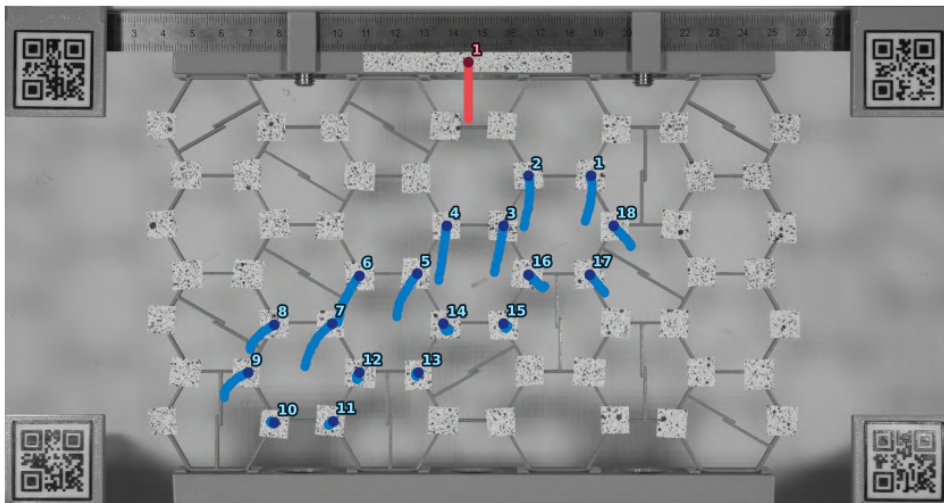
Figure 36: Visualised traces of tracked points (blue) and loading bar (red)

4.2.4   Algorithms and Detection Methods

The detection algorithm combines the `SIFT` point search function and image correlation referred to as `template matching`. Both these detection methods work on images that have been transferred to grey-scale values, Fig GS. OpenCV offers many types of template matching methods. All of them work by comparing the template image to each pixel of the source image. Output of this method is a matrix of similarity that is of the same shape as the reference image,

Fig HM. The chosen method was `Normed Correlation Coefficient` that is defined as:

$$R(x, y) = \frac{\sum_{x',y'} (T'(x', y') \cdot I(x + x', y + y'))}{\sqrt{\sum_{x',y'} T'(x', y')^2 \cdot \sum_{x',y'} I(x + x', y + y')^2}} \tag{1}$$

,where

$$T'(x', y') = T(x', y') - \frac{1}{(w \cdot h)} \cdot \sum_{x''} \sum_{y''} T(x'', y'') \tag{2}$$

$$I'(x + x', y + y') = I(x + x', y + y') - \frac{1}{(w \cdot h)} \cdot \sum_{x''} \sum_{y''} I(x + x'', y + y'') \tag{3}$$

, where I is source image, T is template image, x and y are coordinates of pixels on source image, x', y', x'' and y'' are coordinates of pixels on template image.

The equation (1) gives values from -1 to 1, where -1 means complete dissimilarity and 1 means perfect similarity. An example of the detected template can be observed in the non-deforming region in the initial and final image of the experiment. The correlation values obtained are visualised in following figure, where they have been normalised to a range of 0 to 1 for better visual readability. To highlight the region with the highest correlation value in the final image. The selected region with the highest correlation value in the last image is shown in the 3D plot in following figure.
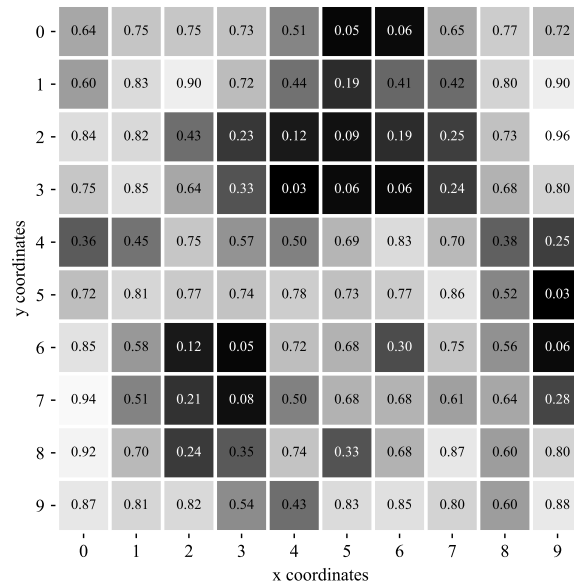
Figure 37: Selection of image converted to grey-scale values
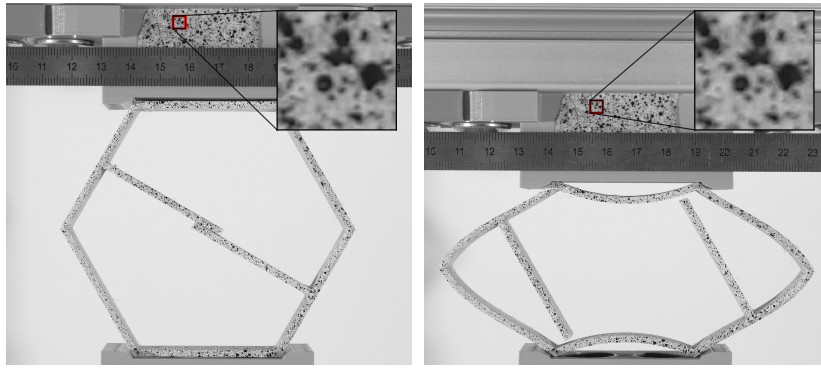
Figure 38: Marked area on reference image (left) and found area on last image (right)

a)   b)
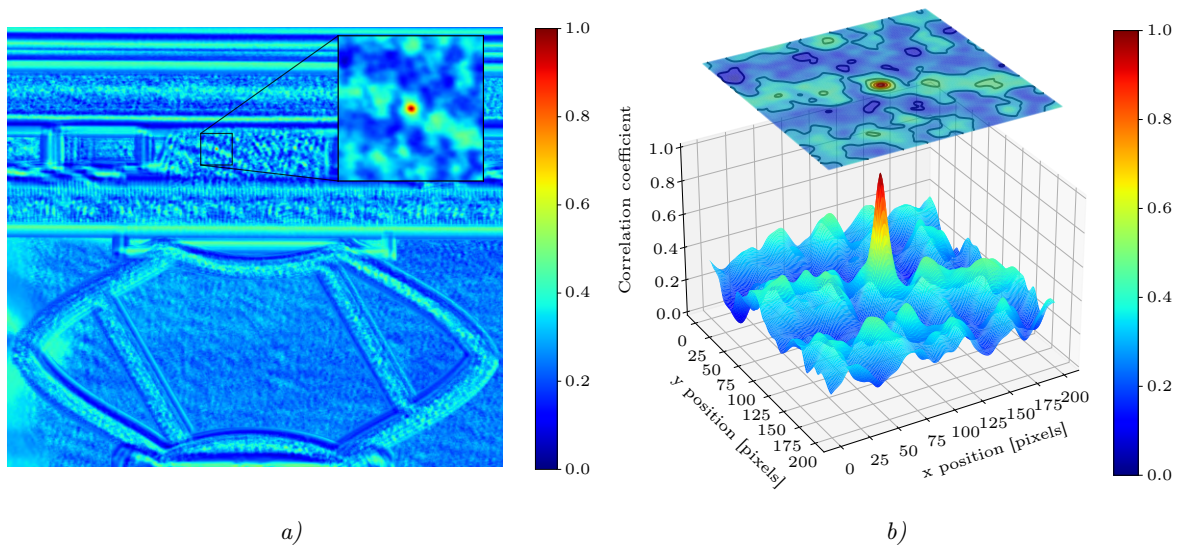
Figure 39: Correlation coefficient of searched area: a) Heatmap of correlation coefficient values of searched area in every pixel of searched last image, b) Correlation coefficient values of selected area of searched last image

The Scale Invariant Feature Transform (SIFT) algorithm is a very powerful image detection tool. The SIFT algorithm can also be used to match points on given images or can be used in real-time object recognition systems [87]. Its versatility is demonstrated by its robustness to various factors such as changes in image size, lighting conditions, noise, perspective distortion and rotation. This algorithm specialises in extracting key points and their corresponding descriptors from images [88–90]. The descriptors are created based on the grey-scale values of the image. Descriptors are used to describe and characterise keypoints in images. These descriptors contain details of the point and its surroundings.The area surrounding each point measures 16×16 pixels and is divided into 16 smaller sub-blocks of 4×4 pixels. An orientation histogram is produced based on the direction of the gradient of the grey values of the pixels in each of these sub-blocks. The histogram consists of eight bins. This process results in a total of 128 values, which are then used to create a vector representation of the point of interest. By using these descriptions, points can be efficiently compared and connected, allowing for the identification of features that match across different images. Distances between descriptors are

30

used to evaluate matches. If the distance ratio between the highest and second highest match is at least 0.8, these points are discarded. Such a high match ratio can be caused by noise or other effects. SIFT utilises a filtering technique in the scale space by employing a Laplacian of Gaussian (LoG) to handle scale differences. This is similar to a scale-adaptive blob detection method. The LoG operates by modifying the scale parameter (σ) to detect points of varying sizes. This is estimated by computing the Difference of Gaussians (DoG) for different octaves in the Gaussian pyramid. The algorithm subsequently identifies local extremes in scale and space that mark potential key points. Taylor's series of scale space extensions is used to determine potential keypoint locations. The values of a given location are determined based on the intensity satisfying the specified criteria [89, 90].

a)

b)
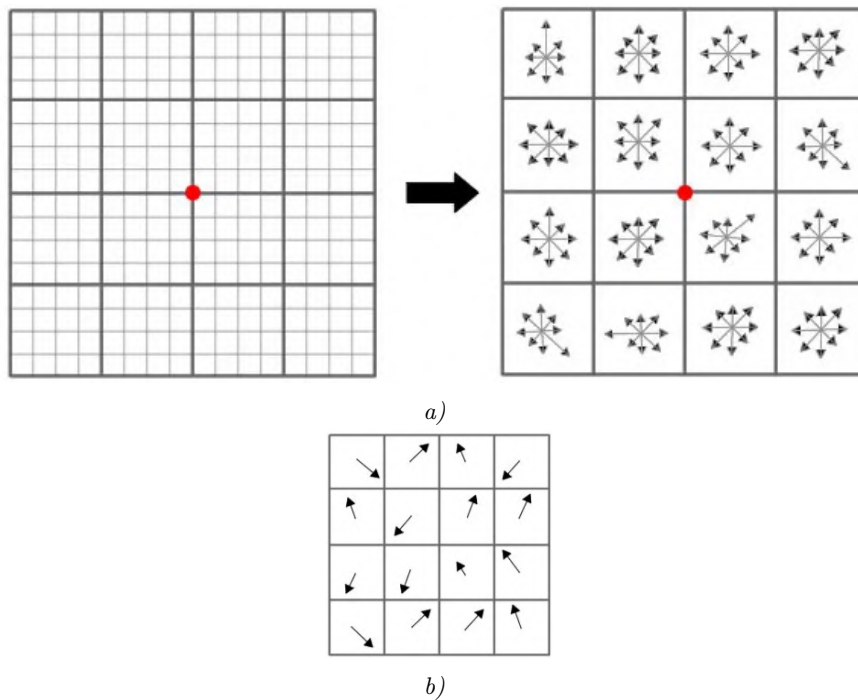
Figure 40: Method of creating the gradient values to determine the descriptor of keypoint (red point). Gradient values and direction are illustrated by the arrows [89].
a) 16 × 16 window (left) and 128 dimensional vector (right), b) 4 × 4 sub-block

As previously stated, these keypoints are used to calculate new positions of searched points. This is done by using selected points within a predefined area around each search point. New positions of the points are found based on the homography matrix. This matrix consists of the coordinates transformation and scale parameters. This is achieved using the RANSAC (Random sample consensus) method with n pairs of corresponding points (x_i, y_i) and (x'_i, y'_i). The objective is to minimise the transformation error by optimising the 9 unknown elements h_{ij} values of the homography matrix H. The first panel contains a set of points $P_i(x_i, y_i)$, while the second panel contains a set of points $P'_i(x'_i, y'_i)$. This matrix is found by using the `findHomography` function in OpenCV. The homography transformation between these points is given by the following relation [91]:

$$\mathbf{P'} = \mathbf{H} \cdot \mathbf{P}$$

$$\mathbf{H} = \begin{bmatrix} h_{11} & h_{12} & h_{13} \\ h_{21} & h_{22} & h_{23} \\ h_{31} & h_{32} & h_{33} \end{bmatrix}$$

The rotation of the found point is also searched. For this purpose, the `estimateAffinePartial2D` function from OpenCV is used. It is evaluated on the basis of the transformation matrix defined as [91]:

$$\mathbf{P}' = \mathbf{M} \cdot \mathbf{P}$$

$$\mathbf{M} = \begin{bmatrix} \cos(\theta) \cdot s & -\sin(\theta) \cdot s & t_x \\ \sin(\theta) \cdot s & \cos(\theta) \cdot s & t_y \end{bmatrix}$$

, where θ is the rotation angle, s is scaling factor and t_x, t_y are translations in the x, y axes. The matrix is found based on the RANSAC method by minimising the transformation error.

a)   b)
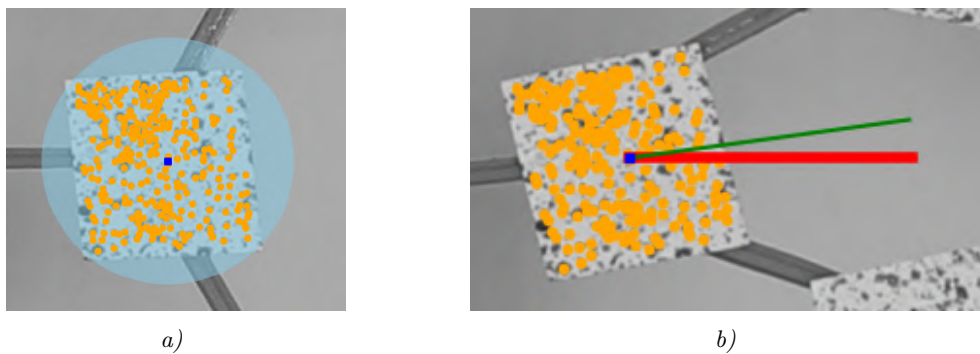
Figure 41: Marked area of usable keypoints (light blue), marked searched point (dark blue) and used keypoints (orange), found searched point on last image with marked used keypoints (orange), original orientation (red line) and new rotated orientation of searched point (green line).
a) reference image, b) last image of deformed structure

4.3   Image distortion correction

There were two types of significant distortions in the images taken by the Arducam camera (this camera is further described in the chapter Experimental equipment). The first was perspective distortion resulting from the tracked sample's movement across the camera's field of view. The first solution for that is to place the camera in sufficient distance to eliminate this effect. That was not possible in this case. Therefore, a different solution, based on eliminating the sample movement across the field of view, was used. The second type of distortion is a barrel distortion caused by the lens curvature. In general, the correcting effort is to place the observed samples to the most undistorted central part of the viewing area of the camera.

The correction process by pinhole camera model goes as follows: Point P is placed in 3D space. This point can be described by a world coordinate with a given origin. Another way of describing the position of a point is by the coordinates of the camera, which has its origin at the viewpoint. The aim is to find the pixel coordinates (u, v) of this point on a projected plane [92].
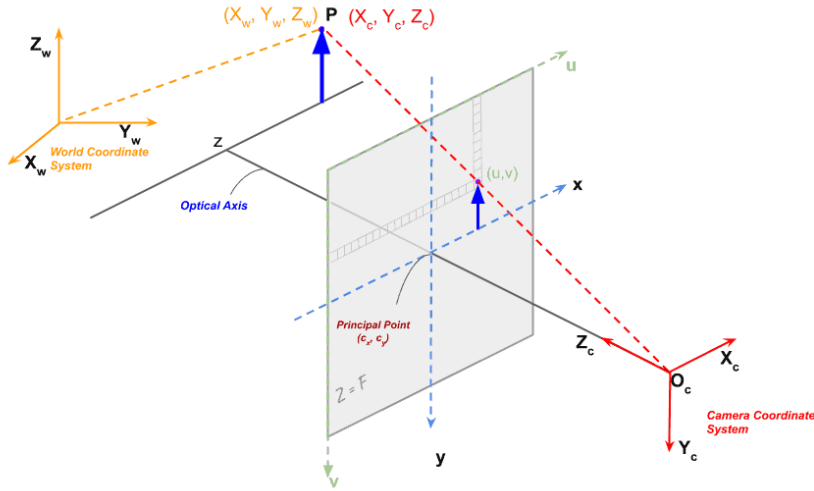
Figure 42: Scheme of coordinates [44]

The relationship between world and camera coordinates is expressed as:

$$
\begin{bmatrix} X \\ Y \\ Z \end{bmatrix} = \mathbf{R} \begin{bmatrix} X_w \\ Y_w \\ Z_w \end{bmatrix} + \mathbf{t} \tag{4}
$$

, where R is rotation matrix and T translation vector and they are stated as follows:

$$
\mathbf{R} = \begin{bmatrix} r_{11} & r_{12} & r_{13} \\ r_{21} & r_{22} & r_{23} \\ r_{31} & r_{32} & r_{33} \end{bmatrix}, \quad \mathbf{T} = \begin{bmatrix} t_x \\ t_y \\ t_z \end{bmatrix} \tag{5}
$$

By combining these two transformation elements we get Extrinsic Matrix of size 3x4 as:

$$
\begin{bmatrix} \mathbf{R}|\mathbf{t} \end{bmatrix} = \begin{bmatrix} r_{11} & r_{12} & r_{13} & t_x \\ r_{21} & r_{22} & r_{23} & t_y \\ r_{31} & r_{32} & r_{33} & t_z \end{bmatrix} \tag{6}
$$

The mathematical expressions that establish a connection between a 3D point $(X_w, \ Y_w, \ Z_w)$ represented in world coordinates and its projection $(u, \ v)$ in image coordinates are:

$$
\begin{bmatrix} u' \\ v' \\ w' \end{bmatrix} = \mathbf{P} \begin{bmatrix} X_w \\ Y_w \\ Z_w \\ 1 \end{bmatrix} \tag{7}
$$

,where

$$u = \frac{u'}{w'} \quad v = \frac{v'}{w'}$$

$$P = K \cdot [R|t] = \begin{bmatrix} f_x & 0 & c_x & 0 \\ 0 & f_y & c_y & 0 \\ 0 & 0 & 1 & 0 \end{bmatrix} \begin{bmatrix} r_{11} & r_{12} & r_{13} & t_x \\ r_{21} & r_{22} & r_{23} & t_y \\ r_{31} & r_{32} & r_{33} & t_z \\ 0 & 0 & 0 & 1 \end{bmatrix} \tag{8}$$

, where K is intrinsic matrix, f_x, f_y are focal distances in x and y directions, c_x, c_y are coordinates of the optical center, r_{ij} are elements of the rotation matrix, t_x, t_y, t_z are translations in x, y, z directions and P is projection matrix.

If the Z direction in the world coordinate is ignored, the 4x3 camera matrix, P, can be reduced to a 3x3 homography matrix, H. A square matrix is able to have its inverse, H^{-1}, which can map a u, v pixel of an image to x, y, 0 coordinate in the world coordinate system as shown below:

$$\begin{bmatrix} X \\ Y \\ Z \end{bmatrix} = H \begin{bmatrix} X_w \\ Y_w \\ Z_w \\ 1 \end{bmatrix} \tag{9}$$

The $k_1 - k_3$ radial distortion coefficients and $p_1 - p_2$ tangential distortion coefficients, as well as the members of the homography matrix, can be obtained through optimization algorithms that minimize the error between calculated distorted points and those obtained from captured images. Once these parameters are obtained, it is possible to calculate the undistorted coordinates of all pixels in the image.

$$x_{distorted} = x(1 + k_1 r^2 + k_2 r^4 + k_3 r^6) + 2p_1 xy + p_2(r^2 + 2x^2) \tag{10}$$

$$y_{distorted} = y(1 + k_1 r^2 + k_2 r^4 + k_3 r^6) + p_1(r^2 + 2y^2) + 2p_2 xy \tag{11}$$

$$r^2 = x^2 + y^2 \tag{12}$$

, where k_1, k_2, p_1, p_2, k_3 are distortion coefficients.

To summarise, the process of camera image calibration in OpenCV using homography involves estimating the homography matrix, retrieving the camera pose, and relating it to intrinsic and extrinsic camera parameters. Image undistortion requires an understanding of radial and tangential distortions, which can be corrected using distortion coefficients and the camera matrix.
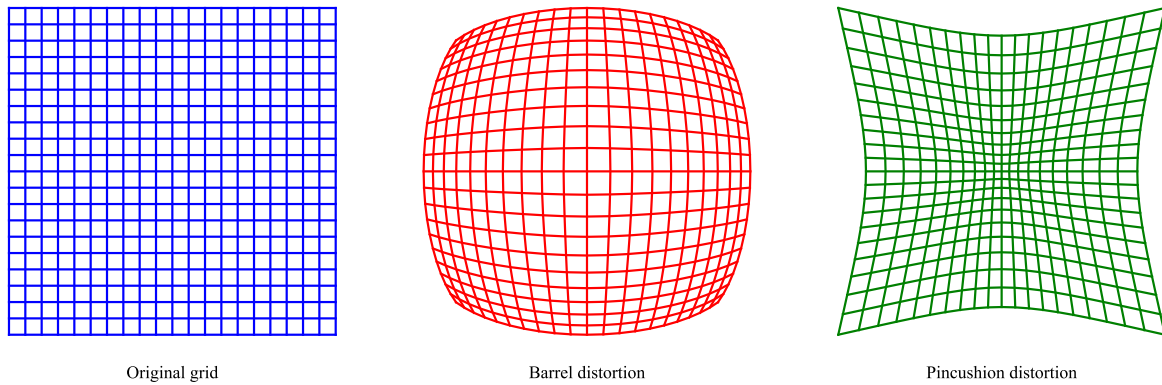
Figure 43: Types of lens distortions shown by deformed grid

An attempt was made to correct the images caused by lens deformation. This was achieved using the calibration *"checkerboard"* pattern and built-in functions `findChessboardCorners` and `calibrateCamera` in the OpenCV library. Calibration was required for each individual lens and resolution setting. A series of 30 images, taken from various angles, was captured for each case. On the images than were used undistort function. The calibration checkerboard were made by a conventional (2D) office laser printer.
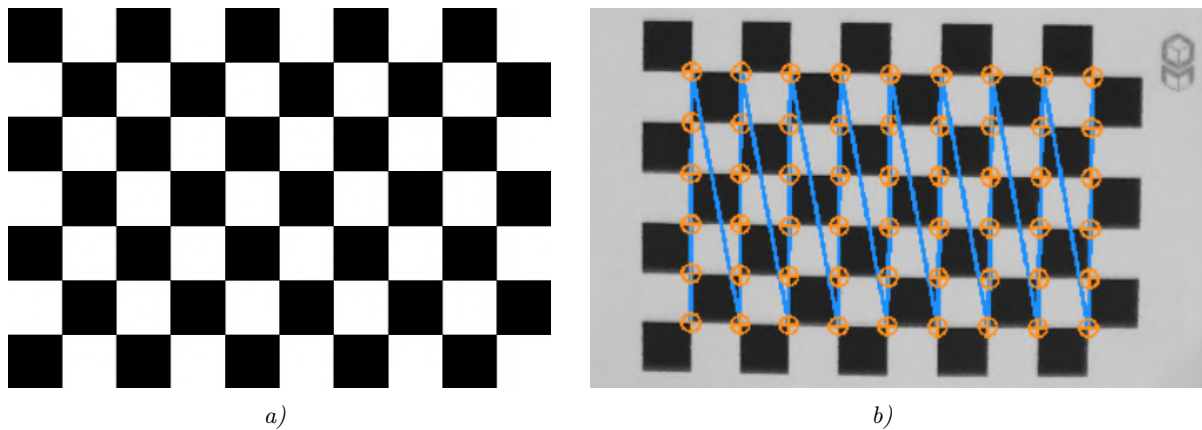
Figure 44: Checkerboard calibration pattern a), Marked found calibration points on checkerboard on taken image b)
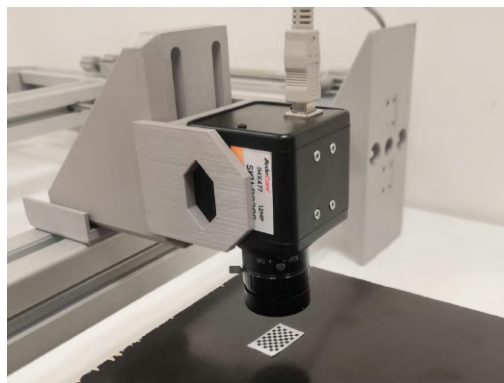
Figure 45: Setup of taking images of checkerboard pattern

<center>a) b)</center>
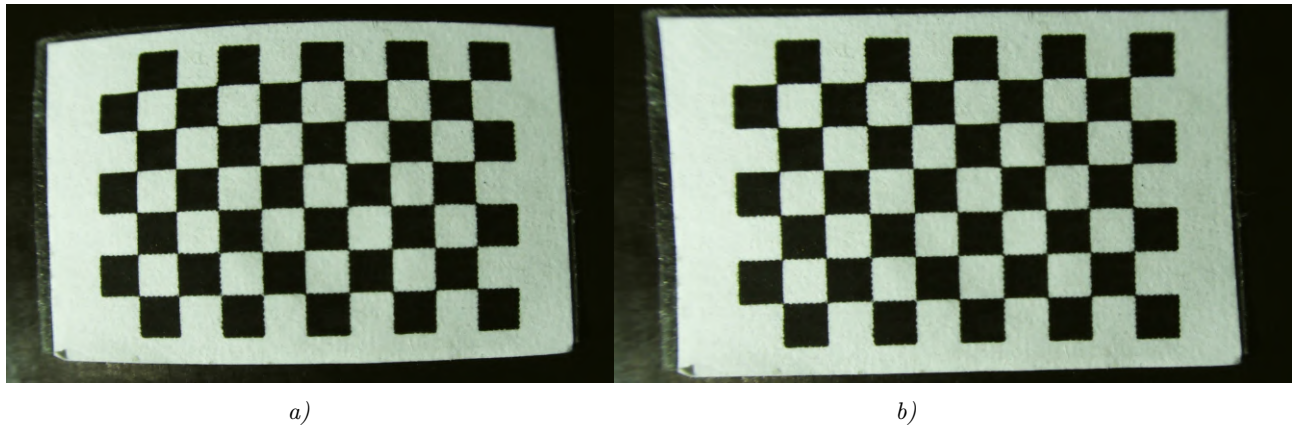
Figure 46: Taken images of checkerboard pattern Before a) and After b) applied distortion correction

The following data and results have been obtained in view of their limited accuracy and the possible influence of external factors. Due to these inaccuracies, the data cannot be considered absolute, but are still valuable for relative comparisons between values. This relative analysis allows for trends and patterns in the data to be identified, although caution must be kept in interpreting absolute values.

5   Experiments

5.1   Description

As stated in the chapter XY, all tested samples were produced using a 3D printer from orange PETG thermoplastic by Prusa Research a.s. All components used to support the samples or for measurement purposes were also created using 3D printing.

The type A cell was tested in 3 orientations. From this it should be ascertained whether the orientation of the individual wall infill has an effect on the resulting stiffness of the cell. Testing of these orientations was carried out by displacing the loading bar by a maximum of 10 mm to avoid plastic deformation of the cell. The cells were then left at rest to eliminate any other residual deformation. Subsequently, the cell was loaded with a displacement of up to 30 mm beyond the elastic deformation limit.Type B cells were loaded in the normal or pre-stressed state. To achieve cantilever snapping, it was necessary to exceed the elastic deformation limit, where the applied load displacement was up to 20 mm.

Because of the manufacturing of the samples using 3D printing, the question arises whether or how much the mechanical properties differ at a given location due to the orientation of the infill. For this reason, two variants of cell A were created for comparison. In the first variant referred to as infill type 1, the orientation of the infill was the same for the whole sample, i.e., a 45° angle in global coordinates. Three types of wall infill arise in this variant. Walls at 30° and 60° angles have the same infill pattern differing only in orientation of the first and last layer. This could result in different mechanical properties of these walls. All these three infills were

tested individually to determine the infill influence. This problem can be solved by using the same pattern orientation to the specific individual wall. The second variant referred to as infill type 2, the 45° angle of the infill was related to the local axis of the given hexagon wall. However, discontinuity of the infill at the corners of the hexagon samples arises due to settings of the Prusa Slicer used to generate the G-Code containing the instructions for the printer as shown in the following figure. Discontinuities could be reduced by setting a larger infill overlap. However, this would significantly alter the infill profile and create surface unevenness, as mentioned in the chapter YY. These discontinuities can significantly change the stiffness and behaviour of the corners. The assumption was that the discontinuities could potentially make the sample less stiff, cause higher tendency to yielding of the material in the corner area or cause total collapse of the sample.

a)   b)   c)
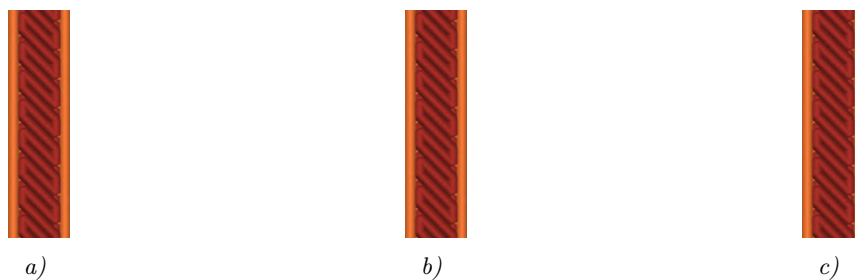
Infill type 1: infill at an angle of 45° to global coordinates. (All walls)

d)

Figure 47: Infill type 2: infill at an angle of 45° to the local wall coordinates. (All walls)

a)   b)

Figure 48: Theoretical model of extruded material of large hexagonal cells with zoomed inset of corresponding printed corners: Infill type 1 a), Infill type 2 b)

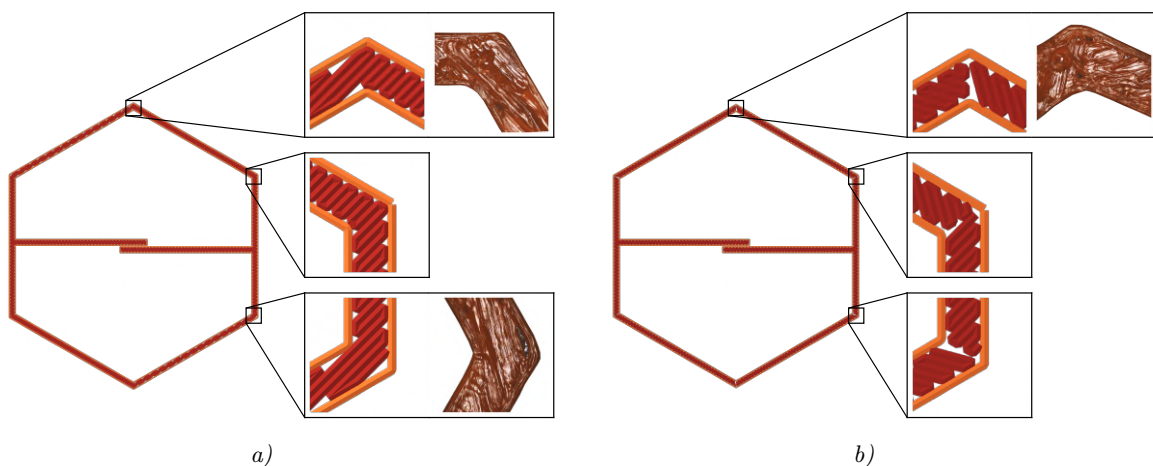Appropriate experiments were performed to determine the parameters of interest for PETG material of the appropriate dimensions and infill type that will be used for mathematical simulations:

- The friction coefficient of the respective surfaces

- Flexural modulus of elasticity

- Young's modulus and tensile strength

- Properties and behaviour of the selected hexagonal cells

- Properties and behaviour of the selected hexagonal cell macrostructure

- Sher tests of the adhered join

Samples will be primarily divided by experiment type and then by internal orientation of the infill in the case of type 1. That will be based on the Roman numerals I-III. A sample marking system is as follows:

- *Wall samples*:
  In the case of friction coefficient measurements, different surfaces of the wall samples are measured. These will be marked with the letter S and a number indicating the given surface, i.e. S1-S4.

- *Tensile samples*:
  The tests will be identified by the letter T, followed by the sample number and a Roman letter indicating the appropriate infill orientation. The samples will be further subdivided according to their size by the letters S and L. The resulting marking of the first small sample shall be: T-01-I_S.

- *Flexural samples*:
  The marking starts with the letter F followed by the sample number and the adjacent orientation. For instance, the first sample of the first orientation of the infill will be marked as F01-I.

- *Large hexagon cells*:
  The tests will be marked with the initial letter H. The measurements of large hexagonal cells will be divided into two series: one for type 1 infill and the other for type 2. The initial series will be labelled as H1, followed by the sample number and orientation type. Following this, the Cell Type letter will be presented, with Type B being divided into two subtypes. The number one will indicate a cell in the basic configuration and the number two will indicate a pre-stressed state. The first example for cell B of the basic configuration is called: H1-01-I_B1. The second series, named H2, will follow a similar pattern to the first series. However the name will be extended by a number at the end to indicate the type of infill. The first sample will be called H2-01-I_1.

- *Macrostructure/aggregate*:
  The samples of the structures will be labelled with the letter M followed by a number indicating the type of sample. Number one will indicate a structure composed of individual cells glued together, while number two will indicate a structure formed as a whole (monolithic). The first sample will be marked as follows: M-01 and M-02.

- *Shear test of joint*:
  The shear tests will be identified by the letter B followed by a number indicating the order in which the tests were performed. The marking of the first sample will be: B-01.

5.2   Experimental equipment

- *Thymos loading machine*

  The testing was done on a custom-build Thymos loading machine created by the Open-Mechanics research group (consisting of members of the Department of Mechanics and the

Experimental Centre of CTU in Prague). This machine consists of a metal frame made of T-slot aluminium profile and other components manufactured using 3D printing. This machine can be set in both vertical and horizontal position. The machine is able to be equipped with up to 3 measuring sensors.

a)   b)
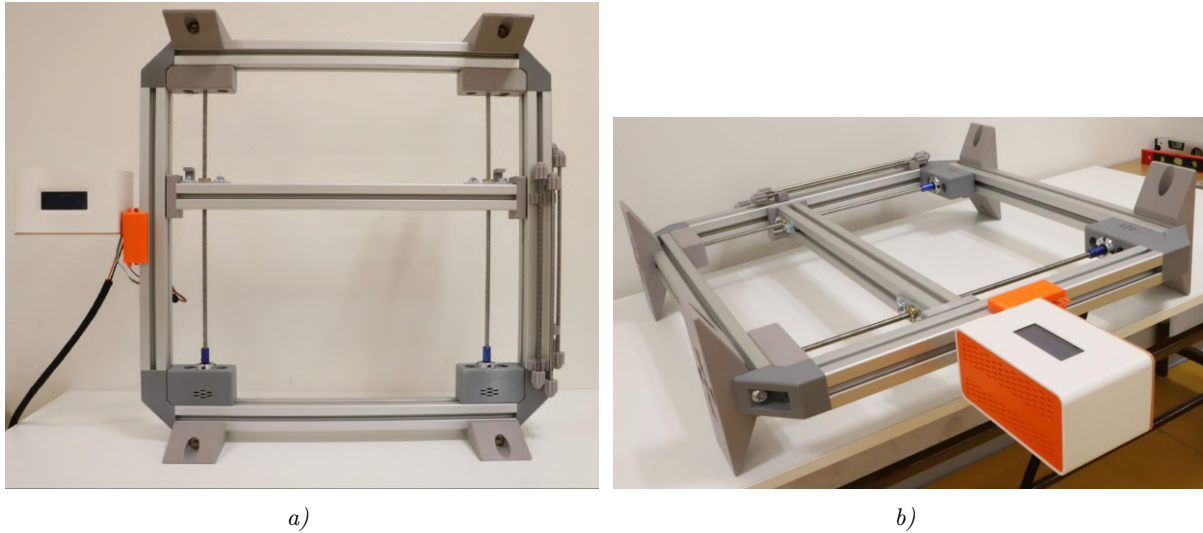
Figure 49: Thymos loading machine in vertical position a), horizontal position b)

Forces were measured by two HT Sensor TAS501N/50kg load cells. These sensors are designed for a maximum load of 50 kilograms, with a safe overload of 120% and a maximum overload of up to 150% of capacity. Sensor error is listed by the manufacturer at around ±0.05% of maximum capacity [93]. During the experiments, the capacity limit was not exceeded. The machine is controlled by a control panel that can be connected to a personal computer via a standard USB Type-A port. The panel consists of a Teensy 4.0 microcontroller, an eight-channel ADS1256 converter and an electrically erasable programmable read-only memory (EEPROM) unit. The control panel can be connected to almost any DSLR camera via a jack connector and converter for the specific camera.

The T-shaped head bolts are used to attach all 3D printed components to the T-Slot aluminium profile frame of the loading machine. The contact area that presses on the load cell is constrained to a circle with a radius equivalent to the width of the load cell. This is done to minimise the external loads, such as flexural moments, and ensure that the transmitted load force is maximally transferred through the center by the steel retaining bolt. The upper fixing bolts are equipped with steel nuts, enabling individual adjustment of the vertical position to level the support components to the desired position.
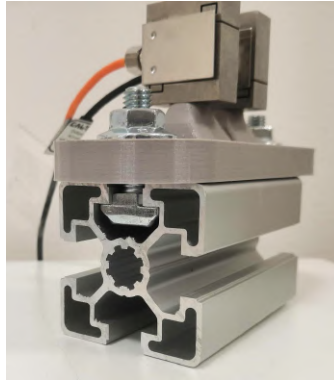
Figure 50: Connection of 3D printed components to the machine frame
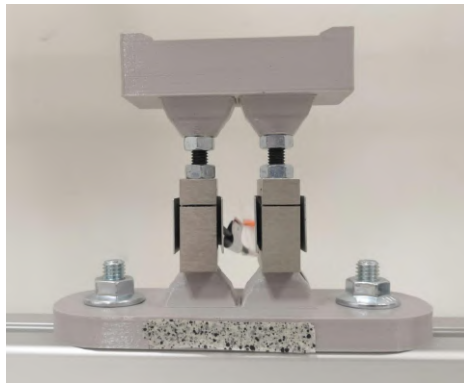
Figure 51: Designed an adjustable levelling system for measuring forces by load cells

- *MTS machine*

  The experiments of tensile properties were performed on a universal testing machine, the MTS Criterion Series 40, model 43 [94].

Figure 52: MTS loading machine [95]

- *Confocal microscope*

The confocal microscope Olympus LEXT OLS5000 was used to analyse the surfaces. The microscope features 5x, 10x, 20x, 50x and 100x zoom LEXT lenses and 1-8 optical zoom. Additionally, it is capable of performing laser 3D surface scanning with a field of view ranging from 16 μm to 5,120 μm [95].
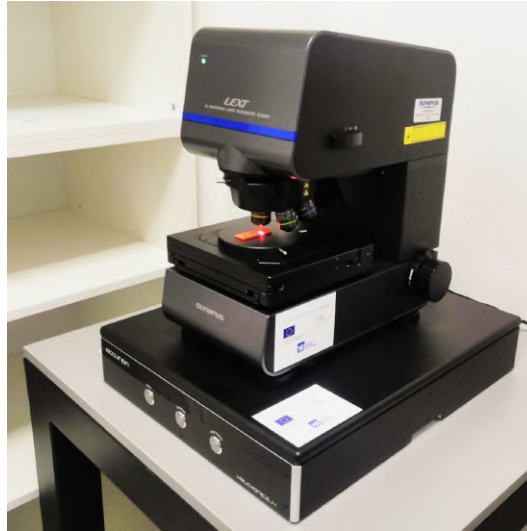
Figure 53: Confocal microscope Olympus LEXT OLS5000

- *DSLR camera*

  For the measurements, the loading setup was equipped with a Canon EOS 6D Mark II digital single-lens reflex camera with CMOS sensor and digital image stabilisation. The camera was also equipped with Canon EF 24-70 mm f/4L IS USM lens [96] and was mounted on a stand-alone tripod.

Figure 54: DSLR Canon EOS 6D Mark II camera

- *Arducam High Quality camera*

  Arducam B0288 12.3 MPx HQ camera [97] with Sony IMX477R stacked, back-illuminated CMOS sensor [98] with ArduCam LN049 varifocal lens 2.8-12 mm [99] for distant capturing and Arducam LN050 lens, 16 mm [100] for close up capturing.
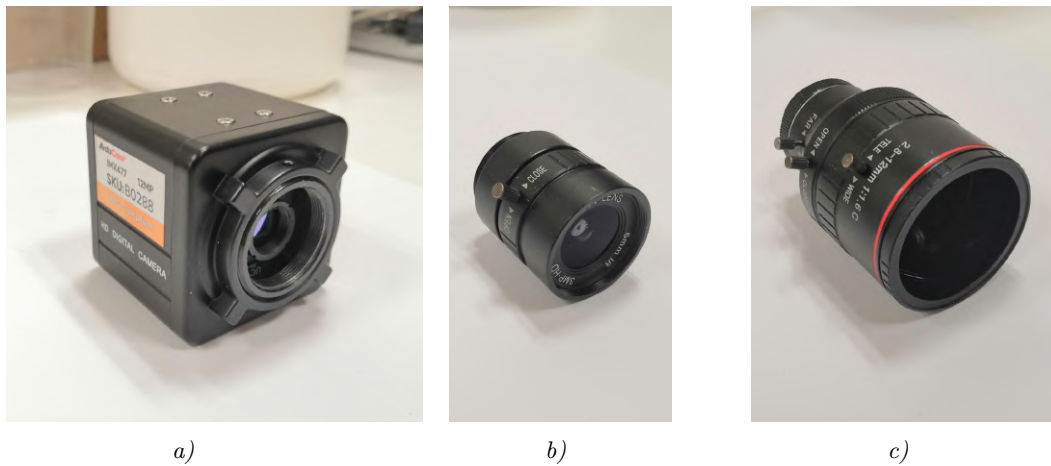
a)   *b)*   *c)*

Figure 55: Arducam camera a), Arducam LN050 lens b), ArduCam LN049 varifocal lens c)
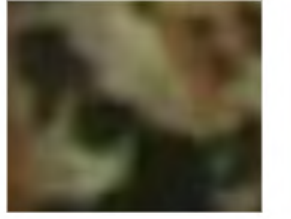
Figure 56: Zoomed images from Arducam camera of individual set resolution in pixels

On the captured images can be seen blocking artefacts resembling known macroblocking effects. This effect is more present on lower resolution images. These artefacts are commonly caused by compression algorithms, in case of JPEG image file format [101, 102]. However these artefacts also appear in other uncompressed image file formats. The cause

42

of that could be the method of capturing and saving photos via the OpenCV library in Python. Taking images by other computer software or using a different camera in combination with OpenCV did not cause this effect. It is assumed that the issue is related to the combination of the used library and the Arducam camera. The exact cause of the effect is not precisely known. It has not been eliminated and has not been further investigated.
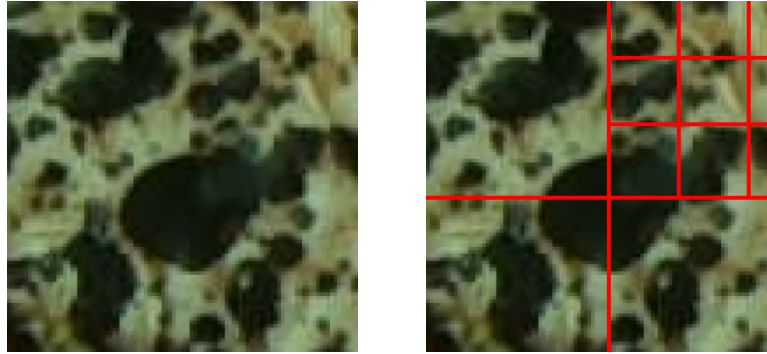
Figure 57: Zoomed images with marked blocking effect on PNG file

5.3   Friction coefficient and Roughness of the sample surface

5.3.1   Definition

One of the parameters of interest was the friction coefficient between two cantilever surfaces. The coefficient of friction (COF) μ is a number expressing the ratio of the frictional resistance force (Fr) and the perpendicular or normal force (N) pushing two surfaces together. Therefore, the resulting equation is:

$$Fr = \mu \cdot N \tag{13}$$
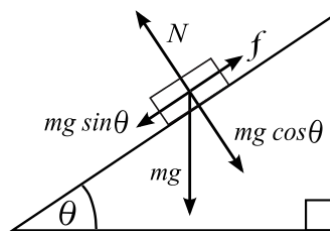
Figure 58: Diagram of the forces acting on the body on an inclined plane [**bibid**]

It is difficult to measure the force of pressure, so instead we consider the force applied by the top object on the bottom by its own weight due to gravity. This force can be referred to as $W = m \cdot g$. This allows us to rewrite the equation as:

$$\mu = Fr/W \tag{14}$$

After the distribution of forces, the force required to overcome the friction coefficient Fr is the friction coefficient times cosine of the angle θ multiplied by the vertical force of the weight of the

object. This gives us the equation as:

$$Fr = \mu \cdot \cos(\theta) \cdot W \tag{15}$$

Another effect is that the gravitational force on the inclined plane also contributes to the force needed to overcome friction. We will refer to this force as Fg. After distributing the forces, we get the following equation:

$$Fg = \mu \cdot \sin(\theta) \cdot W \tag{16}$$

It is therefore clear that the force Fg must be greater than the resisting force Fr in order for the object to start moving. So from the equilibrium position we get the equation:

$$Fr = Fg \tag{17}$$

$$\mu \cdot \cos(\theta) = \sin(\theta) \tag{18}$$

After adjusting the equation, we find that the weight of the object is cancelled out and we get the equation:

$$\mu \cdot \cos(\theta) = \sin(\theta) \tag{19}$$

$$\mu = \frac{\sin(\theta)}{\cos(\theta)} \tag{20}$$

After appropriate adjustments, we obtain an equation where the friction coefficient is equal to the tangent of the angle of the inclined plane:

$$\mu = \tan(\theta) \tag{21}$$

In this equilibrium state, where are object are not in motion relative to each other is considered as *static coefficient of friction* (SCOF) μ_s. The frictional force in motion defined as *kinetic coefficient of friction* (KCOF) μ_k also known as *sliding* or *dynamic coefficient of friction*. Static friction is the result of molecular interactions between the surfaces of touching objects. Different surfaces therefore produce different amounts of static friction. (DCOF). The required force for sliding the object is in motion lower than at the initial state. Therefore KCOF is usually lower than SCOF [103]. This is because after the initial frictional force has been overcome, the microscopic irregularities become less significant, reducing the overall friction.

The KCOF can be obtained from Newton's 2nd law in the direction of sliding:

$$\sum F = m \cdot a \tag{22}$$

,therefore:

$$(m \cdot g) \cdot \sin(\theta) - Fr = m \cdot a \tag{23}$$

$$(m \cdot g) \cdot \sin(\theta) - \mu \cdot FN = m \cdot a \tag{24}$$

$$(m \cdot g) \cdot \sin(\theta) - \mu_k \cdot (m \cdot g) \cdot \cos(0) = m \cdot a \tag{25}$$

After adjusting the equation by cancelling the mass we get the form:

$$g \cdot \sin(0) - \mu_k \cdot g \cdot \cos(\theta) = a \tag{26}$$

That can be written as:

$$\mu_k = \frac{g \cdot \sin(\theta) - a}{g \cdot \cos(\theta)} \tag{27}$$

or

$$\mu_k = \tan(\theta) - \frac{a}{g \cdot \cos(\theta)} \tag{28}$$

After substituting into the equation the values of the initial state, when the motion, thus also the velocity, is zero, we get the following form:

$$\mu_k = \tan(\theta) \tag{29}$$

It can be seen that we get the same equation as for static friction. Further, the validity of the statement that the KCOF is usually smaller than the SCOF can be observed. This is because of the reduction of this value due to the effect of velocity.

5.3.2   Experimental setup

It was decided to measure the coefficient of friction on samples corresponding to the dimensions of the hexagon walls. This dimension was chosen because of the assumption that smaller, i.e., lighter, specimens would be more susceptible to external influences. External influences could be, airflow, vibrations, static electricity, dust, moisture or grease on the sample surface. Three types of surfaces were measured.
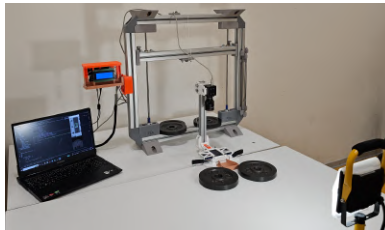
Figure 59: Friction measurement experimental setup

Measurement setup was designed to determine the appropriate angle, which was then converted to a friction coefficient under dry conditions. The machine and measuring equipment were

installed on separate tables, in order to eliminate vibrations caused by the movement of the machine's electric stepper motors. The tables and the machine were also weighed down by metal weights. The measuring assembly consists of a moving stand connected by a string to a stabilised angular apparatus. The angle apparatus consists of a tracking camera, sample storage area and an angle measuring device. The apparatus is fixed with a hinged joint allowing only rotation. One specimen is firmly placed in the apparatus while the other one is loosely placed on top of the bottom sample. The top sample is equipped with a QR-Code indicating the name of the sample and also serving as a reference marker to monitor movement of the top sample and for determining scale from pixels to millimetres.

a)   b)
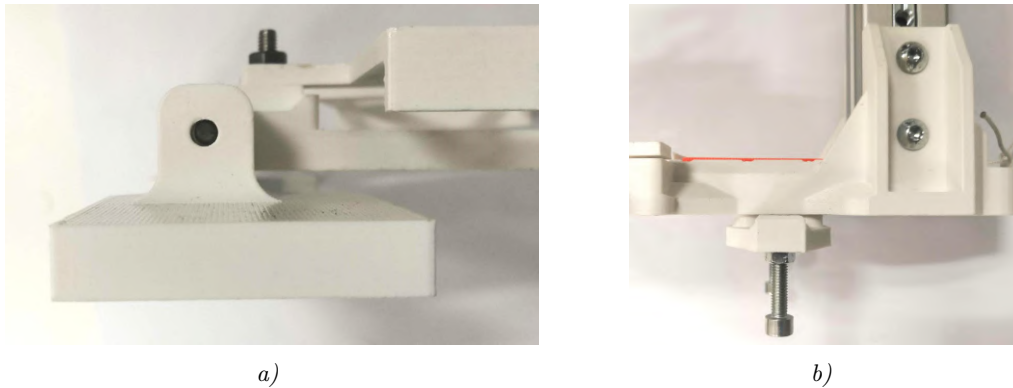
Figure 60: Fixed joint a), adjustable levelling metal bolts of angle measuring apparatus b)

Figure 61: Used angle measuring apparatus

The apparatus is slowly lifted in periodic intervals by the machine. The angle was measured using a combination of gyroscope and accelerometer sensors in the smartphone. This method of measuring angles eliminates errors caused by string stretching, knot slipping, and other external factors. Additional errors could occur when evaluating the angle by measuring the relative distance of the apparatus from the machine and calculating the lengths and angles of the string. This measurement method is independent of the output values from the machine, which may also contain errors. After covering a certain distance, the movement stops to allow the accelerometers to settle and give the specimen time to slide. The slow movement also minimises occurrence of vibrations. Because of that, the measurement was very time-consuming. Due to time constraints, an insufficient number of measurements were taken to accurately determine the statistical deviation of the resulting frictional coefficient of each surface type.

Two types of experiments were performed. The first is to detect SCOF and the second is to detect KCOF. The first type consisted of a random combination of top and bottom samples of the same surface. A random combination was used to obtain general unbiased results. Both samples had the same dimensions, therefore the contact area was reduced immediately at the start of the movement. At the same time, the moving sample could only balance on the edge of the lower sample. The movement of the sample at this point is influenced by free fall. These measurements were taken with the camera set to 1920x1080 resolution with 60 FPS (frames per second). The second type of measurements were done with one bottom sample. This sample is supposed to be of the same surface type as S3-1. The length of the bottom sample was increased in the direction of movement of the top one. The analysis to determine the KCOF was performed only for cases where the specimen slipped during a resting pause and not during machine movement. The analysis was performed on images with applied distortion correction. To obtain more detailed sample tracking, the camera's highest possible 100 FPS was used for these measurements. As a result, the resolution had to be reduced to 1280x960 due to the camera's technical limitations.

Figure 62: Bottom sample for KCOF measurements

From tracking of the QR-code label and known set FPS is it possible to determine the position of the sample in time. Based on that, it is possible to calculate velocity and acceleration. Velocity can be calculated as:

$$v = \frac{ds}{dt}$$

where Δs is the change in position and Δt is the change in time between two points.

Acceleration can be calculated as:

$$a = \frac{dv}{dt}$$

where Δv is the change in velocity and Δt is the change in time between two points.
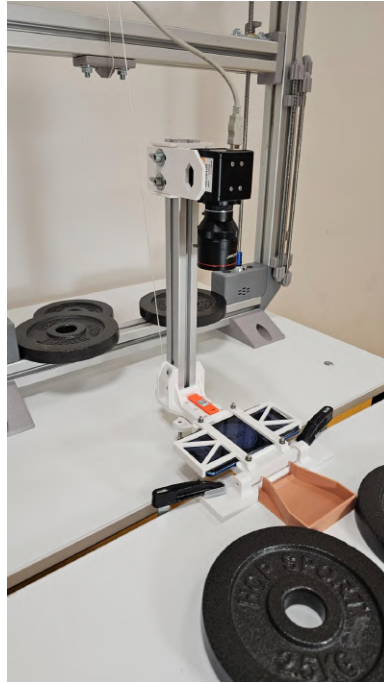
Figure 63: Angle measuring apparatus

5.3.3 Measured data and results

The contact surface area of specimen S1 was compared to the surface of individually printed wall specimens using a confocal microscope to determine its suitability for coefficient of friction tests. Due to the unreliability and inaccuracy of measurements taken with the 5x and 10x lenses, all measurements were conducted using a 20x zoom lens. This resulted in high-resolution measurements of detail, although a very limited field of view of approximately 650 $\times$ 650 μm.

a) S1   *b) S2*   *c) S3-1*
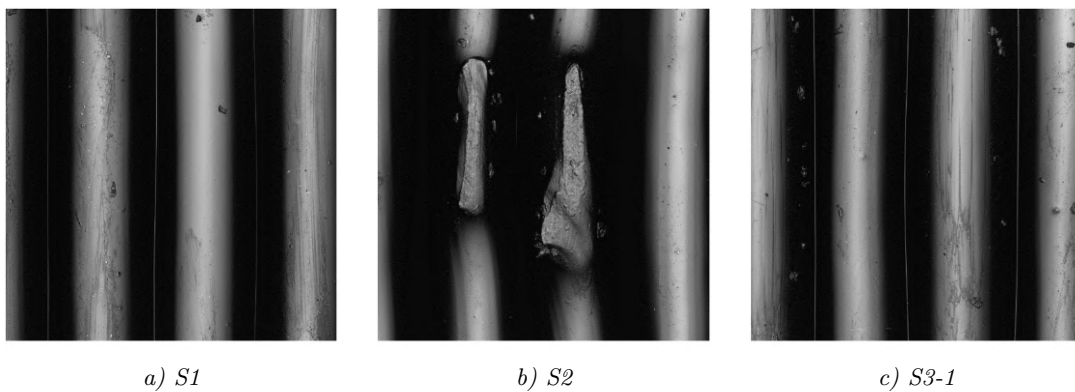
Figure 64: Images of laser reflection intensity from confocal microscopy of reviewed samples surfaces

a)   b)
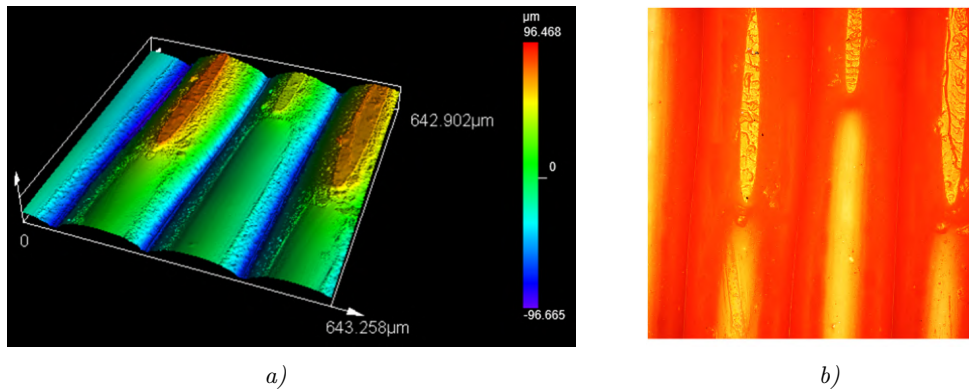
Figure 65: 3D scan of surface S2 by 20x zoom lens after applying a spike reduction. 3D scan a),
captured image of sample

The Gaussian (cut-off) filter λ_c was chosen based on the standard ČSN EN ISO 21920-1, 2, 3 [104–106]. Due to the limitations of the microscope and the maximal observed area of approximately 650x650 μm, the cut-off filter was set to 250 μm. This means that the waviness of the surface is included in the roughness, which is desired. This filter was set for all measurements and the resulting data are used only for relative comparison. All the measurements were performed on the same microscope. Average distance between surface peaks and valleys is 0.1997 mm which corresponds with the set 0.2 mm layer height from Table XX. These surface profiles are shown below:

a)

b)
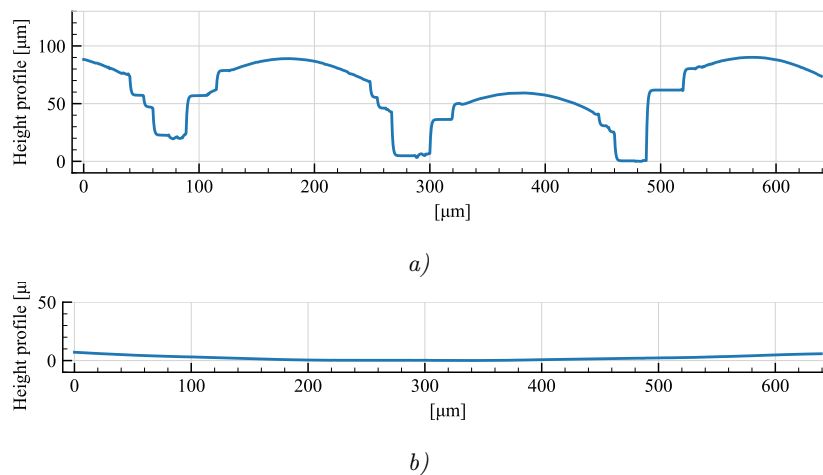
Figure 66: Height profiles of selected of sample S1 cross sections: transverse a), longitudinal b)
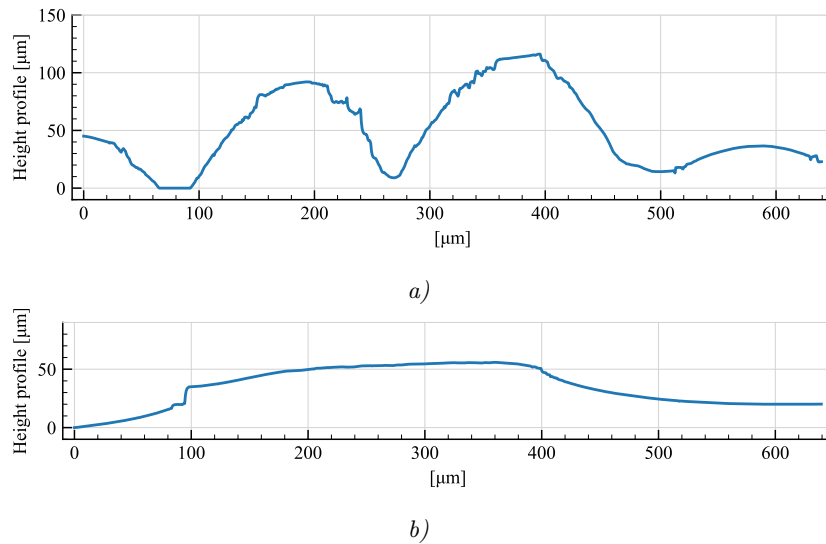
Figure 67: Height profiles of selected of sample S2 cross sections: transverse a), longitudinal b)
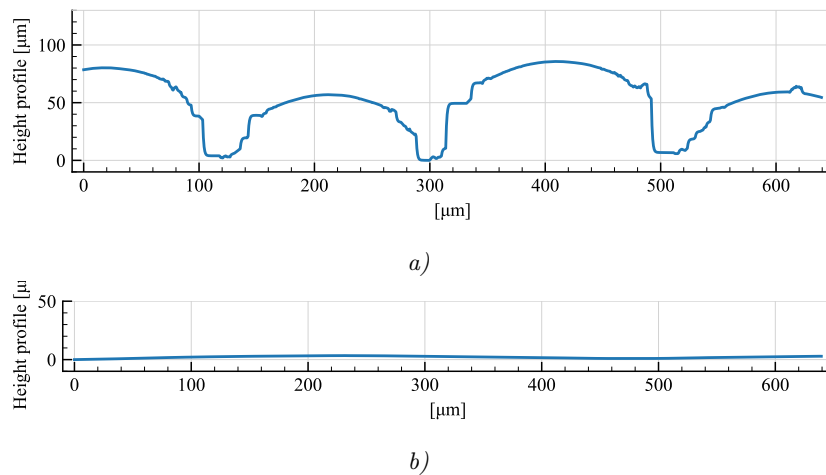
Figure 68: Height profiles of selected of sample S3 cross sections: transverse a), longitudinal n)

The following parameters were used to represent the surface roughness [101]:

- Ra (average roughness) represents the average deviation of the surface profile from its mean line within a given sample length. It is calculated by measuring the arithmetic mean of the absolute values of these deviations.

- Rz (maximum profile height) measures the vertical distance between the highest peak and the lowest valley within a given sampling length. It provides information on the most significant surface irregularities.

- Rt (total profile height) quantifies the total vertical distance between the highest peak and the lowest valley within a given section of the profile. It provides an indication of the overall surface roughness.

- Rsm (root mean square roughness) is a statistical parameter that describes the distribution of irregularities across the surface. It reflects the texture and structure of the surface. Rsm is calculated by taking the square root of each deviation, averaging these square roots and then taking the square root.

The roughness values were evaluated as the average of three sections and are presented in the

following format: *transverse | transverse*

Surface	Ra [µm]		Rz [µm]		Rt [µm]		Rsm [-]	
S1	12.027	0.364	52.327	2.829	63.013	4.091	83.967	61.642
S2	15.254	1.778	61.553	10.732	68.742	16.523	78.994	72.312
S3-1	11.389	0.418	52.722	2.427	58.117	4.849	122.940	31.427
S3-2	11.378	0.388	54.839	2.092	64.946	4.255	133.175	43.030

Table 2: Average measured of each surface type and cross-section roughnesses

The average transverse roughness Ra is around 12 μm, which corresponds to values determined by other researchers [107]. Not enough surface measurements of the samples were taken. However, based on these roughness measurements, it was determined that the individually printed sample S3 was equivalent to the surface of sample S1 and therefore suitable for the coefficient of friction tests. The measured average angles are:

- **S2**: $23.007^o \pm 3.849$
- **S3-1**: $27.034^o \pm 5.098$
- **S3-2**: $25.442^o \pm 4.874$

Resulting static coefficient of frictions are:

- **S2**: 0.427 ± 0.085
- **S3-1**: 0.516 ± 0.118
- **S3-2**: 0.48 ± 0.106

5.4   Tensile material characteristic

5.4.1   Description and Experimental setup

An experimental test was performed to determine the strength and Young's modulus of the material and the corresponding orientations of the infill. The dimensions of the specimens are based on the proportional dimensions of the Type 1B dog-bone shaped specimen specified in ČSN EN ISO 527-1, 2 [108, 109]. The final theoretical cross section was determined as 2.5×16 mm. Two types of samples were created to potentially eliminate and determine the influence of printing and infill. One is based on the standard dimensions. The other has identical dimensions except the linear straight part of the specimen has been extended to match the length of the hexagon wall (50 mm). The tests were performed on the MTS machine. The test speed was set at 2 mm/min and photos for the following DIC analysis were taken every second.
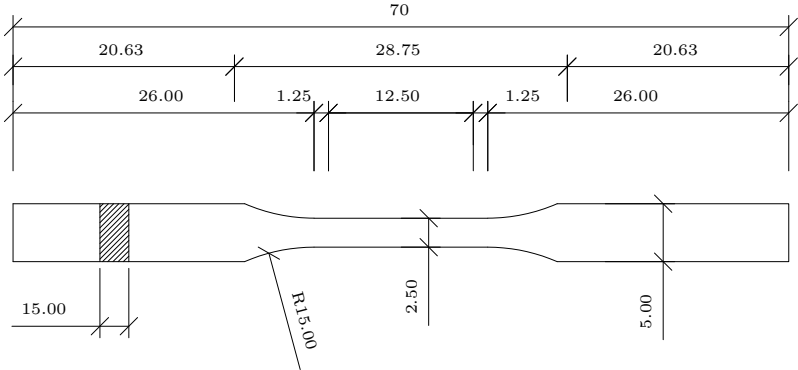
Figure 69: *Theoretical dimensions of short tensile dog-bone shaped samples*
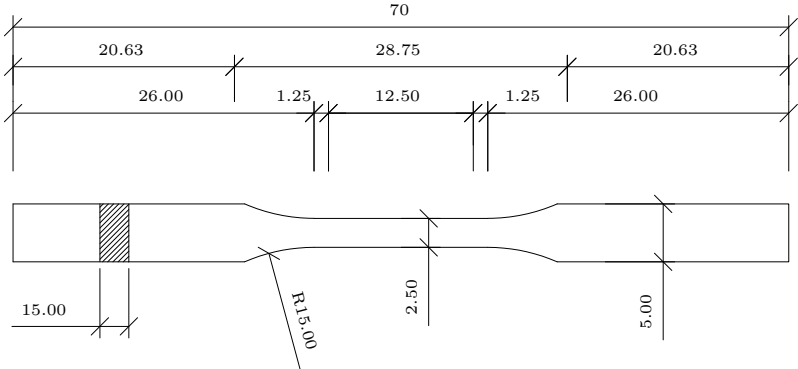
Figure 70: *Theoretical dimensions of long tensile dog-bone shaped samples*

a)   b)

Figure 71: *Tensile measurement experimental setup*
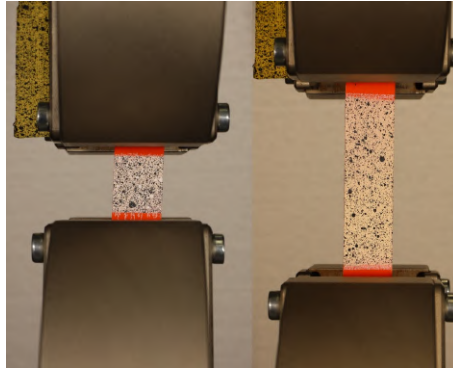
Figure 72: Samples placed in machine clamps

Sample strain was determined by virtual extensometers by using DIC analysis in the Ncorr_post program. As seen in the graph, the position of the extensometers was found based on consistent force/displacement curves. The position of the extensometers was chosen on the basis of the original observed length in relation to the standard used, i.e., 1.25 mm from the origin of the straight part of the dog-bone shaped specimen.

5.4.2   Measured data and results

The measured average modules of elasticity are:

- **T-I_S**: $1951.082 MPa \pm 91.851$
- **T-II_S**: $1864.861 MPa \pm 107.063$
- **T-III_S**: $1860.430 MPa \pm 94.147$
- **T-I_L**: $1946.995 MPa \pm 49.499$
- **T-II_L**: $1970.167 MPa \pm 42.001$
- **T-III_L**: $1988.658 MPa \pm 48.604$
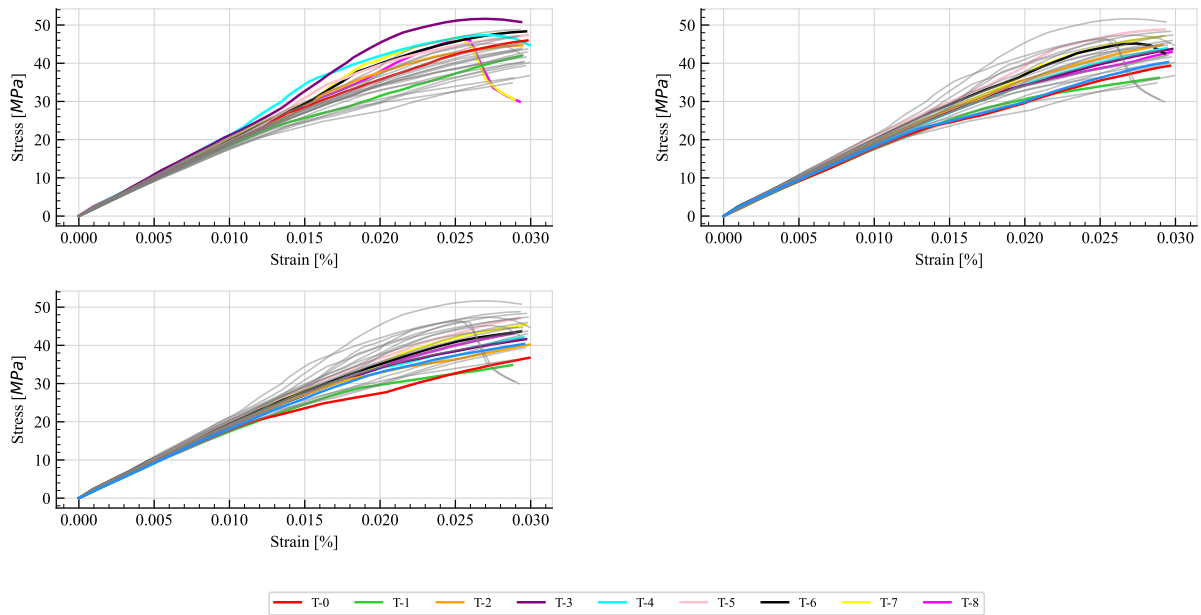
Figure 73: Strain-stress diagram of short samples: (I - top left), (II - top right), (III - bottom left)
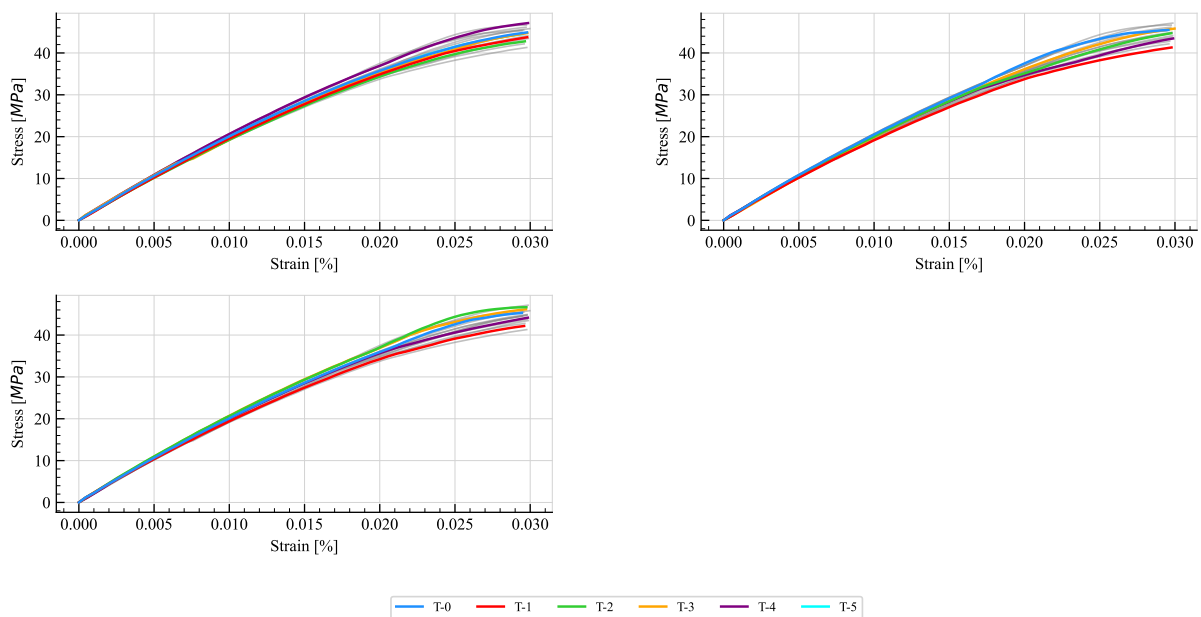
Figure 74: Strain-stress diagram of long samples: (I - top left), (II - top right), (III - bottom left)

5.5 Flexural properties

5.5.1 Description and Experimental setup

Flexural Young's modulus of elasticity was tested in a three-point bending based on Standard ČSN EN IS 178 [110]. In the interest of eliminating the influence of the filament, other colors of the same material from the same manufacturer were chosen. Concretely, white and grey colors. The theoretical flat cross-section of specimens was 2.5 ×15 mm, and the length of the specimens was 75 mm.
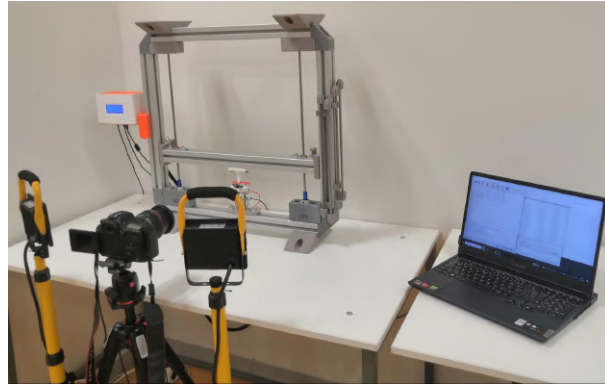
Figure 75: Flexural measurement experimental setup

Tests were performed with a limited displacement of up to 5 mm to ensure the elastic range of the specimens. Subsequently, two selected specimens with the given infill types of each color were tested with a displacement of up to 10   mm.

The static flexural modulus was calculated from the recorded data of the load diagram. This modulus was calculated from the linear part of the load diagram corresponding to elastic behaviour. The calculation of the modulus of elasticity of a three-point bending test is expressed as:

$$w = \frac{F \cdot L^3}{48 \cdot E \cdot I_y} \tag{30}$$

,where w is the displacement, F is the load, L is the span, E is the static modulus of elasticity, and I_y is the moment of inertia in the given axes. The moment of inertia was calculated from the cross-sectional dimensions of the specimens, with width expressed as b and expressed as h:

$$I_y = \frac{1}{12} \cdot b \cdot h^2 \tag{31}$$

Consequently, the static modulus of elasticity (E) was calculated using the following equation:

$$E = \frac{F \cdot L^3}{48 \cdot w \cdot I_y} \tag{32}$$
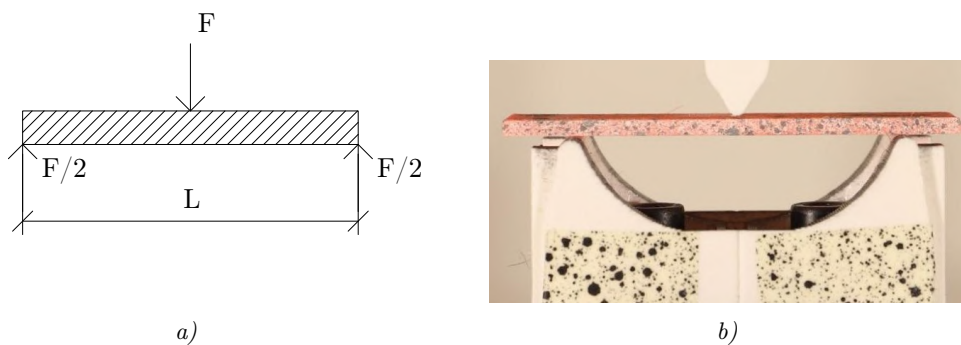
Figure 76: Static schema of experiment a), Real world representation of the experiment b)

5.5.2   Measured data and results

The measured average dimensions of the specimen flat cross-section used in the following calculations are 2.64 × 15.13 mm. The span length was set to 50 mm. The test speed was set at approximately 0.077 mm/s and photos for the following DIC analysis were taken every ten seconds. From the measured data it can be seen that the effect of filament orientation is minimal. However, it can be seen that there is a correlation between the resulting stiffness and the colour of the filament. Specifically, the white filament consistently exhibited lower stiffness compared to the orange one. The difference between the properties of the grey filament and the orange filament was minimal. This is probably due to the chemical variations caused by addition of pigments to change the natural colour of the material. The modules were calculated at chosen displacement of 2.2 mm.

The measured average modules of elasticity according to the orientation are:

- **F-I**: $1541.325 MPa \pm 83.802$
- **F-II**: $1522.297 MPa \pm 28.571$
- **F-III**: $1575.027 MPa \pm 22.909$
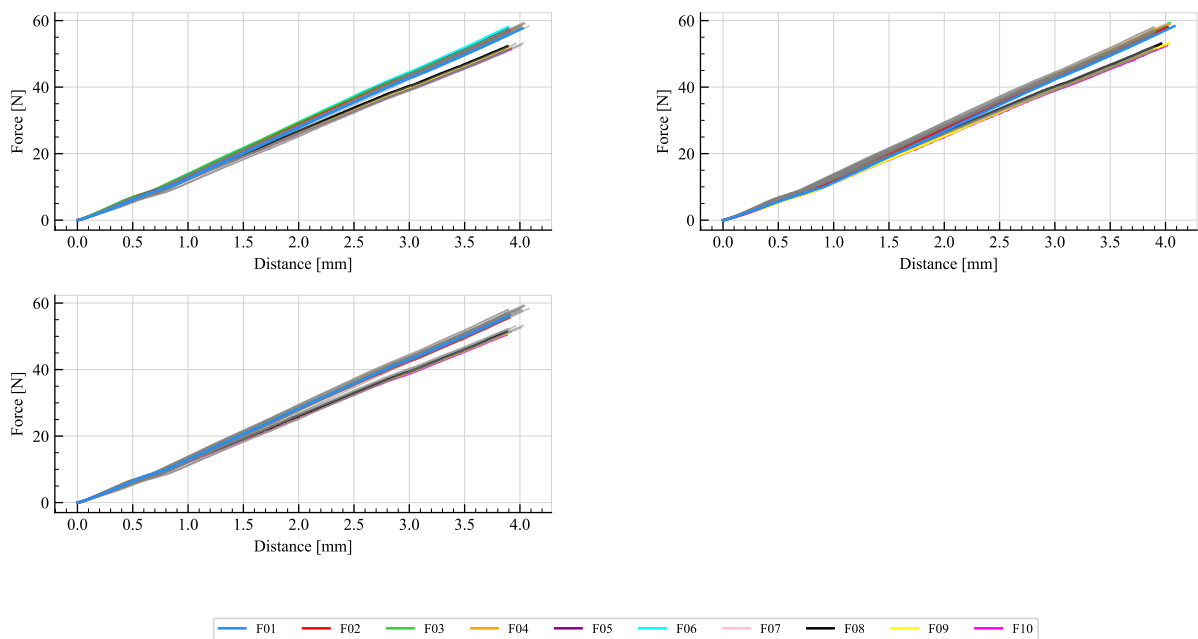
Figure 77: Load-displacement diagram: (I - top left), (II - top right), (III - bottom left)
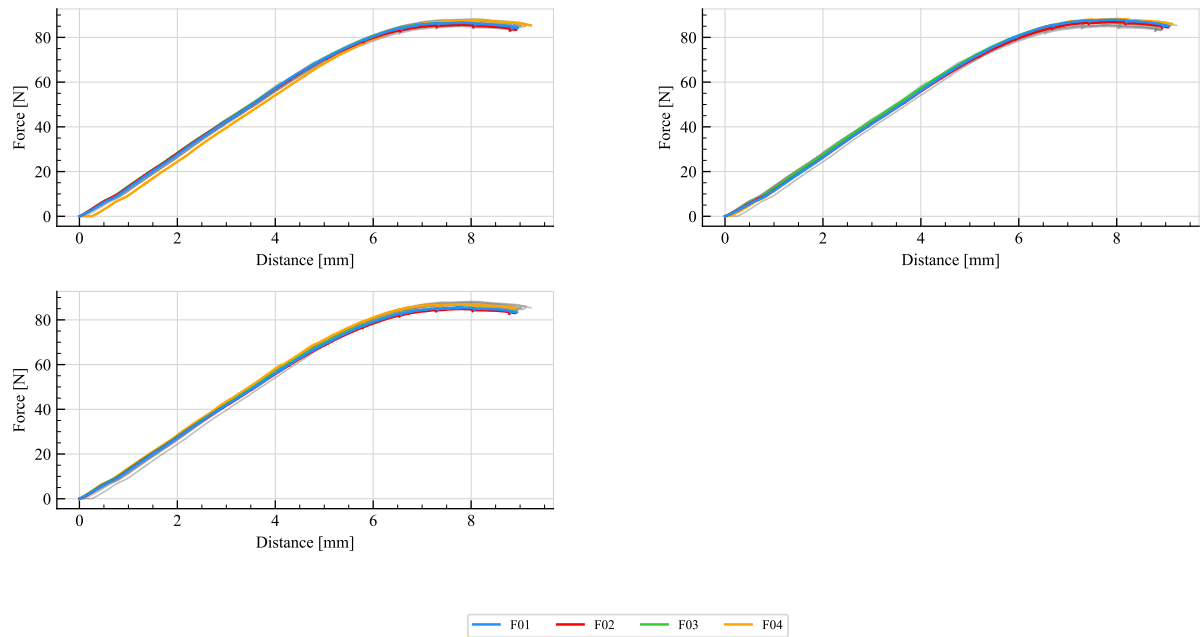
Figure 78: Load-displacement diagram: (I - top left), (II - top right), (III - bottom left)

5.6   Hexagons cells

5.6.1   Individual Cell

5.6.1.1   Description and Experimental setup

The large hexagonal cells were tested in three different orientations, with each cell being rotated by 60° from the previous orientation. This measure is taken with regard to the specific orientation of the filling, as described in the 'Experimental Description' chapter. Two series of measurements were performed on hexagons. The first series aims to investigate the influence of the orientation of type infill 1 on the mechanical properties of hexagonal specimens. The second series compared infill types 1 and 2. Additionally, the second series aimed to determine whether the discontinuities of the 2 infill in the corners have an effect on the mechanical properties of the cell.

The first series of experiments was performed using the standard 2D image analysis method, as shown in the following figure of the experimental setup. The second series also employed the standard 2D image analysis method, but with the addition of a second tracking camera. In this setup, the two cameras are independent of each other and are used to monitor different parameters. A diagram of this experiment is presented in following Figure. This system, consisting of two cameras, was designed to observe the behaviour of the corners of the hexagons in detail. One stationary camera wass tracking the hexagon as a whole, while the other camera was moving to monitor the selected area of the sample. The diagram in following figure illustrates that the first camera is controlled by the machine, while the second camera is controlled by the computer. The taking of images needed to be synchronised. These cameras were positioned opposite each other to avoid blocking each other's view. The camera holder is mounted on a moving loading

bar. The holder was designed to allow adjustment of the position and distance of the camera and the associated light source. The stochastic pattern was applied to both sides of the sample. The setup was added with a shading screen that blocked the light coming from the flashlight onto the lens of the opposite DSLR camera. Another shading screen was added to the Arducam camera lens to block light from opposite reflectors and disperse the light from the flashlight mounted next to it.
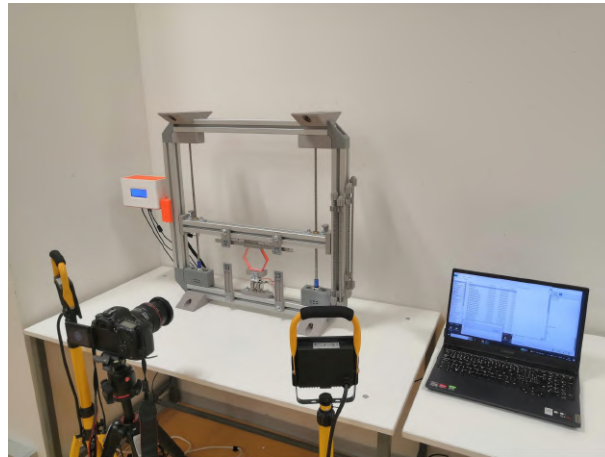
Figure 79: Individual hexagonal cell experimental setup

a)   b)
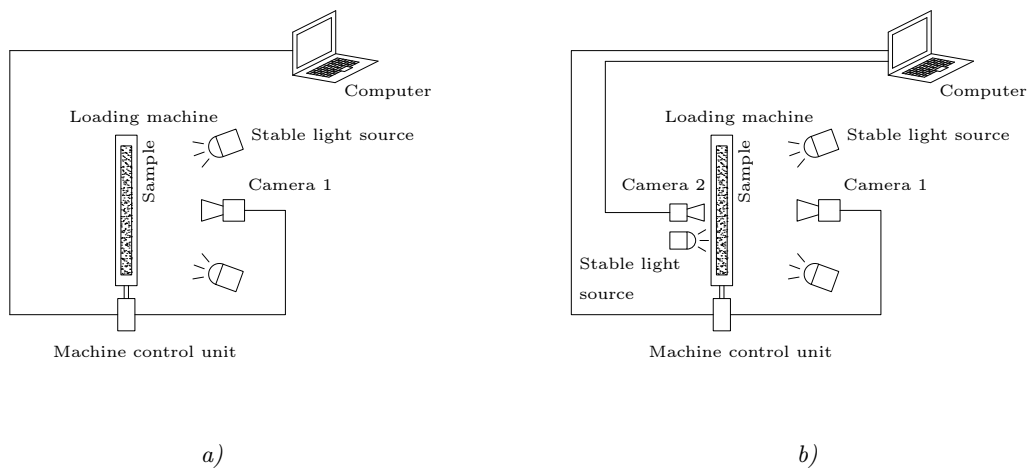
Figure 80: Individual hexagonal cell experimental setup for DIC measurement with one camera a), with two cameras for monitoring whole and detail region of testing sample b)

a)   b)   c)
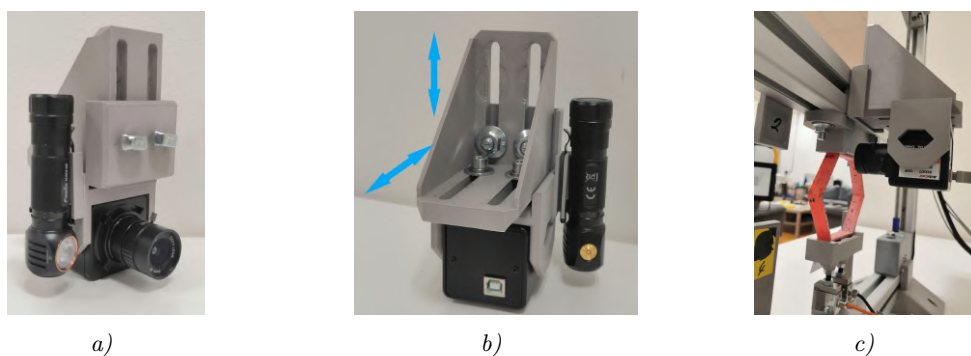
Figure 81: Adjustable holder of the camera and light source position

a)   *b)*

Figure 82: Experimental setup of monitoring detail region of sample, 1 - shading screen, 2 - light-dispersing shade
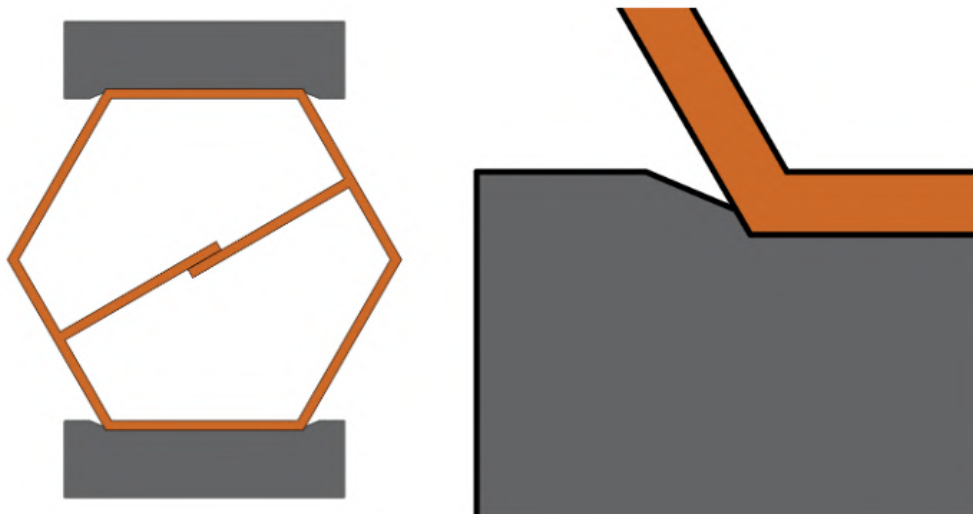
Figure 83: Designed supports of hexagonal cells to set semi-fixed joint boundary conditions

The Figure shows the designed supports that allow the corners to rotate while limiting lateral displacement (which occurs when loading cells with internal cantilevers). During compression, the corners of the hexagon that are supported experience displacement towards the centre of the hexagonal wall due to significant deformations. However, this effect was not taken into account and the supports were considered as fixed joints.

5.6.1.2   Measured data and results

The test speed was set at approximately 0.077   mm/s. Images were captured at 10-second intervals for 10 mm load displacement and 12-second intervals for 30 mm displacement.

- *Series of testing samples with a global infill pattern.*
  The results of previous experiments support the finding that the orientation of the inner infill has minimal effect on the mechanical properties.

  After placing the virtual extensometer from the left upper corner to the center of the upper hexagon wall, we got the following displacement/relative vertical displacement diagram. From the following Figure it can be seen that applied 30 mm loading displacement results

in approximately 5 mm relative vertical displacement 5 mm. This corresponded to the displacement used in the bending tests on the linear elastic part. However, the stresses were concentrated in the corners of the hexagon where plasticization has already occurred.
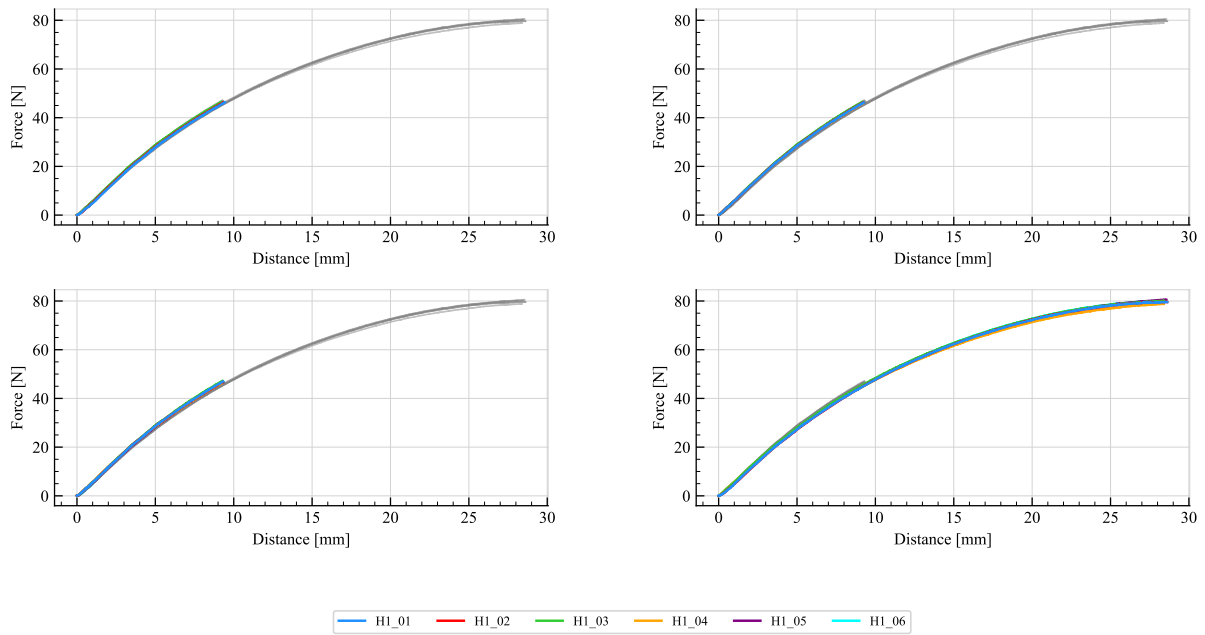
Figure 84: Load-displacement diagram of cell type A: (I - top left), (II - top right), (III - bottom left) , (Maximal displacement - bottom left)
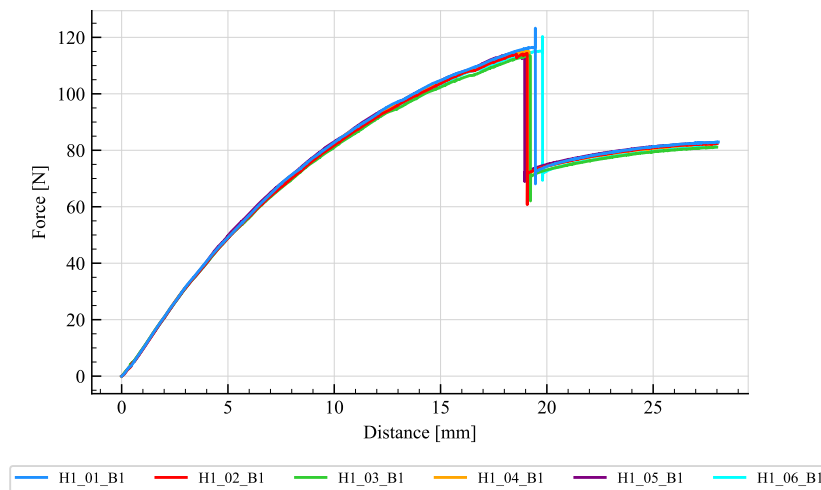
Figure 85: Load-displacement diagram of cell type B1
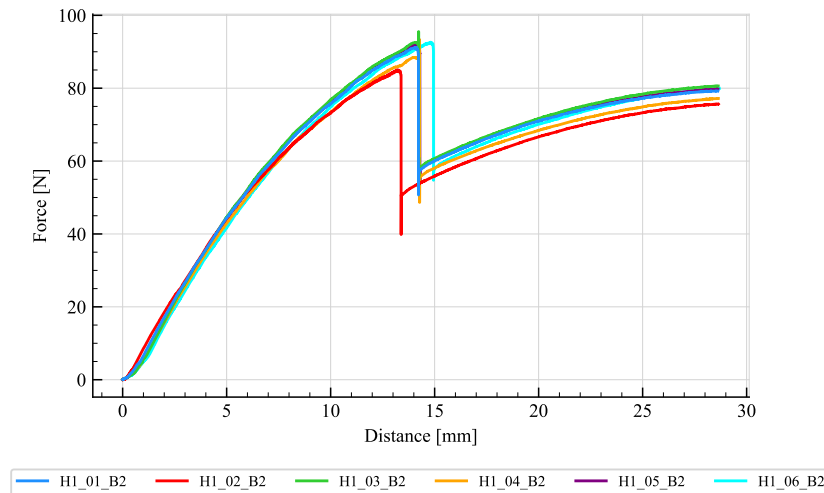
Figure 86: Load-displacement diagram of cell type B2

- *Second series of different infill patterns.*

  For the DIC analysis, a resolution of 2560 × 1400 pixels of the Arducam camera was chosen as it provides a suitable balance between resolution and quality. It offers high resolution and minimal noise.

  The processed data may not be accurate due to the position of the observed object in space caused by the changing viewing angle in time and the distortive effect caused by the optical system of the camera. The noise and camera imaging quality could also influence the measured data.

  The measured data demonstrated that the samples with infill type 2 were slightly stiffer than the ones with infill type 1. This shows that the discontinuities have minimal effect on the overall sample behaviour in early stages of testing. In the end of the measuring, it can be seen in infill type 2 greater scatter of two curves. There is a possibility that the discontinuities are taking place in this effect, but more measurements would be needed to verify this conclusion. The graph indicates that type 2 is more consistent and shows a discernible trend.
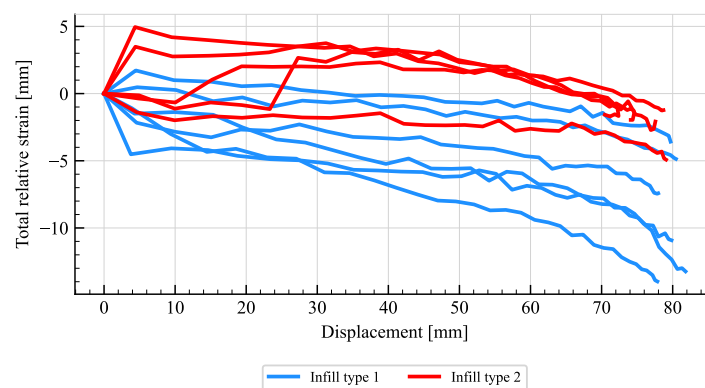
Figure 87: Displacement-relative strain diagram of virtual extensometers

5.6.2   Macrostructure

5.6.2.1   Description and Experimental setup

The potential use of the horizontal loading machine setup for microstructure testing was being considered. The main concern was to prevent any out-of-plane displacement of the structure. Pre-tests did not reveal any such issues, so the horizontal setup was not utilised. The tracking of macrostructure tracking labels was unreliable and caused many problems when used in the Ncorr program. This may have been mainly due to the applied sparse pattern on the tracking labels. The developed tracking program was used at the time and it worked without any problems.

Due to the nature of this structure, there was a tendency of left-down cells to lose contact between the support and the structure in the later stages of the test due to large deformations. At that point, it is no longer possible to consider the supports as a fixed joint. This could be resolved by redesigning the structure or resolving the corner supports as compliant joints [111]. However, it is unclear how the pliable joints would withstand the high stresses during experiments on large samples and whether they would be reusable. Additionally, this solution limits their shape and orientation versatility. Regarding the macrostructure, it is important to consider the design of the joint dimensions to prevent any alteration of the properties of the corner cells resulting from changes in the specific layout and interconnection of the layers in the 3D printing manufacturing process. It is important to consider these factors when evaluating the feasibility of this approach.

5.6.2.2   Measured data and results

The loading curves in Fig 88 show that the adhered structure is significantly less stiff than the structure made as a whole. Additionally, the snapping sequence of the internal cantilevers differed during the test. The stiffness of the adhered structure is 0.139 N/mm, while the second structure has a stiffness of 0.283 N/mm. Relative displacements of points on the structure due to time constraints were not evaluated.

a)   b)
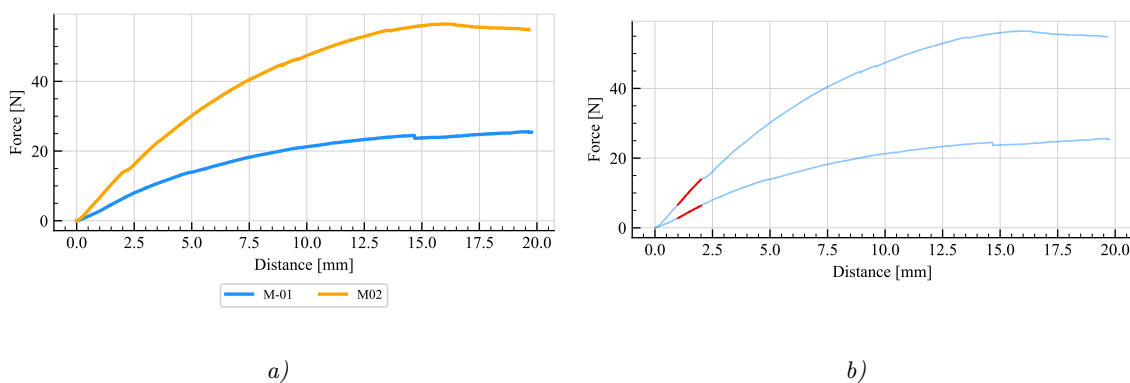
Figure 88: Load-displacement diagram of microstructured a), Load curves with marked linear evaluation region b).

5.7   Shear tests of adhesive joints

5.7.1   Description and Experimental setup

The determination of the repeatability of the adhesive joint was done by a shear test. The area that was adhered measured 10×10 mm. Adhesive was always left to cure for at least 24 hours. Sample preparation process for the reusability investigation:

- Performed test

- Manual removal of adhesive

- Chemical cleaning

- Adhering of samples

- Fixing the samples by clamp and leaving the adhesive to cure

5.7.2   Measured data and results

The graph reveals that the used adhesion is highly inconsistent, probably mainly due to differences in the amount of adhesion applied and overall preparation process of the tested sample. However, the number of reusability cycles seems to has minimal effect.
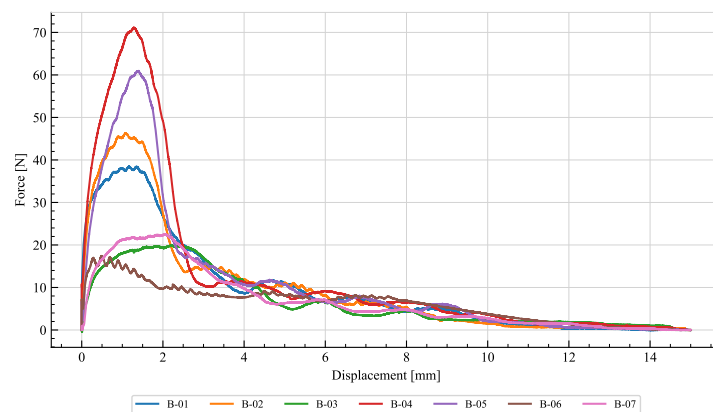
Figure 89: Load-displacement diagram of shear tests

6   Results and discussion

6.1   Friction measurements

The data were evaluated in the initial part of the sliding, where the lower and upper samples were still in contact and the relative displacement of the upper sample was limited to 65 mm. The linear part of the velocity indicates the resulting constant part of the acceleration, which was used for further calculations. The orange dashed line shows the average value of this constant part which sort of corresponds to the overall average of non-zero values shown as an orange dashed

line. The average acceleration was 2.5687 mm^2/s. This results in KCOF of 0.150 ± 0.075. The SCOF was 0.516 ± 0.118
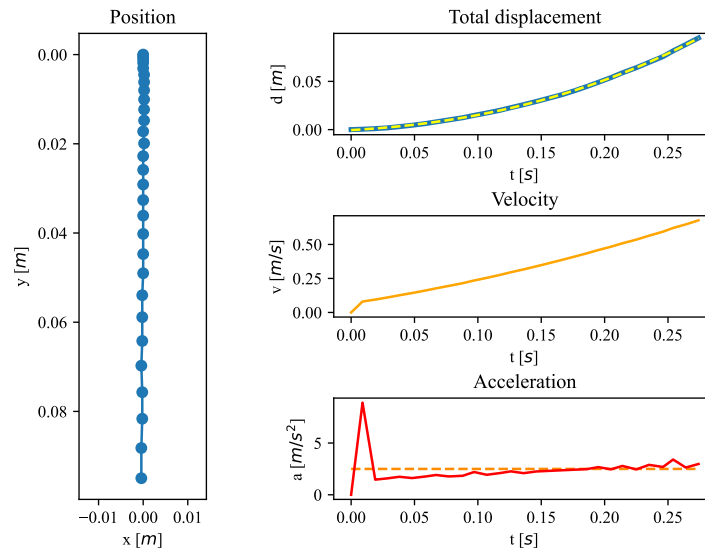
Figure 90: Evaluation of KCOF

To achieve more reliable KCOF results, the bottom sample would need to be further extended. Alternatively, the measurement can be reversed by decreasing the angle of the plane and determining the angle at which the sample stops. Another option is to abandon the inclined plane method of measuring friction and instead directly measure the contact and friction forces.

From the graph can be seen that higher roughness corresponds with higher friction coefficient.

6.2   Tensile measurements

The minimum variance of the data suggests that the orientation of the infill has no effect.
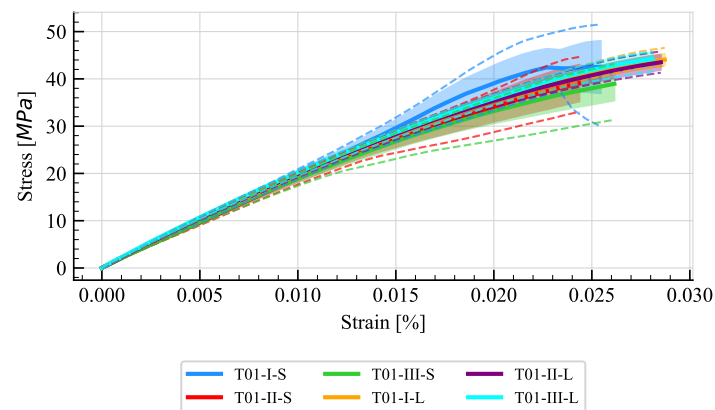
Figure 91: Strain-stress diagram of tensile test

6.3   Individual hexagon cells

The figure shows the consistency of the loading process of cells type A, which indicates good repeatability of the chosen sample manufacturing technology by 3D printing. The difference caused by the infill pattern type 1 is negligible. The scatter of individual data is minimal, indicating that 3D printing is a reliable production method.
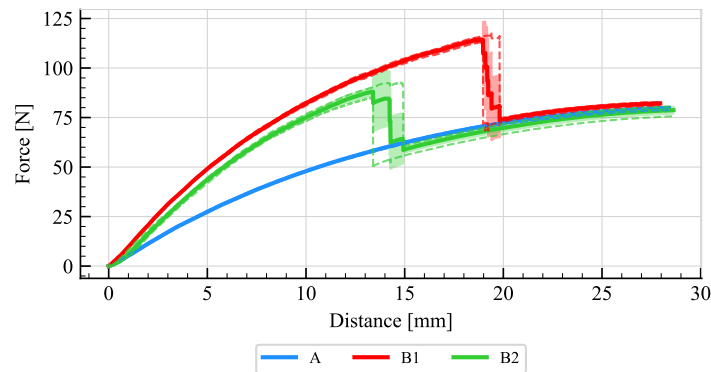
Figure 92: Displacement-relative strain diagram of virtual extensometers. The solid line is the mean, colored area is std from the mean line and dashed line is the maximum and minimum data.

Interestingly, the path of the side corners of the hexagonal specimen at the applied approximately 30 mm displacement of the loading bar corresponds to the final deformed shape. Figure Z shows that each type of infill exhibits a statistical trend. The stiffening of infill 1 at the corner exhibits greater scatter, and the extensometer points move further apart as the loading progresses. In contrast, data of infill type 2 show that the corner stiffening reduces the relative displacement of these points and the virtual extensometer curve fluctuates around 0.
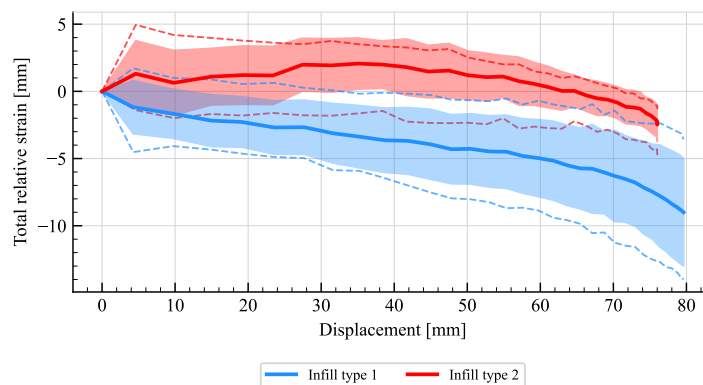
Figure 93: Displacement-relative strain diagram of virtual extensometers. The solid line is the mean, colored area is std from the mean line and dashed line is the maximum and minimum data.

6.4   Shear tests

The scatter of the data is so large that the type of glue used is not suitable.

6.5   Macrostructure

The average ratio of the loading curves is 2.22509. This suggests that the adhesive used may not achieve perfect bonding and interaction between neighbouring bonded cells.

7   Conclusions

The conclusion of this thesis shows the progress made in the experimental investigation of the mechanical behaviour of 3D printed modular metamaterials composed of hexagonal cells. The work focused on the formation and analysis of macrostructures composed of individual cells with variable internal supports, which is a fundamental step towards achieving the desired properties. Valuable material characteristics and data were obtained in the experiments, which serve as input for mathematical simulations. The development and implementation of a multi-camera measurement system was also an important element to monitor the cell parameters during testing.

The objectives of this thesis have been thoroughly evaluated on the basis of the results and experimental data obtained. It should be noted that 3D printed products are not entirely homogeneous and are anisotropic due to the production process and infill pattern used. To increase homogeneity, alternative sample production methods could be considered, such as using resin or silicone casting. The modification of an existing 3D printer with a new print head allows for new production possibilities that can be further exploited in the future research agendas.

One of the objectives was to determine whether one selected type of infill retains its properties regardless of the relative orientation with respect to the axes of the wall specimens. The measured flexural and tensile data showed that the orientation of the filler has only a slight effect on its mechanical properties in the elastic region. However, the data of individual large hexagonal cells indicates that this effect on overall properties of the sample is negligible.

The work also aimed to determine if using multiple independent type 2 infills that are not directly connected would reduce specimen stiffness due to discontinuities in large hexagonal cells. The hypothesis that the specimens would be less stiff due to discontinuity in the corner sections was disproved, indicating that the connection of the individual infills in the corner sections is sufficient.

The third objective was to determine if pre-snapped cells exhibit higher stiffness. The investigation revealed that the initial stiffness of the pre-snapped cell specimens was much higher.

Additionally, an investigation was conducted to determine whether the macrostructure, consisting of attached individual cells, would exhibit similar properties to the structure fabricated as a whole. Potentially to determine what the effect of bonding would be. The stability of the adhesion affected the stiffness of the macrostructure, which was approximately 50% lower than that of the macrostructure fabricated as a whole.

Further tests were performed to verify whether the adhesive bonds could be repeated. Although

the adhesive showed no decrease in strength after repeated use, the shear tests revealed a certain degree of inconsistency in this type of joints. It is suspected that the adhesive used may not be suitable for this application.

The method of using multiple cameras has proven to be useful. The results indicate that this approach is effective and may lead to the use of multiple cameras or other measurement devices in the future. However, it is important to note that these observations may be influenced by inaccuracies of the used camera. The results can be improved in the future by using more suitable cameras with higher resolution, higher quality lenses, speed cameras or even multiple cameras to track deformations in three dimensions and possible out-of-plane deviations. More cameras will also ensure that the perspective distortion is eliminated. The developed program satisfies all the required aspects and has demonstrated high efficiency in processing results. The program can easily be extended in the future to include the strain calculations. However, it is necessary to keep in mind the method of calculation and any potential errors. Supplementing the program with standard DIC mechanisms, combined with image masking and limiting search areas based on existing mechanisms, would be admissible.

This work has expanded our understanding of the behaviour of complex structures and suggested an efficient way to collect data for future research. The results of these experiments provide a valuable resource for further development and optimization of 3D printed modular metamaterials. These structures have the potential to change the approach of the design and creation of metamaterial structures in various industries, including engineering, construction, and others.

8   References

References

[1]   KUMAR, Rakesh; KUMAR, Manoj; CHOHAN, Jasgurpreet Singh; KUMAR, Santosh. Overview on Metamaterial: History, Types and Applications. *Materials Today: Proceedings* [online]. 2022, vol. 56, pp. 3016–3024 [visited on 2024-01-08]. ISSN 2214-7853. Available from DOI: `10.1016/j.matpr.2021.11.423`.

[2]   KAIYU, Jiang; JIAN, Wang; MINJIE, Wang; CHUNZHENG, Duan; BINZHOU, Chi. Forming and Machining Technology for Metamaterials. In: *2022 IEEE MTT-S International Microwave Workshop Series on Advanced Materials and Processes for RF and THz Applications (IMWS-AMP)* [online]. Guangzhou, China: IEEE, 2022, pp. 1–3 [visited on 2023-12-17]. ISBN 978-1-66547-834-2. Available from DOI: `10.1109/IMWS-AMP54652.2022.10106840`.

[3]   ENGHETA, Nader; ZIOLKOWSKI, Richard W. (eds.). *Metamaterials: Physics and Engineering Explorations* [online]. 1st ed. Wiley, 2006 [visited on 2023-12-17]. ISBN 978-0-471-76102-0 978-0-471-78419-7. Available from DOI: `10.1002/0471784192`.

[4]   FAN, Junxiang; ZHANG, Lei; WEI, Shuaishuai; ZHANG, Zhi; CHOI, Seung-Kyum; SONG, Bo; SHI, Yusheng. A Review of Additive Manufacturing of Metamaterials and Developing Trends. *Materials Today* [online]. 2021, vol. 50, pp. 303–328 [visited on 2023-12-17]. ISSN 13697021. Available from DOI: `10.1016/j.mattod.2021.04.019`.

[5]   GRIMBERG, Raimond. Electromagnetic Metamaterials. *Materials Science and Engineering: B* [online]. 2013, vol. 178, no. 19, pp. 1285–1295 [visited on 2023-12-27]. ISSN 09215107. Available from DOI: `10.1016/j.mseb.2013.03.022`.

[6]   WANG, Jun; DAI, Gaole; HUANG, Jiping. Thermal Metamaterial: Fundamental, Application, and Outlook. *iScience* [online]. 2020, vol. 23, no. 10, p. 101637 [visited on 2023-12-27]. ISSN 25890042. Available from DOI: `10.1016/j.isci.2020.101637`.

[7]   HU, Run; XI, Wang; LIU, Yida; TANG, Kechao; SONG, Jinlin; LUO, Xiaobing; WU, Junqiao; QIU, Cheng-Wei. Thermal Camouflaging Metamaterials. *Materials Today* [online]. 2021, vol. 45, pp. 120–141 [visited on 2023-12-27]. ISSN 13697021. Available from DOI: `10.1016/j.mattod.2020.11.013`.

[8]   GRIC, Tatjana; HESS, Ortwin. Metamaterial Cloaking. In: *Phenomena of Optical Metamaterials* [online]. Elsevier, 2019, pp. 175–186 [visited on 2023-12-17]. ISBN 978-0-12-813896-0. Available from DOI: `10.1016/B978-0-12-813896-0.00007-9`.

[9]   CAI, Wenshan; SHALAEV, Vladimir. *Optical Metamaterials* [online]. New York, NY: Springer New York, 2010 [visited on 2023-12-27]. ISBN 978-1-4419-1150-6 978-1-4419-1151-3. Available from DOI: `10.1007/978-1-4419-1151-3`.

[10] CHEN, Yixin; AI, Bin; WONG, Zi Jing. Soft Optical Metamaterials. *Nano Convergence* [online]. 2020, vol. 7, no. 1, p. 18 [visited on 2023-12-27]. ISSN 2196-5404. Available from DOI: `10.1186/s40580-020-00226-7`.

[11] JENETT, Benjamin; CAMERON, Christopher; TOURLOMOUSIS, Filippos; RUBIO, Alfonso Parra; OCHALEK, Megan; GERSHENFELD, Neil. Discretely Assembled Mechanical Metamaterials. *Science Advances* [online]. 2020, vol. 6, no. 47, eabc9943 [visited on 2023-12-18]. ISSN 2375-2548. Available from DOI: `10.1126/sciadv.abc9943`.

[12] YANG, Nan; CHEN, Chun-Wei; YANG, Jinkyu; SILVERBERG, Jesse L. Emergent Reconfigurable Mechanical Metamaterial Tessellations with an Exponentially Large Number of Discrete Configurations. *Materials & Design* [online]. 2020, vol. 196, p. 109143 [visited on 2023-12-18]. ISSN 02641275. Available from DOI: `10.1016/j.matdes.2020.109143`.

[13] FOK, Lee; AMBATI, Muralidhar; ZHANG, Xiang. Acoustic Metamaterials. *MRS Bulletin* [online]. 2008, vol. 33, no. 10, pp. 931–934 [visited on 2023-12-27]. ISSN 0883-7694, ISSN 1938-1425. Available from DOI: `10.1557/mrs2008.202`.

[14] HABERMAN, Michael R.; GUILD, Matthew D. Acoustic Metamaterials. *Physics Today* [online]. 2016, vol. 69, no. 6, pp. 42–48 [visited on 2023-12-27]. ISSN 0031-9228, ISSN 1945-0699. Available from DOI: `10.1063/PT.3.3198`.

[15] BARHEMAT, Rojyar; MAHJOUBI, Soroush; LI, Victor C.; BAO, Yi. Lego-Inspired Reconfigurable Modular Blocks for Automated Construction of Engineering Structures. *Automation in Construction* [online]. 2022, vol. 139, p. 104323 [visited on 2023-12-18]. ISSN 09265805. Available from DOI: `10.1016/j.autcon.2022.104323`.

[16] YU, Bo; YIN, Lesiqi; WANG, Peng; GONG, Cheng. Terahertz Reconfigurable Multi-Functional Metamaterials Based on 3D Printed Mortise-Tenon Structures. *Virtual and Physical Prototyping* [online]. 2023, vol. 18, no. 1, e2230468 [visited on 2023-12-27]. ISSN 1745-2759, ISSN 1745-2767. Available from DOI: `10.1080/17452759.2023.2230468`.

[17] SAUNDERS, Robert. *Metamaterials Using Additive Manufacturing Technologies* [online]. 2020-06-29. [visited on 2023-12-17]. Available from: `https://apps.dtic.mil/sti/citations/AD1103255`.

[18] ASKARI, Meisam; HUTCHINS, David A.; THOMAS, Peter J.; ASTOLFI, Lorenzo; WATSON, Richard L.; ABDI, Meisam; RICCI, Marco; LAURETI, Stefano; NIE, Luzhen; FREEAR, Steven; WILDMAN, Ricky; TUCK, Christopher; CLARKE, Matt; WOODS, Emma; CLARE, Adam T. Additive Manufacturing of Metamaterials: A Review. *Additive Manufacturing* [online]. 2020, vol. 36, p. 101562 [visited on 2023-12-17]. ISSN 22148604. Available from DOI: `10.1016/j.addma.2020.101562`.

[19] LOSHAKOV, P. Modular Structures as a Method of Architectural Environment Arrangement. *Construction Materials and Products* [online]. 2022, pp. 38–53 [visited on 2023-12-18]. ISSN 2618-7183. Available from DOI: `10.34031/2618-7183-2022-5-1-38-53`.

[20] LEONG, Zee; CHEN, Rongsheng; XU, Zijie; LIN, Yangsheng; HU, Nan. Robotic Arm Three-Dimensional Printing and Modular Construction of a Meter-Scale Lattice Façade Structure. *Engineering Structures* [online]. 2023, vol. 290, p. 116368 [visited on 2023-12-18]. ISSN 01410296. Available from DOI: `10.1016/j.engstruct.2023.116368`.

[21] LEE, Seungwoo; KANG, Byungsoo; KEUM, Hohyun; AHMED, Numair; ROGERS, John A.; FERREIRA, Placid M.; KIM, Seok; MIN, Bumki. Heterogeneously Assembled Metamaterials and Metadevices via 3D Modular Transfer Printing. *Scientific Reports* [online]. 2016, vol. 6, no. 1, p. 27621 [visited on 2023-12-27]. ISSN 2045-2322. Available from DOI: `10.1038/srep27621`.

[22] PAL, Raj Kumar; VILA, Javier; RUZZENE, Massimo. Topologically Protected Edge States in Mechanical Metamaterials. In: *Advances in Applied Mechanics* [online]. Elsevier, 2019, vol. 52, pp. 147–181 [visited on 2023-12-18]. ISBN 978-0-12-817479-1. Available from DOI: `10.1016/bs.aams.2019.04.001`.

[23] YUAN, Xujin; CHEN, Mingji; YAO, Yin; GUO, Xiaogang; HUANG, Yixing; PENG, Zhilong; XU, Baosheng; LV, Bowen; TAO, Ran; DUAN, Shenyu; LIAO, Haitao; YAO, Kai; LI, Ying; LEI, Hongshuai; CHEN, Xu; HONG, Guangfu; FANG, Daining. Recent Progress in the Design and Fabrication of Multifunctional Structures Based on Metamaterials. *Current Opinion in Solid State and Materials Science* [online]. 2021, vol. 25, no. 1, p. 100883 [visited on 2023-12-27]. ISSN 13590286. Available from DOI: `10.1016/j.cossms.2020.100883`.

[24] RAFSANJANI, Ahmad; AKBARZADEH, Abdolhamid; PASINI, Damiano. Snapping Mechanical Metamaterials under Tension. *Advanced Materials* [online]. 2015, vol. 27, no. 39, pp. 5931–5935 [visited on 2023-12-27]. ISSN 0935-9648, ISSN 1521-4095. Available from DOI: `10.1002/adma.201502809`.

[25] CUI, Zhiming; JU, Jaehyung. Topologically Reconfigurable Mechanical Metamaterials with Motion Structures. *Mechanics of Materials* [online]. 2020, vol. 143, p. 103317 [visited on 2023-12-27]. ISSN 01676636. Available from DOI: `10.1016/j.mechmat.2020.103317`.

[26] ZHANG, Qian; WANG, Xinyu; CAI, Jianguo; FENG, Jian. Motion Paths and Mechanical Behavior of Origami-Inspired Tunable Structures. *Materials Today Communications* [online]. 2021, vol. 26, p. 101872 [visited on 2023-12-27]. ISSN 23524928. Available from DOI: `10.1016/j.mtcomm.2020.101872`.

[27] KHAS, Raj Agarwal; SHARMA, Shrutika; GUPTA, Vishal; SINGH, Jaskaran; SINGH, Kanwaljit. Additive Manufacturing: Materials, Technologies, and Applications. In: *Additive Manufacturing*. CRC Press, 2023. ISBN 978-1-00-325839-1.

[28] PRUSA, Gwendolin; BAUER, Leandra; SANTOS, Inês; THORWÄCHTER, Christoph; WOICZINSKI, Matthias; KISTLER, Manuel. Strain Evaluation of Axially Loaded Collateral Ligaments: A Comparison of Digital Image Correlation and Strain Gauges. *BioMedical Engineering OnLine* [online]. 2023, vol. 22, no. 1, p. 13 [visited on 2023-12-29]. ISSN 1475-925X. Available from DOI: `10.1186/s12938-023-01077-z`.

[29] XOMETRY, Team. *3D Printing vs. Traditional Manufacturing: Differences and Comparison* [online]. 2022-08-30. [visited on 2024-01-08]. Available from: `https://www.xometry.com/resources/3d-printing/3d-printing-vs-traditional-manufacturing/`.

[30]   BORG COSTANZI, Christopher. Additive Manufacturing. In: BORG COSTANZI, Christopher (ed.). *Reinforcing and Detailing of Thin Sheet Metal Using Wire Arc Additive Manufacturing as an Application in Facades* [online]. Wiesbaden: Springer Fachmedien, 2023, pp. 47–59 [visited on 2023-12-28]. Mechanik, Werkstoffe Und Konstruktion Im Bauwesen. ISBN 978-3-658-41540-2. Available from DOI: `10.1007/978-3-658-41540-2_3`.

[31]   MOLLA-HOSSEINI, Mojtaba; HOSSEINI, Marjan; VOSSOUGHI, Gholamreza; SHARIFZADEH, Mahdi. Additive Manufacturing: A Game-Changing Paradigm in Manufacturing and Supply Chains. In: SHARIFZADEH, Mahdi (ed.). *Industry 4.0 Vision for Energy and Materials* [online]. 1st ed. Wiley, 2022, pp. 339–358 [visited on 2023-12-28]. ISBN 978-1-119-69593-6 978-1-119-69586-8. Available from DOI: `10.1002/9781119695868.ch13`.

[32]   BOURELL, David L.; WOHLERS, Terry. Introduction to Additive Manufacturing. In: BOURELL, David L.; FRAZIER, William; KUHN, Howard; SEIFI, Mohsen (eds.). *Additive Manufacturing Processes* [online]. ASM International, 2020, pp. 3–10 [visited on 2023-12-28]. ISBN 978-1-62708-290-7. Available from DOI: `10.31399/asm.hb.v24.a0006555`.

[33]   SERRANO, Dolores R.; KARA, Aytug; YUSTE, Iván; LUCIANO, Francis C.; ONGOREN, Baris; ANAYA, Brayan J.; MOLINA, Gracia; DIEZ, Laura; RAMIREZ, Bianca I.; RAMIREZ, Irving O.; SÁNCHEZ-GUIRALES, Sergio A.; FERNÁNDEZ-GARCÍA, Raquel; BAUTISTA, Liliana; RUIZ, Helga K.; LALATSA, Aikaterini. 3D Printing Technologies in Personalized Medicine, Nanomedicines, and Biopharmaceuticals. *Pharmaceutics* [online]. 2023, vol. 15, no. 2, p. 313 [visited on 2023-12-28]. ISSN 1999-4923. Available from DOI: `10.3390/pharmaceutics15020313`.

[34]   RASTOGI, Ayush; VISHWAKARMA, Aryman; SINGH, Nitin; KUMAR, Amrish; SINHA ROY, Indroneil. 3D Printer. *International Journal For Multidisciplinary Research* [online]. 2023, vol. 5, no. 3, p. 3112 [visited on 2023-12-28]. ISSN 2582-2160. Available from DOI: `10.36948/ijfmr.2023.v05i03.3112`.

[35]   SNIKHOVSKA, Kseniia. *Seven Types of 3D Printers - Different Printing and Extruder Technologies* [online]. 2022-10-10. [visited on 2023-12-28]. Available from: `https://penandplastic.com/3d-printer-types/`.

[36]   TEAM, Aniwaa. *Categories of 3D Printing Technologies* [online]. Aniwaa, 2023-11-24. [visited on 2023-12-28]. Available from: `https://www.aniwaa.com/guide/3d-printers/3d-printing-technologies/`.

[37]   STŘELECKÝ, Ondřej; PRŮŠA, Josef; BACH, Martin. *Basics of 3D Printing with Josef Prusa*. 1st ed. Prague: Prusa Research a.s., 2019. Available also from: `https://www.prusa3d.com/page/basics-of-3d-printing-with-josef-prusa_490/`.

[38]   *FFF vs FDM: 3d Printing, Extrusion, 3d Printer* [online]. Digital Manufacturing Store Top 3D Shop, 2020-08-27. [visited on 2023-12-28]. Available from: `https://top3dshop.com/blog/fff-vs-fdm-difference-and-best-printers`.

[39] ZHANG, Hong; FANG, Min; YU, Yongming; LIU, Qiannan; HU, Xiaojia; ZHANG, Liang; HU, Honghai; ZHANG, Chunjiang; HUANG, Feng; TIAN, Fang; ZHANG, Nana; DAI, Xiaofeng. Application Prospect of 3D Printing Technology in the Food Intelligent Manufacturing. In: DENG, Kevin; YU, Zhengtao; PATNAIK, Srikanta; WANG, John (eds.). *Recent Developments in Mechatronics and Intelligent Robotics*. Cham: Springer International Publishing, 2019, pp. 974–984. Advances in Intelligent Systems and Computing. ISBN 978-3-030-00214-5. Available from DOI: 10.1007/978-3-030-00214-5_120.

[40] BRIJESH, Gurav. *CoreXY 3D Printer: All You Need to Know* [online]. All3DP, 2023-07-01. [visited on 2024-01-07]. Available from: https://all3dp.com/2/corexy-3d-printer-is-it-worth-buying/.

[41] O'CONNELL, Jackson. *SCARA 3D Printer: All You Need to Know* [online]. All3DP, 2021-05-17. [visited on 2024-01-07]. Available from: https://all3dp.com/2/scara-3d-printer-guide/.

[42] KAUPPILA, Ile. *Robotic Arm 3D Printing – The Ultimate Guide* [online]. All3DP Pro, 2023-05-22. [visited on 2024-01-07]. Available from: https://all3dp.com/1/robotic-arm-3d-printing-platforms-software/.

[43] KAUPPILA, Ile. *3D Concrete Printing – The Ultimate Guide* [online]. All3DP Pro, 2023-08-16. [visited on 2024-01-07]. Available from: https://all3dp.com/1/3d-concrete-printing-guide/.

[44] *3D-printing Robot Creates Freestanding Metal Structures* [online]. New Atlas, 2014-02-22. [visited on 2024-01-07]. Available from: https://newatlas.com/3d-metal-printing-robot/30938/.

[45] GAUGHRAN, Bill. THE GRAPHICS CODE, VISUALIZATION AND CAD: A STRATEGY FOR MORE EFFICIENT USE OF CAD PROGRAMS. In: *Proceeding of Flexible Automation and Integrated Manufacturing 1996* [online]. Atlanta, Georgia, USA: Begellhouse, 2023, pp. 373–381 [visited on 2023-12-27]. ISBN 978-1-56700-067-2. Available from DOI: 10.1615/FAIM1996.400.

[46] GLEADALL, Andrew. FullControl GCode Designer: Open-source Software for Unconstrained Design in Additive Manufacturing. *Additive Manufacturing* [online]. 2021, vol. 46, p. 102109 [visited on 2023-12-27]. ISSN 22148604. Available from DOI: 10.1016/j.addma.2021.102109.

[47] NEGI, Pawan; YADAV, Om Prakash; RAM, Mangey. *Basics of CNC Programming* [online]. 1st ed. New York: River Publishers, 2022 [visited on 2023-12-27]. ISBN 978-1-00-333731-7. Available from DOI: 10.1201/9781003337317.

[48] Hexagonal Tiling. In: *Wikipedia* [online]. 2023 [visited on 2023-12-03]. Available from: https://en.wikipedia.org/w/index.php?title=Hexagonal_tiling&oldid=1186926297.

[49] *Prusament PETG Prusa Orange 1kg | Original Prusa 3D Printers Directly from Josef Prusa* [online]. Prusa3D by Josef Prusa. [visited on 2023-12-28]. Available from: https://www.prusa3d.com/product/prusament-petg-prusa-orange-1kg/#downloads.

[50] *E3D Revo™ Hemera XS* [online]. E3D. [visited on 2023-12-27]. Available from: `https://e3d-online.com/products/revo-hemera-xs`.

[51] *E3D Revo™ Nozzles* [online]. E3D. [visited on 2023-12-28]. Available from: `https://e3d-online.com/products/revo-nozzles`.

[52] MD. SABIT SHAHRIAR HAQUE. Minimizing Stringing Issues In FDM Printing [online]. 2020 [visited on 2023-12-27]. Available from DOI: `10.13140/RG.2.2.35536.74247`.

[53] *Univerzální kontaktní lepidlo Pattex Chemoprén* [online]. Pattex. [visited on 2023-12-27]. Available from: `https://www.pattex.cz/cs/produkty/kontaktni-lepidla/contact-liquid.html`.

[54] *Technický benzín* [online]. SEVEROCHEMA. [visited on 2023-12-27]. Available from: `https://www.severochema.cz/produkty/redidla-a-technicke-kapaliny-c7/technicky-benzin-p150/`.

[55] *Chemical Resistance Chart | Plastics International* [online]. Plastics International. [visited on 2023-12-27]. Available from: `https://www.plasticsintl.com/chemical-resistance-chart`.

[56] LOST IN TECH (director). *Why Your 3d Printed Stuff Doesn't Fit Together and How to Fix It!* [online]. 2023. [visited on 2023-12-09]. Available from: `https://www.youtube.com/watch?v=yzPqBt2SrcE`.

[57] GDOUTOS, Emmanuel E. Digital Image Correlation (DIC). In: GDOUTOS, Emmanuel E. *Experimental Mechanics* [online]. Cham: Springer International Publishing, 2022, vol. 269, pp. 251–259 [visited on 2023-12-29]. ISBN 978-3-030-89465-8 978-3-030-89466-5. Available from DOI: `10.1007/978-3-030-89466-5_12`.

[58] DEEPAK, A.; JENKINS, D. F. L. Comparison of Digital Image Correlation (DIC) Technique with Nanomaterial-Based Sensor for the Analysis of Strain Measurements. *International Journal of Nanoscience* [online]. 2021, vol. 20, no. 04, p. 2150032 [visited on 2023-12-29]. ISSN 0219-581X, ISSN 1793-5350. Available from DOI: `10.1142/S0219581X21500320`.

[59] JADHAV, Prakash; YELLA, Gruhalakshmi; AZMEERA, Anitha. Ply Level Strain Measurement in Composites Using Digital Image Correlation. *Materials Today: Proceedings* [online]. 2023, S2214785323008891 [visited on 2023-12-29]. ISSN 22147853. Available from DOI: `10.1016/j.matpr.2023.02.325`.

[60] LIM, Chhoung; JEONG, Yeongseok; LIMKANTANYU, Suchart; KWON, Minho. Strain Measuring of Composite Grid Using Digital Image Correlation. *Advances in Materials Science and Engineering* [online]. 2022, vol. 2022, pp. 1–12 [visited on 2023-12-29]. ISSN 1687-8442, ISSN 1687-8434. Available from DOI: `10.1155/2022/6041887`.

[61] CHEN, Terry Yuan-Fang; DANG, Nhat Minh; WANG, Zhao-Ying; CHANG, Liang-Wei; KU, Wei-Yu; LO, Yu-Lung; LIN, Ming-Tzer. Use of Digital Image Correlation Method to Measure Bio-Tissue Deformation. *Coatings* [online]. 2021, vol. 11, no. 8, p. 924 [visited on 2023-12-29]. ISSN 2079-6412. Available from DOI: `10.3390/coatings11080924`.

[62] ALCI, Muhsin; GUNES, Recep. A Comparison Study on Experimental Characterization of Unidirectional Fiber Reinforced Composites Using Strain-Gauges and Virtual Extensometers. *Materials Testing* [online]. 2023, vol. 65, no. 2, pp. 174–191 [visited on 2023-12-29]. ISSN 0025-5300, ISSN 2195-8572. Available from DOI: 10.1515/mt-2022-0274.

[63] SOLAV, Dana; SILVERSTEIN, Asaf. DuoDIC: 3D Digital Image Correlation in MATLAB. *Journal of Open Source Software* [online]. 2022, vol. 7, no. 74, p. 4279 [visited on 2023-12-29]. ISSN 2475-9066. Available from DOI: 10.21105/joss.04279.

[64] ZHOU, Lei; WEI, Weiyufeng. DIC: Deep Image Clustering for Unsupervised Image Segmentation. *IEEE Access* [online]. 2020, vol. 8, pp. 34481–34491 [visited on 2023-12-29]. ISSN 2169-3536. Available from DOI: 10.1109/ACCESS.2020.2974496.

[65] SU, Yong; ZHANG, Qingchuan. Random Errors in DIC Caused by Non-Uniform Image Noise. In: HAN, Sen; TAN, JiuBin (eds.) [online]. Beijing, China, 2016, p. 1015503 [visited on 2023-12-29]. Available from DOI: 10.1117/12.2243571.

[66] CHIEN, Chi-Hui; SU, Ting-Hsuan; HUANG, Chao-Jian; CHAO, Yuh-Jin; YEH, Wei-Li; LAM, Poh-Sang. Application of Digital Image Correlation (DIC) to Sloshing Liquids. *Optics and Lasers in Engineering* [online]. 2019, vol. 115, pp. 42–52 [visited on 2023-12-29]. ISSN 01438166. Available from DOI: 10.1016/j.optlaseng.2018.11.016.

[67] FELIPE-SESÉ, Luis; ANDRÉS-CASTRO, Francisca; MOLINA-VIEDMA, Ángel; LÓPEZ-ALBA, Elías; DÍAZ-GARRIDO, Francisco. Digital Image Correlation Employing Thermal Marking. In: *ICEM 2022* [online]. MDPI, 2022, p. 3 [visited on 2023-12-29]. Available from DOI: 10.3390/psf2022004003.

[68] SJÖDAHL, Mikael. Gradient Correlation Functions in Digital Image Correlation. *Applied Sciences* [online]. 2019, vol. 9, no. 10, p. 2127 [visited on 2023-12-29]. ISSN 2076-3417. Available from DOI: 10.3390/app9102127.

[69] FOUQUE, Raphaël; BOUCLIER, Robin; PASSIEUX, Jean-Charles; PÉRIÉ, Jean-Noël. Fractal Pattern for Multiscale Digital Image Correlation. *Experimental Mechanics* [online]. 2021, vol. 61, no. 3, pp. 483–497 [visited on 2023-12-29]. ISSN 0014-4851, ISSN 1741-2765. Available from DOI: 10.1007/s11340-020-00649-7.

[70] STOILOV, G.; KAVARDZHIKOV, V.; PASHKOULEVA, D. A Comparative Study of Random Patterns for Digital Image Correlation. *Journal of Theoretical and Applied Mechanics* [online]. 2012, vol. 42, no. 2, pp. 55–66 [visited on 2023-12-29]. ISSN 0861-6663. Available from DOI: 10.2478/v10254-012-0008-x.

[71] SAFAVIZADEH, S. A.; WARGO, A.; KIM, Y. Richard. Utilizing Digital Image Correlation (DIC) in Asphalt Pavement Testing. *Journal of Testing and Evaluation* [online]. 2018, vol. 46, no. 3, p. 20160262 [visited on 2023-12-29]. ISSN 00903973. Available from DOI: 10.1520/JTE20160262.

[72] ZHAO, Jianlong; SANG, Yong; DUAN, Fuhai. The State of the Art of Two-dimensional Digital Image Correlation Computational Method. *Engineering Reports* [online]. 2019, vol. 1, no. 2, e12038 [visited on 2023-12-29]. ISSN 2577-8196, ISSN 2577-8196. Available from DOI: 10.1002/eng2.12038.

[73]   PAN, Bing; XIE, Huimin; WANG, Zhaoyang. Equivalence of Digital Image Correlation Criteria for Pattern Matching. *Applied Optics* [online]. 2010, vol. 49, no. 28, p. 5501 [visited on 2024-01-08]. ISSN 0003-6935, ISSN 1539-4522. Available from DOI: `10.1364/AO.49.005501`.

[74]   GRUEN, Armin W.; BALTSAVIAS, Emmanuel P. Adaptive Least Squares Correlation With Geometrical Constraints. In: FAUGERAS, Olivier D.; KELLEY, Robert B. (eds.) [online]. Cannes, France, 1986, p. 72 [visited on 2024-01-08]. Available from DOI: `10.1117/12.952246`.

[75]   ALTUNBASAK, Y.; MERSEREAU, R.M.; PATTI, A.J. A Fast Parametric Motion Estimation Algorithm with Illumination and Lens Distortion Correction. *IEEE Transactions on Image Processing* [online]. 2003, vol. 12, no. 4, pp. 395–408 [visited on 2024-01-08]. ISSN 1057-7149. Available from DOI: `10.1109/TIP.2003.809012`.

[76]   PAN, Bing; ASUNDI, Anand; XIE, Huimin; GAO, Jianxin. Digital Image Correlation Using Iterative Least Squares and Pointwise Least Squares for Displacement Field and Strain Field Measurements. *Optics and Lasers in Engineering* [online]. 2009, vol. 47, no. 7-8, pp. 865–874 [visited on 2024-01-08]. ISSN 01438166. Available from DOI: `10.1016/j.optlaseng.2008.10.014`.

[77]   PAN, B; WANG, Z; XIE, H. Generalized Spatial-Gradient-Based Digital Image Correlation for Displacement and Shape Measurement with Subpixel Accuracy. *The Journal of Strain Analysis for Engineering Design* [online]. 2009, vol. 44, no. 8, pp. 659–669 [visited on 2024-01-08]. ISSN 0309-3247, ISSN 2041-3130. Available from DOI: `10.1243/03093247JSA546`.

[78]   BLABER, Justin. *Ncorr - Open Source 2D Digital Image Correlation MATLAB Software* [online]. [visited on 2023-12-28]. Available from: `https://www.ncorr.com/index.php`.

[79]   BLABER, Justin. *DIC Algorithms* [online]. [visited on 2023-12-28]. Available from: `https://www.ncorr.com/index.php/dic-algorithms`.

[80]   *What Is Python? Executive Summary* [online]. Python.org. [visited on 2023-12-30]. Available from: `https://www.python.org/doc/essays/blurb/`.

[81]   *About* [online]. OpenCV. [visited on 2023-12-30]. Available from: `https://opencv.org/about/`.

[82]   *What Is NumPy?* [online]. NumPy. [visited on 2023-12-30]. Available from: `https://numpy.org/doc/stable/user/whatisnumpy.html`.

[83]   GEUZAINE, Christophe; REMACLE, Jean-François. *Gmsh: A Three-Dimensional Finite Element Mesh Generator with Built-in Pre- and Post-Processing Facilities* [online]. Gmsh. [visited on 2023-12-30]. Available from: `https://gmsh.info/`.

[84]   TIWARI, Sumit. An Introduction to QR Code Technology. In: *2016 International Conference on Information Technology (ICIT)* [online]. Bhubaneswar, India: IEEE, 2016, pp. 39–44 [visited on 2023-12-30]. ISBN 978-1-5090-3584-7. Available from DOI: `10.1109/ICIT.2016.021`.

[85] ANSARI, Aslam. Quick Response Code and Its Use in Libraries: A Recent Trend. In: 2014, pp. 225–236. ISBN 978-93-84144-08-1.

[86] WASSER, Leah A. *Hierarchical Data Formats - What Is HDF5? | NSF NEON | Open Data to Understand Our Ecosystems* [online]. The National Ecological Observatory Network, 2020-10-07. [visited on 2023-12-30]. Available from: https://www.neonscience.org/resources/learning-hub/tutorials/about-hdf5.

[87] VAITHIYANATHAN, Dhandapani; MANIGANDAN, Muniraj. Real-Time-Based Object Recognition Using SIFT Algorithm. In: *2023 Second International Conference on Electrical, Electronics, Information and Communication Technologies (ICEEICT)* [online]. Trichirappalli, India: IEEE, 2023, pp. 1–5 [visited on 2024-01-07]. ISBN 9798350397635. Available from DOI: 10.1109/ICEEICT56924.2023.10157675.

[88] LINDEBERG, Tony. Scale Invariant Feature Transform. *Scholarpedia* [online]. 2012, vol. 7, no. 5, p. 10491 [visited on 2024-01-07]. ISSN 1941-6016. Available from DOI: 10.4249/scholarpedia.10491.

[89] *OpenCV: Introduction to SIFT (Scale-Invariant Feature Transform)* [online]. [visited on 2024-01-07]. Available from: https://docs.opencv.org/4.x/da/df5/tutorial_py_sift_intro.html.

[90] TYAGI, Deepanshu. *Introduction to SIFT(Scale Invariant Feature Transform)* [online]. Medium, 2020-04-07. [visited on 2024-01-07]. Available from: https://medium.com/@deepanshut041/introduction-to-sift-scale-invariant-feature-transform-65d7f3a72d40.

[91] *Camera Calibration and 3D Reconstruction* [online]. [visited on 2024-01-07]. Available from: https://docs.opencv.org/3.4/d9/d0c/group__calib3d.html#ga4abc2ece9fab9398f2e560d53c

[92] MALLICK, Satya. *Geometry of Image Formation | LearnOpenCV #* [online]. 2020-02-20. [visited on 2024-01-07]. Available from: https://learnopencv.com/geometry-of-image-formation/.

[93] *TAS501N Micro S Type Load Cell* [online]. HTC. [visited on 2023-12-27]. Available from: http://www.htc-sensor.com/products/196.html.

[94] *MTS* [online]. MTS. [visited on 2023-12-27]. Available from: https://www.mts.com/en/products/materials/static-materials-test-systems/www.mts.com.

[95] *OLS5100 | Olympus IMS* [online]. LEXT™ OLS5100 3D Laser Scanning Microscope. [visited on 2023-12-28]. Available from: https://www.olympus-ims.com/en/microscopes/laser-confocal/ols5100/.

[96] EUROPE, Canon. *Specifications & Features - Canon EOS 6D Mark II* [online]. Canon Europe. [visited on 2023-12-02]. Available from: https://www.canon-europe.com/cameras/eos-6d-mark-ii/specifications/.

[97]   *Arducam High Quality Complete USB Camera Bundle, 12MP 1/2.3 Inch IMX477 Camera Module with 6mm CS-Mount Lens, Metal Enclosure, Tripod and USB Cable* [online]. Arducam. [visited on 2023-12-27]. Available from: https://www.arducam.com/product/arducam-high-quality-complete-usb-camera-bundle-12mp-1-2-3-inch-imx477-camera-module-with-6mm-cs-mount-lens-metal-enclosure-tripod-and-usb-cable-b0280/.

[98]   *Image Sensor for Consumer Cameras | Products & Solutions* [online]. Sony Semiconductor Solutions Group. [visited on 2023-12-27]. Available from: https://www.sony-semicon.com/en/products/is/camera/index.html.

[99]   *Arducam 2.8-12mm Varifocal C-Mount Lens for Raspberry Pi HQ Camera, with C-CS Adapter* [online]. Arducam. [visited on 2023-12-27]. Available from: https://www.arducam.com/product/arducam-2-8-12mm-varifocal-c-mount-lens-for-raspberry-pi-hq-camera-with-c-cs-adapter/.

[100]   *Arducam CS-Mount Lens for Raspberry Pi HQ Camera, 16mm Focal Length with Manual Focus and Adjustable Aperture* [online]. Arducam. [visited on 2023-12-27]. Available from: https://www.arducam.com/product/arducam-cs-mount-lens-for-raspberry-pi-hq-camera-16mm-focal-length-with-manual-focus-and-adjustable-aperture/.

[101]   RABIE, Tamer. Lossless Quality Steganographic Color Image Compression. *International Journal of Advanced Computer Science and Applications* [online]. 2015, vol. 6, no. 4 [visited on 2023-12-17]. ISSN 21565570, ISSN 2158107X. Available from DOI: 10.14569/IJACSA.2015.060416.

[102]   NIKOUKHAH, Tina; COLOM, Miguel; MOREL, Jean-Michel; GROMPONE VON GIOI, Rafael. Local JPEG Grid Detector via Blocking Artifacts, a Forgery Detection Tool. *Image Processing On Line* [online]. 2020, vol. 10, pp. 24–42 [visited on 2023-12-17]. ISSN 2105-1232. Available from DOI: 10.5201/ipol.2020.283.

[103]   BARRETT, Richard T. *Fastener Design Manual* [online]. 1990. [visited on 2023-12-27]. Available from: https://ntrs.nasa.gov/citations/19900009424.

[104]   *ČSN EN ISO 21920-1 (014450): Geometrical Product Specifications (GPS) - Surface Texture: Profile - Part 1: Indication of Surface Texture*. 2023.

[105]   *ČSN EN ISO 21920-2 (014450): Geometrical Product Specifications (GPS) - Surface Texture: Profile - Part 2: Terms, Definitions and Surface Texture Parameters*. 2023.

[106]   *ČSN EN ISO 21920-3 (014450): Geometrical Product Specifications (GPS) - Surface Texture: Profile - Part 3: Specification Operators*. 2023.

[107]   FRIS, Daniel. Analysis of the Accuracy and the Surface Roughness of FDM/FFF Technology and Optimisation of Process Parameters. *Tehnicki vjesnik - Technical Gazette* [online]. 2020, vol. 27, no. 4 [visited on 2023-11-26]. ISSN 13303651, ISSN 18486339. Available from DOI: 10.17559/TV-20190320142210.

[108]   *ČSN EN ISO 527-1 (640604): Plastics - Determination of Tensile Properties - Part 1: General Principles*. 2020.

[109] *ČSN EN ISO 527-2 (640604): Plastics - Determination of Tensile Properties - Part 2: Test Conditions for Moulding and Extrusion Plastics.* 2012.

[110] *ČSN EN ISO 178 (640607): Plastics - Determination of Flexural Properties.* 2019.

[111] FARHADI MACHEKPOSHTI, D.; TOLOU, N.; HERDER, J. L. A Review on Compliant Joints and Rigid-Body Constant Velocity Universal Joints Toward the Design of Compliant Homokinetic Couplings. *Journal of Mechanical Design* [online]. 2015, vol. 137, no. 3, p. 032301 [visited on 2023-12-27]. ISSN 1050-0472, ISSN 1528-9001. Available from DOI: 10.1115/1.4029318.